THE IDENTIFICATION AND PROPERTIES OF LINKED AND KNOTTED

FLUX TUBES IN PARTICLE PHYSICS

By

Martha J. Holmes

Dissertation

Submitted to the Faculty of the

Graduate School of Vanderbilt University

in partial fulfillment of the requirements

for the degree of

DOCTOR OF PHILOSOPHY

in

Physics

May, 2009

Nashville, Tennessee

Approved:

Thomas W. Kephart

Senta V. Greene

Robert A. Knop

Robert J. Scherrer

Bruce Hughes

David J. Ernst

ACKNOWLEDGMENTS

TABLE OF CONTENTS

Page

Chapter

LIST OF FIGURES

CHAPTER I

INTRODUCTION

1.1   Motivation and Thesis Overview

Our current understanding of strong interactions of quarks and gluons is that they are described by the non-Abelian gauge field theory Quantum Chromodynamics (QCD) [1, 2, 3]. Even though QCD provides a theory of strong interactions, very little is known about the physical states of the theory [4]. Until we can both predict the properties of the physical states of the theory and confirm these predictions by experiment we can hardly claim to understand QCD.

To a large extent our knowledge of hadron physics is based on phenomenological models, in particular the quark model [5, 6]. Meson and baryon spectroscopy is described well as composite objects made of constituent valence quarks. Particles that can be described by valence quark configurations are referred to as "conventional." Most QCD-motivated models, however, predict other types of strongly interacting particles with explicit glue degrees of freedom. These are glueballs, which have no constituent quarks in them at all, and hybrids, which have both constituent quarks and excited gluon degrees of freedom.

At present, the observed meson states exceed the number of states which can be accommodated by the quark model. Models predict that the lowest mass glueball states carry the same quantum numbers as scalar mesons. Controversy surrounds

the classification of these extraneous states as well as the expected experimental signatures of glueballs. My thesis focuses on modeling glueballs as tightly knotted or linked tubes of color flux. The model predicts a spectrum of glueball states based on the known spectrum of knots and links.

Chapter I provides an introduction to the theoretical foundations of QCD, the Standard Model and glueballs. Chapter II introduces the model of glueballs as tightly knotted or linked flux tubes and summarizes the most recent calculations and plots associated with the model. The model presented in chapter II includes both ground states and excited states, however for the purpose of calculating rotational energies it assumes the tightly knotted or linked flux tubes are spherical rigid rotors to lowest order. In order to more accurately determine the rotational energies, Chapter III presents the exact calculation of the moment of inertia tensor for several geometries. Chapter IV uses the bag model to estimate the radius of a knotted or linked flux tube, discusses spherical, symmetric and asymmetric rigid rotors and explores the relationship between the classification of a rigid rotor and its rotational energy. Using the results of calculations in Chapters III and IV, Chapter V calculates the rotational energy of the knots and links used in the model. In conclusion, Chapter VI summarizes the results found and mentions possible future directions for the model.

1.2 The Standard Model

1.2.1 Interactions

There are four fundamental interactions known in nature: strong, electromagnetic, weak, and gravitational [9].

The classical theory of gravity is Newton's law of universal gravitation. Its relativistic generalization is Einstein's general theory of relativity. A successful quantum theory of gravity has yet to emerge.

The physical theory describing electromagnetic interactions is called electrodynamics. Maxwell formulated the classical theory of electrodynamics more than a hundred years ago, and his theory is consistent with relativity. The quantum theory of electrodynamics, or QED, emerged in the 1940s from work by Tomonaga, Feynman, Schwinger and many others.

The theory of the weak interaction was given a relativistic quantum formulation from the very beginning. The weak interaction is responsible for nuclear beta decay, charged pion decay, muon decay, and the decay of many of the strange particles. The first theory of the weak interaction was presented by Fermi in 1933; it was refined by Lee and Yang, Feynman and Gell-Mann, and many others in the 1950s, and put into its current form by Glashow, Weinberg, and Salam in the sixties. The theory of electroweak interactions is referred to as Glashow-Weinberg-Salam (GWS) theory; the GWS model actually treats weak and electromagnetic interactions as different manifestations of a single electroweak force, therefore reducing the four forces to three.

The idea of the strong interaction began with Yukawa in 1935. Elements of the theory of the strong interaction developed during the 1960s and 1970s. In 1973, Fritzsch, Gell-Mann, and Leutwyler published a paper [1] that is frequently referred to as the foundation for the relativistic quantized theory of strong interaction, known as Quantum Chromodynamics (QCD).

In the quantum field theory description, each of these interactions is the result of the exchange of a particle. The particles exchanges are called mediators and are all bosons, which are particles with integer spin. The gravitational mediator is the graviton; electromagnetic interactions are mediated by the photon, strong interactions by the gluon, and weak interactions by the intermediate vector bosons, $W^{\pm}$ and Z.

In the late 1970s, the Standard Model emerged as a theory that describes all of the known elementary particle interactions except gravity. The Standard Model is a collection of related theories combining the GWS theory of weak processes and QCD. Since 1978, it has satisfied the hypotheses of every experimental test[1].

1.2.2 Quarks and Leptons

Leptons and quarks are the basic building blocks of matter [7]. These particles carry spin $\frac{1}{2}$, in units of $\hbar$, so they are fermions. They are structureless at the smallest distances currently probed by the highest-energy accelerators. Particles interact as a result of the exchange of bosons.

Leptons are particles which if electrically charged, interact electromagnetically

---

[1]The Standard Model satisfies all experimental hypotheses when the model was extended to include right handed neutrinos

and weakly, and, if neutral, only weakly[2] [8]. By contrast, quarks are 'strongly interacting analogues' of leptons, since they interact via strong, electromagnetic and weak interactions. This is the basis for distinguishing between these two types of fundamental matter, a distinction which will presumably disappear if it eventually proves possible to unify all three types of forces.

Table 1.2.1 below lists charged and neutral leptons. All leptons and quarks have their own antiparticles[3]. There are six leptons, classified according to their charge (Q), electron number (L_e), muon number (L_μ), and tau number (L_τ). They fall naturally into three families, or generations: Similarly, there are six types of quarks,

Table 1.2.1: Lepton Classification

Generation	Lepton	Q	L_e	L_μ	L_τ
1st	e	-1	1	0	0
1st	ν_e	0	1	0	0
2nd	μ	-1	0	1	0
2nd	ν_μ	0	0	1	0
3rd	τ	-1	0	0	1
3rd	ν_τ	0	0	0	1

which are classified by electric charge and flavor: strange (S), charm (C), bottom (B), and top (T). Additionally quarks carry a new type of charge, called color. There are 3 defined colors: red, blue, and green. Antiquarks have the complementary colors anti-red, anti-blue and anti-green. With color, there are a total of 36 quarks and antiquarks. The quarks also fall into three generations, as shown in Table 1.2.2.

---

[2]There are a couple of exceptions to this general statement.
[3]If we include ν_R

Table 1.2.2: Quark Classification

Generation	Quark	Q	I_3	S	C	B	T
1st	d	$-1/3$	$-1/2$	0	0	0	0
1st	u	$2/3$	$1/2$	0	0	0	0
2nd	s	$-1/3$	0	-1	0	0	0
2nd	c	$2/3$	0	0	1	0	0
3rd	b	$-1/3$	0	0	0	-1	0
3rd	t	$2/3$	0	0	0	0	1

1.3   Theory

1.3.1   Fields

The passage from a classical field theory to the corresponding quantum field theory does not involve modification of the Langrangian or the field equations, but rather a reinterpretation of the field variables; the fields are "quantized," and particles emerge as quanta of the associated fields. Leptons and quarks are quanta of fermionic Dirac fields; the photon is the quantum of the electrodynamic field, A^μ; the $W^\pm$ and Z are quanta of the appropriate weak gauge fields; gluons are quanta of the eight QCD gauge fields.

Each Lagrangian determines a particular set of Feynman rules. The Feynman rules, along with Feynman diagrams, represent the possible interactions. The Langrangian consists of two kinds of terms: the free Langrangian for each participating field, plus various interaction terms ($\mathcal{L}_{int}$). The former determines the propagator; the latter-obtained by invoking local gauge invariance-determine the vertex factors.

1.3.2   Gauge Theories

In the Standard Model, the theory of the electroweak and color interaction is a gauge theory. Gauge theories are based on the application of the basic idea that the form of a physical theory should not depend on how the coordinate frame is chosen from point to point in space-time [10]. This is called the principle of local gauge invariance. The form of physical laws should remain unchanged regardless of how the local choice of axes is made.

The simplest application of local gauge invariance within the Standard Model is to electromagnetism. All quantum theories in the Standard Model involve the description of particles in terms of wavefunctions and involve internal spaces. In electromagnetism, the internal space is one-dimensional. In quantum mechanics, the absolute phase of the wavefunction of an electron, ψ, has no significance. When ψ is changed to $\psi \exp(i\alpha e)$, where e is its charge and α is an overall constant no observable consequences occur. The probability that the electron is in a volume dV is unaltered and so is the expectation value of the momentum operator. Therefore, both the position and the motion of the electron are unaffected. This phase change is called a global gauge transformation because it changes the phase in the same way at all points in space-time. When we apply local gauge invariance, the phase change α varies with position and time yielding the following wavefunction:

$$\psi \rightarrow \psi \exp[i\alpha(x,t)e] \tag{1.3.1}$$

Here $\alpha(x,t)e$ represents a rotation in a one-dimensional complex space. It is important to note that the "rotation" corresponding to the $U(1)$ symmetry is not in the

four-dimensional space-time in which the electrons and photons move and live. The rotations of the $U(1)$ group are an internal rotation in an abstract space associated with the field. This internal space, or 'charge' space, is not related to space-time; it is an abstract mathematical space where internal symmetries live. Local gauge invariance applied to this charge space would require that the laws of physics do not depend on the local choice of α. Unlike a global gauge transformation, a local gauge transformation changes the derivatives of the fields.

The symmetry group of QED is the rotational group $U(1)$; 'U' specifies a unitary transformation in which the amplitude of ψ is not affected and '1' refers to the dimensionality of the complex space. The family of phase transformations $U(\alpha) = \exp(i\alpha e)$ forms a unitary Abelian group known as the $U(1)$ group. Abelian just records the property that the group multiplication is commutative:

$$U(\alpha_1)U(\alpha_2) = U(\alpha_2)U(\alpha_1) \tag{1.3.2}$$

If all the group elements commute, as shown above, the group is called Abelian. If the group elements do not commute, the group is called non-Abelian:

$$U(\alpha_1)U(\alpha_2) \neq U(\alpha_2)U(\alpha_1) \tag{1.3.3}$$

Forcing the $U(1)$ symmetry to become a local symmetry, and applying the gauge principle, means that the "angle" of rotation appears in the transformation properties of the single gauge field of QED, the photon.

The difference between global and local gauge transformations occurs when we calculate the derivatives of the fields. Instead of a simple phase factor, we pick up an

extra term. However, if we replace every partial derivative by the covariant derivative, the extra term will cancel out. The covariant derivative has the form:

$$D_\mu \equiv \partial_\mu - ieA_\mu \,. \tag{1.3.4}$$

The only way that symmetry may be preserved under local changes in the phase of an electron field is if a new field, A_μ, is introduced. Changes in this new field absorb those contributions arising from the local phase change of the electron field that would otherwise destroy the symmetry properties. This new field must be coupled to the electron field and the strength of this coupling is expressed in the Lagrangian by a coupling constant. This field is called a gauge field and it is actually the photon, which is a "gauge boson," an interaction-transmitting particle having integer spin which emerges in $U(1)$ gauge theory as the preserver of local gauge symmetry.

In order to enforce local phase symmetry and local charge conservation, a theory of free electrons/positrons must introduce photons and an interaction with those photons. The requirement of local gauge invariance generates the electromagnetic field. The substitution of D_μ for ∂_μ is a mechanism for converting a globally invariant Lagrangian into a locally invariant one. The idea that the interactions of the theory are determined by forcing it to respect local phase symmetry, or gauge symmetry, is termed the gauge principle.

The link between symmetry and interactions is very powerful. Quantum field theory gives the basic structure, but does not specify the phase of the quantum field. An interaction automatically appears if the phase is allowed to assume different values at different points of space/time as well as the imposed condition that the Lagrangian

has a symmetry with respect to the phase change. Start with a quantum field theory having no interactions, add symmetry via the phase, enforce the gauge principle, and the result is a gauge theory with interactions. The interaction is mediated by a gauge field that emerges to fulfill this role.

The successful application of local gauge invariance to electromagnetism suggests applying it elsewhere to explain other forces. In 1954 Yang and Mills applied the same strategy to the group $SU(2)$. What would we expect in the general case when the gauge principle is applied to an $SU(n)$ internal space? There would be $(n^2 - 1)$ gauge fields. Leptons and quarks would be expected to appear in multiplets with n members. In order to recognize $SU(n)$ symmetries in nature we can examine whether the quarks and leptons are arranged in multiplets.

Both quarks and leptons feel the weak force and appear in doublets and singlets so that $SU(2)$ is presumably the symmetry underlying the weak force. The symmetry group for color proposed by Greenberg was $SU(3)$. Since quarks, which possess color, feel the strong force while leptons do not suggests that the $SU(3)$ of color is the symmetry underlying the strong force[4].

The quark wavefunction appears as:

$$\psi \exp[i\epsilon_\alpha(x,t)\lambda_\alpha] \tag{1.3.5}$$

where ϵ_α is a rotation angle in color space and λ_α are the Gell-Mann matrices. These matrices are the generators of rotation for the $SU(3)$ symmetry. The $SU(3)$ group is non-Abelian because not all of the generators λ_α commute with each other. According

---

[4]Leptons are in $SU_c(3)$ singlets

to the gauge principle the values of ϵ_α can be chosen arbitrarily at each point in space-time without affecting the physics. The appropriate covariant derivative for quantum chromodynamics is:

$$D_\mu \equiv \partial_\mu - igA_\mu^\alpha \lambda_\alpha \qquad (1.3.6)$$

where g is the coupling constant. Physically, A_μ^α, are the gluon fields that mediate the strong interactions.

1.3.3   Quantum Chromodynamics

Quarks carry an extra charge, color, and interact via the exchange of gluons. Color is triple valued; all objects directly observable in experiments are color-neutral. As a result, quarks and gluons appear to be confined within colorless baryons and mesons; this is known as confinement. Gluons carry one color and one anticolor in a color octet configuration; the completely symmetric configuration $1/\sqrt{3}(r\bar{r} + b\bar{b} + g\bar{g})$ is a color singlet and excluded, hence there exist 8 gluons. The 8 gluon states which make up a 'color octet' are given by: $|1> = \frac{(r\bar{b}+b\bar{r})}{2}$, $|2> = -i\frac{(r\bar{b}-b\bar{r})}{2}$, $|3> = \frac{(r\bar{r}-b\bar{b})}{2}$, $|4> = \frac{(r\bar{g}+g\bar{r})}{2}$, $|6> = \frac{(b\bar{g}+g\bar{b})}{2}$, $|7> = -i\frac{(b\bar{g}-g\bar{b})}{2}$, and $|8> = \frac{(r\bar{r}+b\bar{b}-2g\bar{g})}{6}$.

Gluons are massless particles like photons that carry the same quantum numbers as photons, $J^{PC} = 1^{--}$. Photons don't carry electric charge, however gluons carry color charge. As a result gluon-gluon interactions are possible as well with three- and four-point vertices, as shown in Figure 1. A theory of strong interactions based on the exchange of colored gluons between colored quarks can be constructed in a fashion similar to QED. The resulting theory, QCD, can be shown to be renormalizable. Like
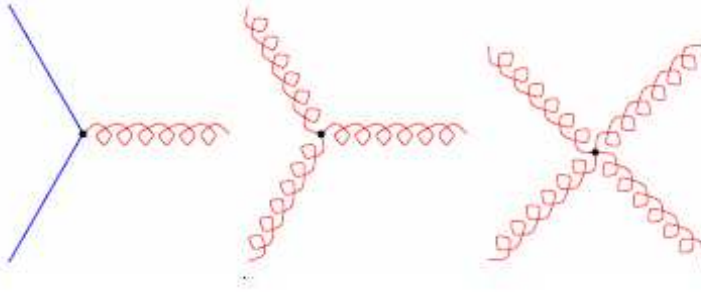
Figure 1: Quark-gluon and gluon-gluon interactions

in QED, some expressions give infinite contributions, but the renormalizable scheme allows one to control all divergences. QCD is described by the Lagrangian [4]:

$$\mathcal{L}_{QCD} = \bar{q}_i \left(iD_\mu \gamma^\mu - m\delta_{ij} \right) q_j - \frac{1}{4} F_{\mu\nu}^a F^{a\,\mu\nu} \,, \tag{1.3.7}$$

where

$$F_a^{\mu\nu} = \partial^\mu A_a^\nu - \partial^\nu A_a^\mu - g f_{abc} A_b^\mu A_c^\nu \,. \tag{1.3.8}$$

A_a^μ are the gluon fields with $a = 1, ..., 8$, q_i are the quark fields with indices $i = 1, 2, 3$, g is the bare coupling and m is the quark mass. The non-Abelian group structure of $SU(3)$ leads to nonlinear terms in the field strength $F_a^{\mu\nu}$, which gives rise to trilinear and quadratic vertices in the theory. This non-linearity makes the theory difficult to solve, and leads to the confinement of color. A consequence of this behavior appears to be the existence of new hadrons, particles that interact strongly, with gluonic degrees of freedom known as glueballs and hybrids. The energy region most relevant to our daily lives is where the QCD coupling constant is really strong. In this area protons and neutrons and their excitations exist. Neither perturbative QCD nor chiral

12

perturbation theory are able to describe interactions in this region. For momentum scales given by typical hadron masses, around 1 GeV, not only α_s changes but also relevant degrees of freedom change from current quarks to constituent quarks.

The masses of quarks are difficult to determine. No free separated quark has even been observed. Since quarks are never free, quark masses are only revealed through their effect on some interaction [13]. Quark masses are not unique, but depend on how they are defined. One way to estimate quark masses is to use a simple quark model of hadrons that reproduces the pattern of hadron masses. As each quark lives inside a hadron filled with interacting quarks and gluons, they behave as though they have an effective mass that isn't necessarily their "true" mass. This effective mass is called the constituent mass. Roughly, the constituent masses of the u and d quarks are about a third the mass of the proton (~ 938 MeV), so they come out to around 300 MeV each. In theory, the quark masses enter into calculations as parameters which can then be determined by comparison of the computational results with the data [7]. In this case, we solve the equations of strong interactions and the resulting quark masses are called current quark masses. The mean mass values are presented in Table 1.3.1 [12]. Complications arise in the theory of strong interactions. The

Table 1.3.1: Constituent and current quark masses

LIGHT QUARKS					HEAVY QUARKS			
	d	u	s		c	b	t	
current mass	~ 6	~ 3	~ 115	MeV	~ 1.3	~ 4.2	~ 174	GeV
constituent mass	~ 330	~ 330	~ 510	MeV	~ 1.5	~ 5.0	~ 174	GeV

13

coupling constant, α_s, increases dramatically with decreasing momentum transfer, Q^2, and consequently QCD predictions in the low-energy regime are difficult. At high momentum transfer, α_s is small and QCD can be successfully approached using perturbation theory. At low energies, there is progress in numerically calculating QCD quantities on a discrete space-time lattice.

For lower energies confinement becomes the most important aspect of strong interactions. This is the realm of non-perturbative QCD or of *strong* QCD. At very small energies, in the chiral limit, observables can be expanded in powers of masses and momenta and chiral perturbation theory leads to reliable predictions. At very large energies QCD can be treated perturbatively. The strong interaction constant α_s decreases and particles behave asymptotically as if they were free. In an extremely hot and dense environment we expect quarks to become free; a phase transition to the quark-gluon plasma is expected and may have been observed.

In short, experimentally it has been shown that the coupling constant in QCD depends on energy. However, experiments have shown that for *both* QED and QCD the strength of the interaction depends on energy [14]. Though both theories share a similar mechanism for this energy-dependence, the two respond in opposite ways to changes in energy. In QED, screening provides a simple physical picture of how the coupling *increases* as the test particle is probed more closely. In contrast, for QCD the coupling *decreases*. This is explained in terms of an anti-screening effect. The virtual particle pairs surrounding a bare color charge actually make the color charge on a quark appear stronger than it is, and when a probe quark penetrates through the

layers of anti-screening, the core is revealed to be weaker, not stronger. An electron induces a cloud of positive charge around itself, thereby diluting its negative charge. By contrast, a quark appears to induce around it a color charge of the same type. The root of the difference lies in the fact that the gluons themselves carry color. As a result, the gluons that appear in the cloud of virtual particles around a bare quark contribute directly, whereas the photons in the QED case do not.

The expression for the strong coupling parameter, α_s, is one of the key results of QCD. Much information can be gained by examining the following expression:

$$\alpha_s(Q^2) = \frac{12\pi}{(33 - 2n_f)\ln(Q^2/\Lambda^2)} \tag{1.3.9}$$

The formula for the strong coupling constant is quite similar to that for QED. One difference is an additional term in the factor in the denominator, $33 - 2n_f$, where n_f is the number of flavors. The 33 comes from the gluons, and the fact that the color group is $SU(3)$: a different symmetry group would give a different number. The $2n_f$ comes from the quarks, and reflects the number of different virtual quark-antiquark pair possibilities into which gluons may transform during the course of an interaction. If this factor is negative, then, as in QED, the effective coupling *increases* at small distances; if it is positive, the coupling *decreases* [9]. The number of flavors is related to the strength of the strong force. In the Standard Model there are 6 flavors, so that $33 - 2n_f$ comes out positive and as a result the QCD coupling decreases at small distances. Qualitatively, this is the origin of asymptotic freedom. In QCD, there is no way to measure the strength of the color charge on an isolated quark. As a result, it is difficult to determine the full spectrum for the strong coupling constant. All we can

do is measure α_s at some reasonable energy to fix the overall scale, just as knowing the charge of an electron fixes the sliding scale of the electromagnetic coupling in QED.

As a result, it is more convenient to relate the strong coupling and energy in terms of some parameter, whose value is known just as soon as experimenters have made a measurement of α_s. This parameter, or equivalently the α_s measured at some specific energy, is the single fundamental constant in the theory. It must be determined by experiment, whereas most other constants are derived from theory. This new parameter is called Λ, and it has dimensions of mass. It is referred to as the "Λ_{QCD}," or "QCD scale parameter." Determining a definite value for Λ has proved difficult. The accepted value of Λ is about 200 MeV.

The QCD Lagrangian knows nothing about the Λ parameter or an intrinsic mass or length scale. The theory of QCD is scale invariant, it doesn't distinguish between the sizes of particles. However, this changes when the Lagrangian is quantized and renormalized. Renormalization introduces a length scale - a momentum cutoff or a renormalization scale. The fact that the physical content of the theory is invariant with respect to this scale factor yields the *change* of the strong coupling with energy. But to get an actual value for the strong coupling means including the renormalization scale in the guise of the Λ parameter. The quantum theory of QCD therefore acquires a scale-dependence in the form of the Λ parameter: the scale invariance of the Lagrangian is sacrificed in the transition to a full quantum theory. The value of 200 MeV for Λ corresponds to a distance scale of around one fermi, a little smaller

16

than the wavelength associated with a pion and roughly the size of a proton.

If the energy scale gets close to the value of Λ, then the strong coupling parameter is large, and perturbation theory no longer holds. In other words, Λ dictates where the usefulness of perturbation theory ends. These energy divisions are represented in Figure 2. At low energies, below 1 GeV, one approach that has proved useful is lattice
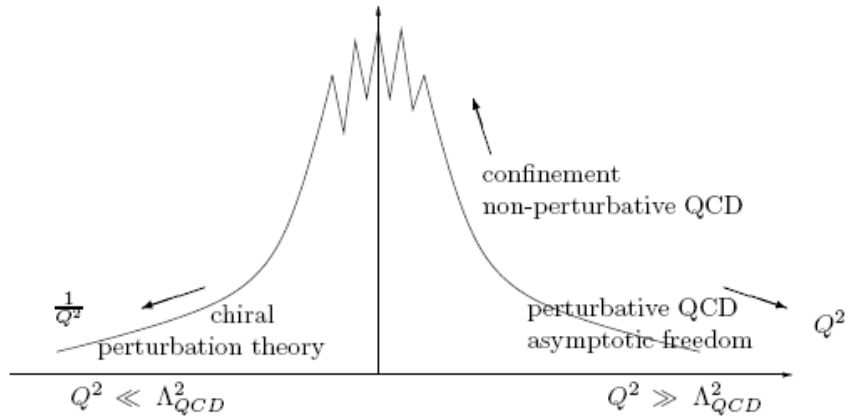
Figure 2: QCD regions in terms of momentum transfer, Q^2, and Λ^2_{QCD}

QCD. Lattice QCD has approached the non-perturbative region of QCD using computers to solve the equations of QCD. Within non-perturbative QCD lies confinement, the antithesis of high-energy's asymptotic freedom. When a quark and antiquark try to separate, it becomes energetically favorable to create a quark-antiquark pair from the vacuum. One way to visualize this scenario is to imagine the quark and antiquark are connected by a gluon string. The quark and antiquark rotate about each other, held a fixed distance apart by the string, their centrifugal motion keeping the string

rigid. Confinement implies that the force between a quark and an antiquark remains constant as they are pulled apart, so as the string is stretched it does not weaken. Instead, the energy added to the system by pulling the quark and antiquark apart is converted into more string, and the string becomes longer. The string does not grow
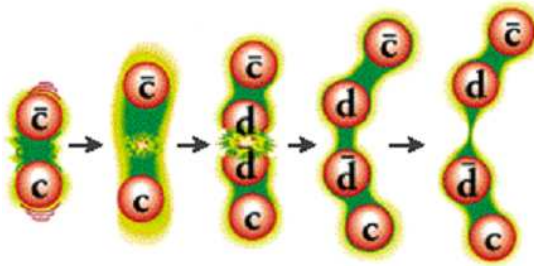
Figure 3: The mechanism of quark confinement. As the quark and antiquark separate, eventually it becomes energetically favorable to create a quark-antiquark pair from the vacuum.

indefinitely; there is a point at which it is energetically favorable to break. The gluon string breaks, and an antiquark and quark emerge. There are now two mesons, each connected by string. Figure 3 illustrates this concept.

This "string" contains lines of color force. How do gluons fit into this picture? The quark and antiquark behave as though they are relatively free when they are close together. As more energy is put into separating the quark-antiquark pair, the energy goes into creating more and more quark/antiquark pairs and gluons from the vacuum. As the gluons grow in number they cause an attractive force between the gluons mediating the quark-antiquark attraction, in effect pulling the gluon color

force lines together. This is a direct consequence of the fact that gluons themselves have color, and interact with each other. As the quark and antiquark are pulled apart, more gluons are created therefore causing the lines of color linking the pair to come together. The interaction strength grows, and is directed along a tube of force, yielding the "string" connecting the quark and antiquark. The channeling of color force into a tube yields a force that is roughly constant with increasing separation, and is ultimately responsible for the pair's confinement. The squared coupling constant α_s becomes very large for large distances, which leads to quark confinement. This feature of QCD implies that neither single quarks nor gluons can be observed as free particles. It is the large-distance behavior that is probed at low energies and it cannot be described by a single coupling constant but is effectively depicted by meson exchanges and their couplings to baryons.

1.4 Mesons

Mesons were first introduced by Yukawa [15] with pions acting as the exchange bosons responsible for the strong interactions between nucleons [4]. The introduction of high-energy accelerators led to a whole zoo of mesons and baryons, creating great confusion. Eventually, when the various mesons and baryons were arranged into multiplets based on their quantum numbers, patterns started to emerge. It was recognized that hadrons of a given J^{PC} arranged themselves into representations of the group $SU(3)$, although none of the observed states seemed to correspond to the fundamental triplet representation. Zweig and Gell-Mann postulated that the mesons

and baryons were actually composite objects, with mesons made of a quark-antiquark pair and baryons made of three quarks.

1.4.1   Quantum Numbers

The quark model is a classification scheme for hadrons in terms of their valence quarks, the quarks and antiquarks which give rise to the quantum numbers of the hadrons [16]. There are two sets of quantum numbers used to identify hadrons. The first set, J^{PC} where J is the total angular momentum, P, the intrinsic parity, and C the charge conjugation parity. The remainder are flavor quantum numbers such as the isospin, I. When three flavors of quarks are taken into account, the quark model is also known as the eightfold way, in reference to the meson octet.

Quarks have spin $S = 1/2$ and baryon number $B = 1/3$, antiquarks $S = 1/2$ and $B = -1/3$. A quarks and an antiquark can form bound states with $B = 0$ and spin $S = 1$ or $S = 0$. A conventional meson is defined as a $q\bar{q}$ system and has the following properties [7].

The parity of a meson due to the orbital angular momentum between quark and antiquark is given by $P = (-1)^L$. Quarks also have intrinsic parity which we define to be $P = 1$; antiquarks have opposite parity $P = -1$. The total parity of a $q\bar{q}$ meson is hence given by

$$P = (-1)^{L+1} \tag{1.4.1}$$

Parity is conserved in strong interactions.

Neutral mesons with no strangeness are eigenstates of the charge conjugation

operator, sometimes called C-parity,

$$C = (-1)^{L+S} \qquad (1.4.2)$$

where only neutral mesons are eigenstates of C.

Soon after the discovery of the neutron, Heisenberg observed that the mass of the proton and the neutron were amazingly close. Heisenberg proposed that they be regarded as two "states" of a *single* particle, the nucleon. This idea led to the introduction of isospin, I. The nucleon carries isospin $I = 1/2$, and the third component has eigenvalues $+1/2$ (the proton) and $-1/2$ (the neutron) [2]. The proton and neutron are said to form an isospin doublet. The three pions have isospin $I = 1$, they form an isospin triplet.

$$|I = 1, I_3 = 1\rangle = -|u\bar{d}\rangle = -|\pi^+\rangle \qquad (1.4.3)$$

$$|I = 1, I_3 = 0\rangle = \frac{1}{\sqrt{2}}(|u\bar{u}\rangle - |d\bar{d}\rangle) = |\pi^0\rangle \qquad (1.4.4)$$

$$|I = 1, I_3 = -1\rangle = -|d\bar{u}\rangle = |\pi^-\rangle \qquad (1.4.5)$$

isospin is conserved in strong interactions. The C-parity only has a defined eigenvalue for particles which are their own antiparticles. The action of C-parity on other states leads to their antiparticles.

$$C|\pi^0\rangle = +|\pi^0\rangle \,;\; C|\pi^+\rangle = |\pi^-\rangle \,;\; C|\pi^-\rangle = |\pi^+\rangle \qquad (1.4.6)$$

C-parity is conserved in strong interactions.

C-parity becomes more useful when it is used in G-parity; G-parity is C-parity followed by a rotation in isospin space by 180° degrees about the y-axis. The rotation

by 180° about the y-axis in isospin space will carry I_3 into $-I_3$, converting, for instance a π^+ into a π^-. The rotation is given by

$$e^{i\pi I_y} \tag{1.4.7}$$

We can now define the G-parity as follows:

$$G = C \cdot e^{i\pi I_y} \tag{1.4.8}$$

G-parity is defined and has the same value for all members of a multiplet; it is essentially the generalization of C-parity to multiplets of particles. Since it depends on isospin, it is conserved in strong interaction. An example would be the following

$$G|\pi^{\pm,0}\rangle = \eta_G|\pi^{\pm,0}\rangle \tag{1.4.9}$$

where $\eta_G = \pm 1$ are the eigenvalues of G-parity.

1.4.2 Meson Nonets

Mesons are characterized by their quantum numbers J^{PC} and by their flavor content. These are measured quantities. In the light quark domain we have $SU(3)$ symmetry which leads to a nonet of states, we expect an octet and a singlet. If the flavor symmetry was exact, then all nine mesons would have the same mass. Table 1.3.1 shows that the light quarks are similar in mass. However, the s quark is heavier than the u and d quarks. Since the three quarks are similar in mass, but not equal is mass, the three pairs $u\bar{u}$, $d\bar{d}$ and $s\bar{s}$ can therefore form mesons which are approximate $SU(3)$ eigenstates meaning they are mesons composed of linear combinations of $u\bar{u}$,

$d\bar{d}$ and $s\bar{s}$ pairs.

Mesons carry both orbital angular momentum, L, and spin, S. Mesons with $J = 0$ and positive parity are called scalar particles. Mesons with $J = 0$ and negative parity are pseudoscalar particles. For example, a pseudoscalar particle is a particle with quantum numbers $J^{PC} = 0^{-+}$.

From the three quarks u, d, s and their antiquarks, nine $SU(3)$ eigenstates can be constructed. The nine states are orthogonal; one of them is the singlet, the η_1, which is invariant under rotations in $SU(3)$. Figure 4 shows the nonet representation of the pseudoscalar mesons. The eightfold way classification is the result of a pattern

with $\pi^0 = \frac{1}{\sqrt{2}}\left|u\bar{u} - d\bar{d}\right\rangle$, $\eta_8 = \frac{1}{\sqrt{6}}\left|u\bar{u} + d\bar{d} - 2s\bar{s}\right\rangle$, and $\eta_1 = \frac{1}{\sqrt{3}}\left|u\bar{u} + d\bar{d} + s\bar{s}\right\rangle$.
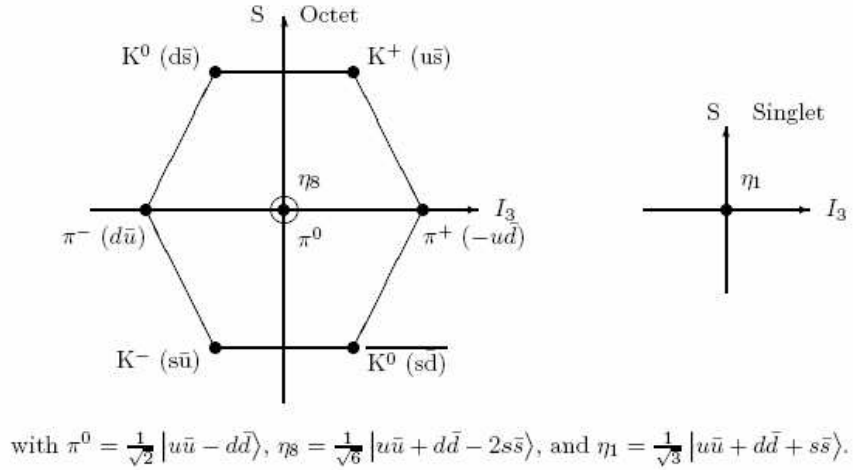
Figure 4: Pseudoscalar Meson Nonet

originating in arguments from group theory. The three states in the center of Figure 4, π^o, η_8, and η_1, carry the same value for the S and I_3 quantum numbers. How do we distinguish between the states $u\bar{u}$, $d\bar{d}$, and $s\bar{s}$ which all correspond to mesons with

23

$S = I_3 = 0$?

The state of a quantum system is defined by the wavefunction [17]. A fundamental postulate of quantum mechanics is the statement that the specification of the wavefunction completely determines all the properties of the system in a given state.

A mixed state can be thought of as a superposition of pure states $\psi^{(i)}$. In our case, the states $u\bar{u}$, $d\bar{d}$ and $s\bar{s}$ are pure states with the same quantum numbers. But the physical states are mixed states, which are linear combinations of the pure states, and it is not possible to identify one quark-antiquark combination with one meson. Since the two states η_8 and η_1 have identical quantum numbers, they can mix [7]. The eigenstates η_8 and η_1 correspond to the physical states η and η'; the degree of mixing in these states is represented by the pseudoscalar mixing angle Θ_{ps}:

$$|\eta\rangle = \cos\Theta_{PS}|\eta_8\rangle - \sin\Theta_{PS}|\eta_1\rangle \tag{1.4.10}$$

$$|\eta'\rangle = \sin\Theta_{PS}|\eta_8\rangle + \cos\Theta_{PS}|\eta_1\rangle \tag{1.4.11}$$

Minimal mixing occurs when $\sin\Theta_{PS} \cong 0.6$. Gluons do not carry flavor, which means that they carry quantum numbers $S = 0$ and $I_3 = 0$. As such, it is possible that gluons, or a state composed solely of gluons known as a glueball, could potentially contribute to the η and η' wave functions. This additional component is referred to as a glue component. To accommodate this new possibility, we extend the mixing scheme to include a glue element.

$$|\eta\rangle = X_\eta \cdot \frac{1}{\sqrt{2}}(u\bar{u} + d\bar{d}) + Y_\eta \cdot (s\bar{s}) + Z_\eta \cdot (glue) \tag{1.4.12}$$

$$|\eta'\rangle = X_{\eta'} \cdot \frac{1}{\sqrt{2}}(u\bar{u} + d\bar{d}) + Y_{\eta'} \cdot (s\bar{s}) + Z_{\eta'} \cdot (glue) \tag{1.4.13}$$

Currently there is no evidence to support glueball content in the η' wavefunction; nevertheless the η' still appears to be produced preferentially in glue-rich processes.

A meson nonet is fully described by four types of particles. The lightest pseudoscalar nonet contains 3 pions, 4 kaons, the η and the η'. In Table 1.4.1 some possible combinations of higher order nonets are shown. Currently, there are more particles than places in the nonets; in particular the light mesons are still ambiguously classified. The spectrum of scalar mesons is of interest since the lowest mass

Table 1.4.1: Possible light meson nonet combinations. The two K_{1A} and K_{1B} mix to form the observed resonances $K_1(1280)$ and $K_1(1400)$. In some cases, mesons still need to be identified. We have borrowed the spectroscopic notation $n^{2s+1}L_J = 1^1S_0$. Here, s is the total spin of the two quarks.

L	S	J	n	$I=1$	$I=1/2$	$I=0$	$I=0$	J^{PC}	$n^{2s+1}L_J$
0	0	0	1	π	K	η'	η	0^{-+}	1^1S_0
0	1	1	1	ρ	K^*	Φ	ω	1^{--}	1^3S_1
1	0	1	1	$b_1(1235)$	K_{1B}	$h_1(1380)$	$h_1(1170)$	1^{+-}	1^1P_1
1	1	0	1	$a_0(????)$	$K_0^*(1430)$	$f_0(????)$	$f_0(????)$	0^{++}	1^3P_0
1	1	1	1	$a_1(1260)$	K_{1A}	$f_1(1510)$	$f_1(1285)$	1^{++}	1^3P_1
1	1	2	1	$a_2(1320)$	$K_2^*(1430)$	$f_2(1525)$	$f_2(1270)$	2^{++}	1^3P_2
2	0	2	1	$\pi_2(1670)$	$K_2(1770)$	$\eta_2(1645)$	$\eta_2(1870)$	2^{-+}	1^1D_2
2	1	1	1	$\rho(1700)$	$K^*(1680)$	$\omega(1650)$	$\Phi(????)$	1^{--}	1^3D_1
2	1	2	1	$\rho_2(????)$	$K_2(1820)$	$\omega_2(????)$	$\Phi_2(1870)$	2^{--}	1^3D_2
2	1	3	1	$\rho_3(1690)$	$K_3^*(1780)$	$\omega_3(1670)$	$\Phi_3(1850)$	3^{--}	1^3D_3
0	0	0	2	$\pi(1370)$	$K_0(1460)$	$\eta(????)$	$\eta(1440)$	0^{-+}	2^1S_0
0	1	1	2	$\rho(1450)$	$K^*(1450)$	$\Phi(1680)$	$\omega(1420)$	1^{--}	2^3S_1

glueball is expected to have quantum numbers $J^{PC} = 0^{++}$. Little is known about the scalar meson spectrum. Experiments have improved the situation, but there is still much controversy surrounding particle states and how are they are classified. Figure 5 shows the nonet for the scalar mesons. There are a number of candidates that

would satisfy the question marked states, but there is no general agreement on which states should go where.
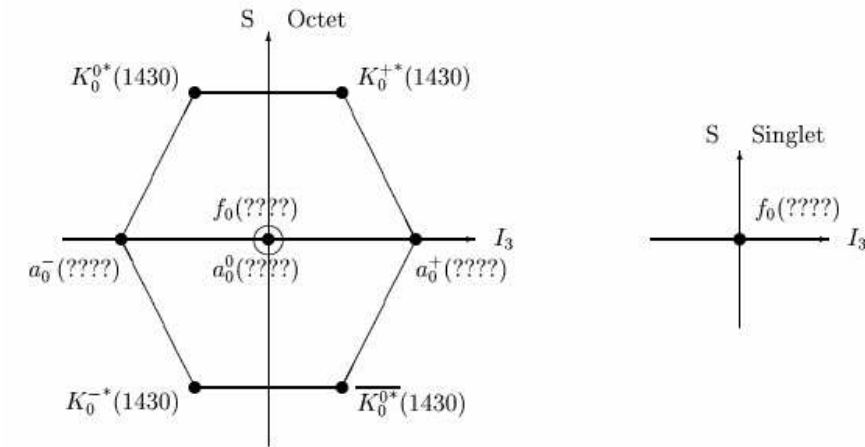
Figure 5: Scalar Meson Nonet

1.5   Glueballs

1.5.1   Definition

The self-coupling of gluons in QCD suggests that additional mesons made of bound gluons, known as glueballs, may exist. Glueballs reflect new degrees of freedom brought into hadron spectroscopy by QCD and are therefore of prime interest [7]. The main motivation of current experiments on meson spectroscopy is the quest to search for glueballs, to establish their non-$q\bar{q}$ character and to determine their properties: masses, total and partial widths, and their mixing with ordinary $q\bar{q}$ states having the same quantum numbers. There are strong candidates for glueballs. The number of

scalar states with $I^G(J^{PC}) = 0^+0^{++}$ seems to be too large for the quark model to accommodate. However, none of the states has decay properties as expected for a pure glueball. Mixing scenarios have been proposed in which the pattern of observed states is understood as quarkonia mixing with a pure glueball. The following discussions on glueballs will focus on the scalar glueball candidates.

1.5.2 Glueball Masses

The most accepted predictions for the glueball mass spectrum are based on lattice gauge calculations. The ground state is a scalar state, at about 1730 MeV; followed by a tensor and pseudoscalar glueball with masses of 2300 and 2350 MeV, respectively. The uncertainty of these calculations is estimated to be of the order of 100 MeV. Figure 6 summarizes the lattice calculations. These mass predictions are supported by other models, such as bag models, flux tubes models, or QCD sum rules. However, some models, such as the bag model, predict lower glueball masses. In addition, the lattice results are in the so-called quenched approximation, which neglect virtual $q\bar{q}$ loops. The glueball mass prediction could be potentially lower when light quarks are taken into account. All of these models agree that the lightest glueball has quantum numbers $J^{PC} = 0^{++}$.

The low-lying glueballs all have quantum numbers which allow mixing with conventional mesons. This mixing is difficult to establish, and even more difficult to rule out.
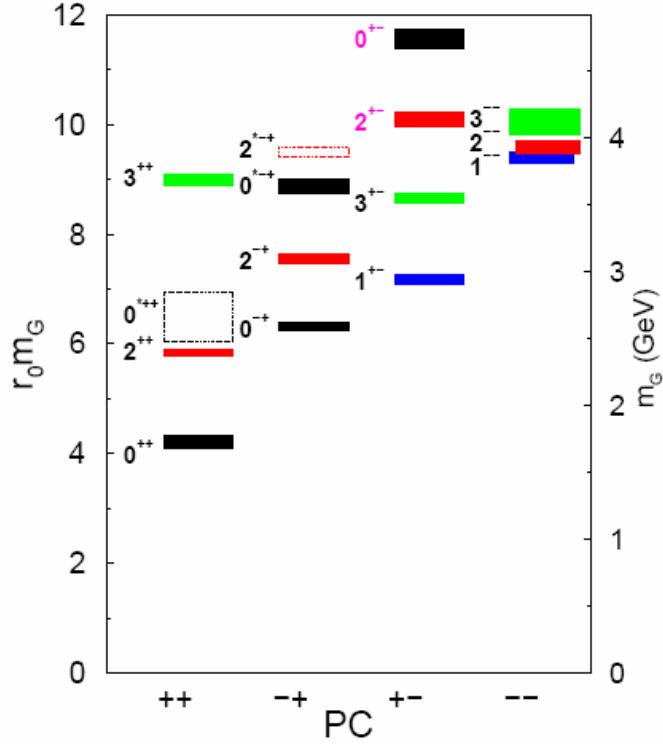
Figure 6: The predicted glueball spectrum from an anisotropic lattice study [19].

1.5.3 Glueball Production and Decay

The 2006 Particle Data Group [18] lists the naive signatures expected for glueballs as (i) no place in $q\bar{q}$ nonets, (ii) enhanced production in gluon-rich channels such as central production and radiative J/ψ (1S) decay, (iii) decay branching fraction incompatible with $SU(3)$ predictions for $q\bar{q}$ states, and (iv) reduced $\gamma\gamma$ coupling.

Since glueballs are expected to carry masses and quantum numbers similar to ordinary mesons, glueballs are difficult to identify. One way to differentiate between the two is to examine the dynamics of their production and decay. There are three production mechanisms that are considered ideal for finding glueballs. The first is

radiative decay $J/\psi \to \gamma G$, where the glueball, G, is formed from intermediate gluons. The second is in central production, where glueballs are produced from pomerons. Pomerons are thought to be particle-like objects made up of gluons. The third is in proton-antiproton annihilation, where the destruction of quarks can lead to the creation of glueballs. These three processes are sketched in Figure 7. Historically,
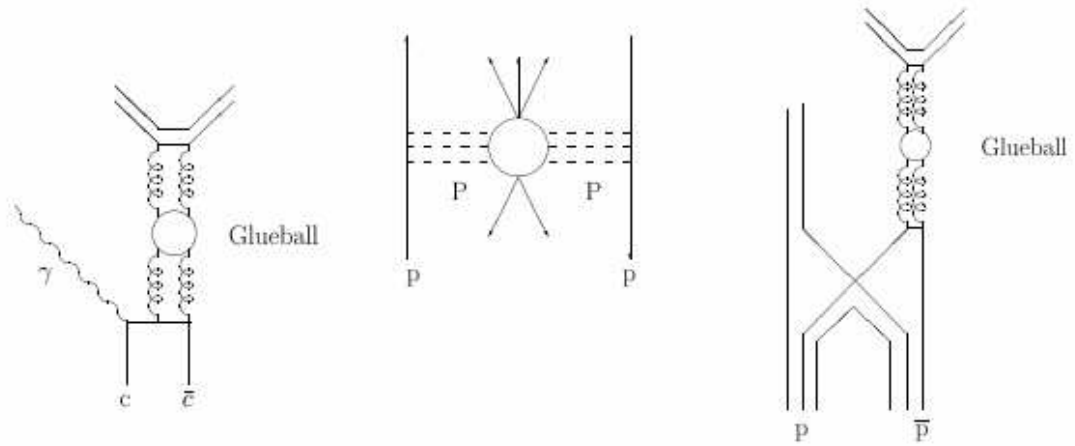
Figure 7: Diagrams potentially leading to the formation of glueballs: radiative J/ψ decays, Pomeron-Pomeron scattering, and $p\bar{p}$ annihilation.

J/ψ radiative decay was the first to present serious glueball candidates. In J/ψ decay the $c\bar{c}$ quarks annihilate into gluons before creating lighter quark pairs to form the final state hadrons [20]. The J/ψ is narrow and has a mass of 3.1 GeV. The J/ψ decays via three gluons or two gluons and a single photon. Two gluons or three gluons can produce a color singlet. In most decays, the J/ψ gives 3 gluons which then hadronize. In the case where the J/ψ decays into two gluons and a photon, the

two gluons can self-interact and form a glueball [21]. It is possible to determine the energy of the two-gluon system by changing the energy of the produced photon. If there is a glueball, then there should be an enhanced production rate of hadrons at that energy.

Central production is another process in which glueballs are thought to be produced abundantly. In central production two hadrons, such as two protons, pass by each other 'nearly untouched.' Each proton is a collection of quarks surrounded by a cloud of gluons [20]. As they approach each other, a color singlet bit of glue gets detached from one proton and is absorbed by the other. This is called Pomeron exchange. Once in awhile, as the two protons approach color single glue from each will be released and these bits may fuse to produce resonance states. These would be preferentially gluonic in nature. The state would decay into hadrons. No valence quarks are exchanged. The process is often called Pomeron-Pomeron scattering. The absence of valence quarks in the production process makes central production a good place to search for glueballs.

In $p\bar{p}$ annihilation, some quarks in the initial proton and antiproton annihilate completely, leaving only gluons, and this subsequently results in light hadrons.

Glueballs do not couple directly to photons and their production should be suppressed in $\gamma\gamma$-processes. Further information is provided by the coupling of the candidate state to $\gamma\gamma$. Gluons can only couple to photons through the creation of an intermediate quark-antiquark pair which is therefore suppressed relative to quark model states.

A pure glueball would not be seen in two photon reactions. This is the motivation for a ratio called *stickiness*. Since a glueball should appear strongly in J/ψ radiative decay, but very weakly in $\gamma\gamma$ reactions, the quantity stickiness for a hadron is the ratio of its branching ratios for the production in J/ψ radiative decays to the decay to $\gamma\gamma$. Pure glueballs should then have large stickiness.

Further distinctive features can be derived from their decays, glueballs are flavor singlets. However, these arguments have to be taken with a grain of salt: mixing of a glueball with mesons having the same quantum numbers can occur and would dilute any selection rule.

Glueball decays are expected to produce flavor symmetric coupling to final-state hadrons [4]. This gives the characteristic flavor singlet branching fraction for pseudoscalar pairs

$$\Gamma(G \to \pi\pi : K\bar{K} : \eta\eta : \eta\eta' : \eta'\eta') = 3 : 4 : 1 : 0 : 1 \,. \tag{1.5.1}$$

The decay into $\eta\eta'$ is forbidden: a singlet cannot decay into a singlet and an octet meson. This selection rule holds even if the state is a mixture of a glueball and a conventional meson: the two mesons η and η' have orthogonal $SU(3)$ flavor states and a flavor singlet cannot decay into two states which are orthogonal.

1.5.4 Scalar Mesons and Scalar Glueballs

Below 2 GeV, there are 19 'established' scalar mesons [18] which are summarized in Table 1.5.1. In addition to these established states, the PDG also lists further states that require confirmation. For example, the $f_0(1200 - 1600)$, if verified, would

Table 1.5.1: Scalar Mesons

$I = 1/2$	$I = 1$	$I = 0$
$\kappa(800)$	$a_0(980)$	$f_0(400 - 1200)$ $f_0(980)$ $f_0(1370)$
$K^*(1430)$	$a_0(1450)$	$f_0(1500)$ $f_0(1710)$

need to find a place among the scalar mesons. There is no agreement on how to interpret the scalar spectrum. More experimental results are needed to clarify the current situation. In the end, only nine states can be accounted for by the quark model. Many models have been suggested to accommodate the remaining states. I will briefly discuss the possible classifications for the above states.

Scalar mesons below 1000 MeV. The light scalar meson states fall below the lattice predictions for the scalar glueball mass. As a result, there are two proposals for the structure of light scalars mesons: a $q\bar{q}$ structure and a $qq\bar{q}\bar{q}$ one. In the latter case there are at least three possible configurations: a meson-meson molecule, a diquark-diquark state and a compact $qq\bar{q}\bar{q}$ state (known as a tetraquark). In addition, there is the possibility that these states contain a glueball component.

The following states, $a_0(980)$, $f_0(600)$, $f_0(980)$, $\kappa(800)$, could form a nonet [7] . As a nonet of 'normal' $q\bar{q}$ mesons, their mass seems to be too low. Instead, these states could be a nonet composed of $qq\bar{q}\bar{q}$ states. Figure 8 sketches a possible tetraquark nonet. Even if all four particles exist, there is no proof they form a nonet. Other possibilities exist where the dynamical origin of the $f_0(600)$, $\kappa(800)$ and of the $a_0(980)$
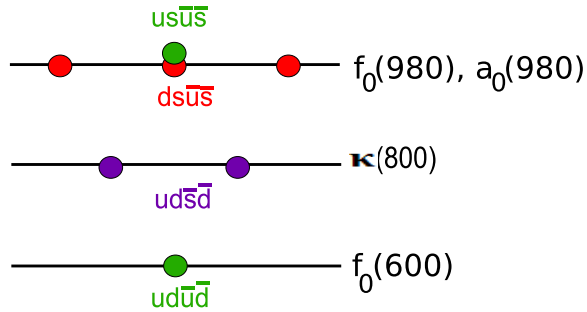
Figure 8: Classification of possible tetraquark mesons. Green denotes $I = 0$ states, purple $I = 1/2$ and red $I = 1$. The vertical axis is mass.

and the $f_0(980)$ are different. The $a_0(980)$ and the $f_0(980)$ are sometimes considered weakly bound states of K and $\bar{K}$; the kaon has an approximate mass of 500 MeV.

In the literature, the above states are not currently discussed as potential glueball candidates since the mass predictions for the lowest scalar glueball from lattice QCD are in the $1500 - 1700$ MeV mass range. However, their precise structure remains controversial.

Scalar mesons above 1000 MeV. Most scalar meson models agree that the $K^*(1430)$ is predominantly the quark model $s\bar{u}$ or $s\bar{d}$ state [18]. The $a_0(1450)$ state carries isospin and is not likely a glueball candidate. The relative couplings to its final states are close to $SU(3)$-flavor predictions for an ordinary $q\bar{q}$ meson. Given this fact, it most likely fits into the scalar meson nonet. The three candidates most discussed as glueball candidates in this mass range fall within or near the mass range predicted by lattice QCD. The three candidates are: the broad $f_0(1370)$, and the comparatively narrow $f_0(1500)$ and $f_0(1710)$. I will briefly discuss how these states stand up to the

glueball signatures listed above. Table 1.5.1 clearly demonstrates the first signature: too many potential candidates for the scalar nonet. If the states below 1000 MeV are dismissed as scalar nonet candidates, as tetraquark states or bound states, then we are left with ten particles for nine places. This is the most common scenario considered. In that case, one of the three states must be a glueball: $f_0(1370)$, $f_0(1500)$, and $f_0(1710)$.

The second signature is concerned with the production of states in gluon-rich processes. As listed above, the gluon-rich processes most discussed are: J/ψ radiative decays, central production, and $p\bar{p}$ annihilations. The $f_0(1370)$ is produced in $p\bar{p}$ annihilations and central collisions. The $f_0(1500)$ has been observed in $p\bar{p}$ annihilations, in central collisions (enhanced production), and in J/ψ radiative decays. The $f_0(1710)$ is seen in J/ψ radiative decays and central production; a large signal is observed in J/ψ radiative decays.

The third signature is related to expected decay products for a glueball, which is a flavor singlet. Table 1.5.2 below summarizes the branching ratios from the 2006 Particle Data Group and the Crystal Barrel experiment for the three states under consideration. As discussed earlier, we expect a glueball candidate to decay with the ratio, $\pi\pi : K\bar{K} : \eta\eta : \eta\eta' : \eta'\eta'$ of $3 : 4 : 1 : 0 : 1$. Therefore, we expect decays to $\eta\eta'$ to be suppressed. For the three candidates under discussion, neither the $f_0(1370)$ and $f_0(1710)$ decay to $\eta\eta'$; however, the $f_0(1500)$ does.

From Table 1.5.2 it can be seen that none of the three states fits the expected decay ratio. From the branching ratios Table 1.5.2, as well as the remainder listed by the

Table 1.5.2: Partial decay widths for $f_0(1370)$, $f_0(1500)$, and $f_0(1710)$.

	$f_0(1370)$	$f_0(1500)$	$f_0(1710)$
Γ_{tot}	~ 350	~ 109	~ 137
$\Gamma_{\pi\pi}$	~ 90	~ 38	~ 5
$\Gamma_{K\bar{K}}$	~ 50	~ 9	~ 52
$\Gamma_{\eta\eta}$	~ 1	~ 6	~ 25
$\Gamma_{\eta\eta'}$		~ 2	
$\Gamma_{\eta'\eta'}$			
$\Gamma_{\gamma\gamma}$	seen	not seen	

Particle Data Group [18], we find that the $f_0(1370)$ and $f_0(1500)$ decay mostly into pions, while the $f_0(1710)$ decays mainly into $K\bar{K}$ final states. Naively, this suggests a $u\bar{u} + d\bar{d}$ structure for the $f_0(1370)$ and $f_0(1500)$ and $s\bar{s}$ for the $f_0(1710)$.

The last signature deals with couplings to photons. Since gluons do not carry electric charge, we do not expect glueballs to be formed from photon collisions nor do we expect a glueball candidate to decay into two photons. A $f_0(1710)$ signal is observed in $\gamma\gamma$ collisions leading to two kaons. The $f_0(1500)$ is not observed in $\gamma\gamma \to K\bar{K}$ nor $\pi^+\pi^-$. The partial width listed for the $f_0(1370)$ to $\gamma\gamma$ is small. The partial width for the $f_0(1500)$ is listed as not seen, and there is nothing listed for the $f_0(1710)$ branching ratio to $\gamma\gamma$.

Looking at the currently excepted members of the scalar nonet, we find an average width of about 300 MeV. The $f_0(1370)$ would then seem like a good candidate for the nonet, with a width of around 350 MeV.

Since none of the candidates in the lattice QCD mass range appear to have all the 'correct' glueball properties, mixing has been suggested as a way to resolve this

problem. The two scalar $q\bar{q}$ states and the scalar glueball have the same quantum numbers; they mix and form the three observed states. Several mixing scenarios have been suggested and some of them are capable of reproducing the decay pattern. However, alternative schemes exist in the literature. In particular, for a scalar glueball, the two-gluon coupling to $n\bar{n}$ appears to be suppressed by chiral symmetry and therefore $K\bar{K}$ decay could be enhanced. Ultimately, more data are needed to clarify the spectrum of scalar mesons.

1.5.5   Meson-Glueball Mixing

Several authors have suggested scenarios in which a scalar glueball mixes with two $q\bar{q}$ states [7]. The mixing angles were partly determined from partial decay widths of the scalar states. All mixing schemes agree that the scalar glueball shows itself in the scalar meson sector and it has a mass, before mixing, of about 1600 MeV. $SU(3)$ symmetry in the decays of scalar meson states is imposed in the fits as well as flavor blindness of the glueball. The mixing schemes do not agree on how the glueball is distributed between the three experimentally observed states. Some of the models assign large $s\bar{s}$ components to the $f_0(1370)$ or $f_0(1500)$, however this is not compatible with the data. Table 1.5.3 lists some of the meson-glueball mixing schemes.

Table 1.5.3: Decomposition of the wave function of three scalar isoscalar states into their quarkonium and glueball contributions in various models.

		Amsler and Close [22]				
$f_0(1370)$	$=$	$0.86\frac{1}{\sqrt{2}}(u\bar{u}+d\bar{d})$	$+$	$0.13s\bar{s}$	$-$	0.50 glueball
$f_0(1500)$	$=$	$0.43\frac{1}{\sqrt{2}}(u\bar{u}+d\bar{d})$	$-$	$0.61s\bar{s}$	$+$	0.61 glueball
$f_0(1710)$	$=$	$0.22\frac{1}{\sqrt{2}}(u\bar{u}+d\bar{d})$	$-$	$0.76s\bar{s}$	$+$	0.60 glueball
		Lee and Weingarten [23]				
$f_0(1370)$	$=$	$0.87\frac{1}{\sqrt{2}}(u\bar{u}+d\bar{d})$	$+$	$0.25s\bar{s}$	$-$	0.43 glueball
$f_0(1500)$	$=$	$-0.36\frac{1}{\sqrt{2}}(u\bar{u}+d\bar{d})$	$+$	$0.91s\bar{s}$	$-$	0.22 glueball
$f_0(1710)$	$=$	$0.34\frac{1}{\sqrt{2}}(u\bar{u}+d\bar{d})$	$+$	$0.33s\bar{s}$	$+$	0.88 glueball
		De-Min Li et al. [24]				
$f_0(1370)$	$=$	$-0.30\frac{1}{\sqrt{2}}(u\bar{u}+d\bar{d})$	$-$	$0.82s\bar{s}$	$+$	0.49 glueball
$f_0(1500)$	$=$	$0.72\frac{1}{\sqrt{2}}(u\bar{u}+d\bar{d})$	$-$	$0.53s\bar{s}$	$-$	0.45 glueball
$f_0(1710)$	$=$	$0.63\frac{1}{\sqrt{2}}(u\bar{u}+d\bar{d})$	$+$	$0.22s\bar{s}$	$+$	0.75 glueball
		Close and Kirk [25]				
$f_0(1370)$	$=$	$-0.79\frac{1}{\sqrt{2}}(u\bar{u}+d\bar{d})$	$-$	$0.13s\bar{s}$	$+$	0.60 glueball
$f_0(1500)$	$=$	$0.62\frac{1}{\sqrt{2}}(u\bar{u}+d\bar{d})$	$+$	$0.37s\bar{s}$	$-$	0.69 glueball
$f_0(1710)$	$=$	$0.14\frac{1}{\sqrt{2}}(u\bar{u}+d\bar{d})$	$+$	$0.91s\bar{s}$	$+$	0.39 glueball
		Celenza et al. [26]				
$f_0(1370)$	$=$	$0.01\frac{1}{\sqrt{2}}(u\bar{u}+d\bar{d})$	$-$	$1.00s\bar{s}$	$-$	0.00 glueball
$f_0(1500)$	$=$	$0.99\frac{1}{\sqrt{2}}(u\bar{u}+d\bar{d})$	$-$	$0.11s\bar{s}$	$+$	0.01 glueball
$f_0(1710)$	$=$	$0.03\frac{1}{\sqrt{2}}(u\bar{u}+d\bar{d})$	$+$	$0.09s\bar{s}$	$+$	0.99 glueball
		M. Strohmeier-Presicek et al. [27]				
$f_0(1370)$	$=$	$0.94\frac{1}{\sqrt{2}}(u\bar{u}+d\bar{d})$	$+$	$0.07s\bar{s}$	$-$	0.34 glueball
$f_0(1500)$	$=$	$0.31\frac{1}{\sqrt{2}}(u\bar{u}+d\bar{d})$	$-$	$0.58s\bar{s}$	$+$	0.75 glueball
$f_0(1710)$	$=$	$0.15\frac{1}{\sqrt{2}}(u\bar{u}+d\bar{d})$	$+$	$0.81s\bar{s}$	$+$	0.57 glueball

CHAPTER II

GLUEBALLS AS TIGHTLY LINKED FLUX TUBES: A REVIEW

2.1 Introduction

The backbone of this thesis is the model of glueballs as tightly knotted or linked flux tubes by Buniy and Kephart [28], which is introduced in this chapter. Each chapter is in some way related to this model. This chapter starts by presenting the model, followed by some additional calculations directly related to the model. The end of the chapter incorporates these new calculations as well as new states and updated state masses from the Particle Data Group into the existing model.

2.2 Knots and links

Before we delve into the model, we first begin with a brief introduction to knots and links. We are all familiar with everyday knots - the kind that we use to tie up parcels, shoelaces, and so on [29]. These knots can be untied, and retied in the same or different ways. By manipulating the string, we can let the "knots" escape.

In mathematics, the term knot means something different than our daily experience. In order to study the properties of knots, the knotted part of the string must be trapped. To visualize this, take a piece of string [30]. Tie a knot in it. Then glue or tape the ends together. This is a mathematical knot. The last step, joining the ends of the rope, is what distinguishes mathematical knots from everyday knots. The

knots studied by mathematicians are always formed on a closed loop, i.e. there are no loose ends.

A simple definition for a mathematical knot is: A knot, K, is a simple closed curve in 3-dimensional space. When talking about knots, the first example is a circle - a planar, round circle. This closed curve is the standard unknotted loop and is known as the trivial knot or the unknot. The overhand knot commonly used to tie string is called a trefoil. It comes in two mirror-image forms, different from each other, labeled left-handed and right-handed, as shown in Figure 9 below. The trefoil, therefore, is an example of a chiral knot. Other knots, such as the figure eight knot, are equivalent

Figure 9: Trefoil knot

to their mirror images; these knots are called achiral knots.

The study of knots and their properties is known as knot theory. Mathematically knots are modeled on the physical variety, and we allow a knot to be deformed as if it were made of a thin, flexible, elastic thread [29]. Two knots are considered equivalent if one can be smoothly transformed into the other [31]. Cutting the knot or allowing it to pass through itself is not allowed.

Knots have been cataloged in order of increasing complexity. Knots are classified

by the minimum number of crossings it contains. For example, a circle has no crossings and the trefoil has three crossings. It is possible to have more than one knot with the same number of crossings [29]. In this case, a subscript is used to denote different knots with the same number of crossings, such as the 5_1 and 5_2 knots in Figure 10. Whereas there is only one knot with four crossings, 4_1, the figure eight knot. Knots

3_1 4_1 5_1 5_2

Figure 10: A few prime knots

such as the square knot, pictured left below, and the granny knot, pictured below right, are usually excluded from knot tables because they can be constructed from simpler knots [31]. Both the Square Knot and the Granny Knot can be deconstructed into two trefoils. Knots that cannot be split into two or more simpler knots are known as prime knots. The trefoil is a prime knot. A link, L, is a collection of knots; the individual knots which make up a link are called the components of the link. The set of links contains the set of knots. We shall restrict the term knot to mean a link of only one component.

Links are also classified by the minimum number of crossings, but also by the number of components it contains. For example, Figure 12 shows the simplest link

Figure 11: Square Knot (left) and Granny Knot (right)

known as the Hopf link which has two components and two crossings. The notation

Figure 12: Hopf Link 2_1^2

for a link is n_l^k, where n represents the number of crossings, k represents the number

of components and l is used to distinguish between links with the same number of

crossings and components. The Hopf link is described as 2_1^2.

2.2.1 Knots and Links in Physics

Knots and links have been of interest to physicists since 1867 when Lord Kelvin

proposed that atoms could be described as knotted vortex tubes in the ether [32]. Of

particular interest is a property called the ropelength of a knot, which is defined as the

quotient of the knot's length and its radius [33]. There is a minimum ropelength for

each knot and link, and the ropelength of that curve is called the ropelength $Rop(L)$

of the knot or link. These minimum ropelength curves are called *tight* knots. Most ropelengths are found by employing numerical methods, however certain types can be exactly calculated. The ropelength results we use for our model are considered tentative upper bounds for knots and links, except for the few cases where the ropelength can be calculated exactly. Comparisons of ropelengths that can be calculated explicitly with numerical methods show a difference of $0.01 - 0.02\%$. For example, the ropelength for a trefoil is computed to be: $Rop(3_1) = 8\pi$.

From a given ropelength one can calculate the so-called "knot energy," which is a topological invariant [34]. The knot energy is proportional to the ropelength, which implies that the tightest knot configuration represents the 'ground-state.' The knot energy is defined to be

$$\epsilon(K) = \frac{Rop(L)}{2a} \tag{2.2.1}$$

where a is the radius of the flux tube. More details about this relationship are given in the next section. If the radius of a tight knot is set to 1, then the knot energy for the trefoil would be given by: $\epsilon(3_1) = 4\pi$.

2.3   The model

We discussed in Chapter I that experiments report more states than the current quark model can support. The lightest glueball states are predicted to carry the same quantum numbers as scalar mesons, $J^{PC} = 0^{++}$, which are defined by the Particle Data Group as f_0 states. Buniy and Kephart [28] modeled all f_0 states as knotted/linked chromoelectric QCD flux tubes.

The first question to address is how could a glueball be related to a *knot* or a *link?* The strong interaction is a result of gluons exchanged by quarks, and at large distances this exchange can be thought of as a tube of colored flux. Imagine a quark and an antiquark connected by a tube of flux. Imagine the quark and antiquark annihilating, leaving behind a circular tube of color flux. If the flux tube crossed over itself before the quark and antiquark annihilated, what remains could be a knotted flux tube. The result would be a knotted lump of energy, or a knotted soliton. By definition, a glueball is a flavorless meson (i.e. a boson) with no valence quarks. These knotted solitons would be considered glueballs.

Knotted magnetic fields, treated as solitons, have been suggested as candidates for a number of plasma phenomena in systems such as astrophysical, atmospheric, and Bose-Einstein condensates. In plasma physics, tight knots and links correspond to metastable minimum energy configurations.

Imagine a hadronic collision that creates a gluonic state in the form of a closed QCD chromoelectric flux tube. The fields in the flux tube quickly relax to an equilibrium configuration, which is topologically equivalent to the initial state. The field relaxes to its minimum energy state. Flux conservation and energy minimization dictate that the fields are homogeneous across the tube cross sections. This process occurs by shrinking the tube length, resulting in a "tight" knot or link. The radial scale is set by Λ_{QCD}^{-1}. The energy of the final state depends only on the topology of the initial state, and is estimated as follows. A knotted tube of radius a and length l has a volume $\pi a^2 l$. Using conservation of flux Ψ_E, the energy can be written as

proportional to $l(tr\Psi_E^2)/(2\pi a^2)$. Setting the radius of the tube to be proportional to Λ_{QCD}^{-1}, the energy is found to be proportional to the length l. This yields the dimensionless quantity defined as the knot energy, given by Equation 2.2.1.

Buniy and Kephart identified knotted and linked QCD flux tubes with glueballs. The lightest candidate is the $f_0(600)$, which is identified with the shortest link, i.e. the 2_1^2. Following this, the $f_0(980)$ is identified with the next shortest knot, the 3_1 trefoil knot. And so on.

2.4 Additional Exact Calculations of Knot/Link Energy

Originally, Buniy and Kephart calculated the energy of links 2_1^2, 4_1^3 and 6_1^4 exactly. These calculations assumed one quanta of flux per tube. We can expand this calculation to include link configurations where one of the components carries two quanta of flux. The following section goes through the details of these calculations.

2.4.1 Energy of link $2_1^2 \# 2_1^2$ where 0_1 carries double flux

We first consider the case of the link $2_1^2 \# 2_1^2$ where one 0_1 carries a single quanta of flux, and the other $0_1'$ component carries two flux quanta. The radius of the flux tube in 0_1 is designated as a. $0_1'$ carries double flux, the cross-sectional area is doubled and we assume constant energy density such that $\pi a^2 \to 2\pi a^2$ so that $a \to \sqrt{2}a$. We will designate the radius of $0_1'$ by $b = \sqrt{2}a$. We will call the ropelength of the flux tube carrying two flux quanta l_1. We will call the ropelength of the flux tube with a single quanta which goes through the interior l_2. And we will call the ropelength of the flux

tube that wraps around the other two l_3. Given these definitions we can write down a relationship for the knot/link energy in terms of ropelength.

$$E = \frac{(2l_1 + l_2 + l_3)}{2a}. \tag{2.4.1}$$

The ropelength of l_1 is found by calculating the circumference of a circle of radius $a+b$, which yields $l_1 = 2\pi(a+b)$. Similarly, the ropelenth of l_2 is found by calculating the circumference of a circle of radius $2a$, which yields $l_2 = 4\pi a$.

The ropelength of l_3 requires a little geometry; the ropelength can be divided into three parts: two equal straight segments, one arclength from a cirle of radius $2a$ (denoted as L_1) and one arclength of radius $a+b$ (denoted as L_2). The length of each straight segment can be found using the Pythagorean theorem, where the hypotonuse is $a + b$, and the short side of the triangle is $b - a$. The long side, which represents the straight segment we are looking for, is calculated as $(2a)\sqrt[4]{2}$. We will use this triangle to find some angles needed to calculate the arclengths. The first arclength is $L_1 = \beta(2a)$, where $\beta = 2\cos^{-1}(\frac{b-a}{a+b})$. The second arclength is $L_2 = \alpha(a + b)$, where $\alpha = \pi + 2\sin^{-1}(\frac{b-a}{a+b})$. The total ropelength is $l_3 = (4a)\sqrt[4]{2} + (\pi + 2\sin^{-1}(\frac{b-a}{a+b}))(a + b) + (2\cos^{-1}(\frac{b-a}{a+b})(2a)$. Plugging this into equation 2.4.1 gives

$$E = \frac{4\pi(a + b) + 4\pi a + 4a\sqrt[4]{2} + (\pi + 2\sin^{-1}(\frac{b-a}{a+b}))(a + b) + (2cos^{-1}(\frac{b-a}{a+b}))2a}{2a}. \tag{2.4.2}$$

Plugging in $b = \sqrt{2}a$, we get

$$E = \frac{4\pi a(2 + \sqrt{2}) + 4a\sqrt[4]{2} + (\pi + 2\sin^{-1}(\frac{\sqrt{2}-1}{1+\sqrt{2}}))a(1 + \sqrt{2}) + (2\cos^{-1}(\frac{\sqrt{2}-1}{1+\sqrt{2}}))2a}{2a}, \tag{2.4.3}$$

45

which reduces to

$$E = 2\pi(2+\sqrt{2}) + 2(\sqrt[4]{2}) + \frac{(\pi + 2\sin^{-1}(\frac{\sqrt{2}-1}{1+\sqrt{2}}))}{2}(1+\sqrt{2}) + (2\cos^{-1}(\frac{\sqrt{2}-1}{1+\sqrt{2}})). \quad (2.4.4)$$

Which numerically reduces to

$$E = 30.8 \qquad\qquad (2.4.5)$$

2.4.2 Energy of link $2_1^2 \# 2_1^2$ where the center loop carries double flux

Next we consider the case of the link $2_1^2 \# 2_1^2$ where the center component carries two flux quanta, and the other two components carry single flux quanta. This configuration is shown in Figure 13. The same definitions apply as above for the radii
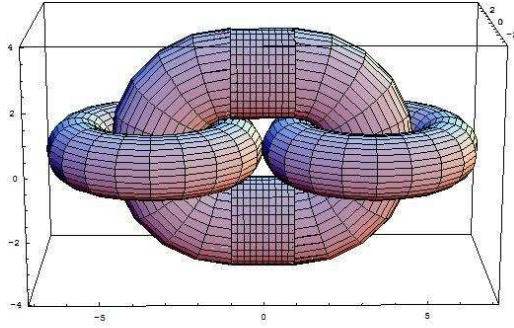
Figure 13: Link $2_1^2 \# 2_1^2$ where the center loop carries double flux.

of the single and double flux tubes. We will call the ropelength of the flux tube with two flux quanta l_1. We will call the ropelength of the flux tubes with a single quanta l_2 and l_3. Given these definitions we can write down a relationship for the knot/link

energy in terms of ropelength.

$$E = \frac{2l_1 + l_2 + l_3}{2a}. \tag{2.4.6}$$

The ropelengths of l_2 and l_3 are equal. $l_2 = l_3 = 2\pi(a+b)$. l_1 contains two semicircles of radius $(a+b)$, and two straight segments of length $2a$. Putting this together yields $l_1 = 2\pi(a+b) + 4a$. Combining these we get

$$E = \frac{4\pi(a+b) + 8a + 4\pi(a+b)}{2a}. \tag{2.4.7}$$

Substituting in $b = \sqrt{2}a$ we find

$$E = \frac{4\pi a(1+\sqrt{2}) + 8a + 4\pi a(1+\sqrt{2})}{2a}. \tag{2.4.8}$$

$$E = 2\pi(1+\sqrt{2}) + 4 + 2\pi(1+\sqrt{2}). \tag{2.4.9}$$

$$E = 4\pi(1+\sqrt{2}) + 4. \tag{2.4.10}$$

$$E = 34.3 \tag{2.4.11}$$

2.5 Averages and Errors

In most cases, the average mass and width used is that stated by the PDG. However, we used some data from the Further States section where experimental data were listed but no average calculated. In this case, we applied the averaging procedures as described in the PDG to the data ourselves.

We averaged the data using the weighted least-squares method. The measurements of a given state are assumed uncoralated, and the weighted average and error

is calculated as

$$m = \bar{x} \pm \delta\bar{x} = \frac{\sum_i w_i x_i}{\sum_i w_i} \pm (\sum_i w_i)^{-1/2}, \qquad (2.5.1)$$

where

$$w_i = \frac{1}{(\delta x_i)^2}. \qquad (2.5.2)$$

Here x_i and δx_i are the value ad error reported by the experiment, and the sums run over the N experiments. We also calculate $\chi^2 = \sum_i w_i(\bar{x}_i - x_i)^2$ and compare it with $N - 1$, which is the expectation value of χ^2 if the measurements are from a Gaussian distribution.

If $\chi^2/(N-1)$ is less than or equal to 1, and there are no known problems with the data, we accept the results.

If $\chi^2/(N-1)$ is greater than 1, but not greatly so, we average the data but increase the quoted error with a scale factor. The scale factor, S, is defined as

$$S = [\chi^2/(N-1)]^{1/2}. \qquad (2.5.3)$$

The scaling procedure for errors does not affect the stated central values and the unscaled error, $\delta\bar{x}$, can be recovered by dividing the quoted error by S.

2.5.1 Averages and Errors Calculations

The $f_0(1200 - 1600)$ state is listed in the Further states section of the Meson Particle Listings. It has been measured three times by two different experiments, and the data is stated as 1323 ± 8 MeV, 1480^{+100}_{-150} MeV and 1530^{+90}_{-250} MeV. We calculate the average mass and the average mass error in Mathematica using the above relationship,

which gives

$$m = 1325 \pm 10 \text{ MeV.} \tag{2.5.4}$$

We compute $\chi^2/(N-1)$, to determine if we need to scale the mass.

$$\chi^2/(N-1) = 5/2. \tag{2.5.5}$$

Since this quantity is larger than 1, we scale the error by the scale factor, S, as defined above. Our final value for $f_0(1200-1600)$ is given as

$$m = 1325 \pm 15 \text{ MeV}, (S = 1.5). \tag{2.5.6}$$

The $f_3(2300)$ state is listed in the Further states section of the Meson Particle Listings. It has been measured twice by different experimental groups, and the data is 2334 ± 25 MeV and 2303 ± 15 MeV. We calculate the average mass and the average mass error in Mathematica using the above relationship, which gives

$$m = 2311 \pm 13 \text{ MeV.} \tag{2.5.7}$$

We compute $\chi^2/(N-1)$ and find that we need to include a scale factor. The final mass is then

$$m = 2311 \pm 14 \text{ MeV}, (S = 1.1). \tag{2.5.8}$$

The $f_0(2330)$ state is listed in the Meson Particle Listings. It has been measured twice by different experiments, and the data listed is 2314 ± 25 MeV and 2337 ± 14 MeV. We calculate the average mass and the average mass error in Mathematica, which gives

$$m = 2332 \pm 12 \text{ MeV.} \tag{2.5.9}$$

We compute $\chi^2/(N-1)$ and find that we do not need a scale factor.

The $f_2(1910)$ state is listed in the Meson Particle Listings. It has been measured three times by different experimental groups and from three different decay modes, the data given is: 1903±9 MeV, 1934±16 MeV and 1941±18 MeV. We calculate the average mass and the average mass error in Mathematica, finding

$$m = 1915 \pm 7 \text{ MeV.} \tag{2.5.10}$$

We compute $\chi^2/(N-1)$ and find that a scale factor is necessary. The final mass is then

$$m = 1915 \pm 12 \text{ MeV}, (S = 1.6). \tag{2.5.11}$$

The $f_2(1430)$ state is listed in the Meson Particle Listings. It has been measured six times by several different experimental groups and from three different decay modes, the data listed is as follows: 1453±4 MeV, 1421±5 MeV, 1480±50 MeV, 1436^{+26}_{-16} MeV, 1412±3 MeV, and 1439^{+5}_{-6} MeV. We calculate the average mass and the average mass error in Mathematica using the above relationship, which gives
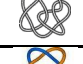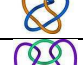
$$m = 1428 \pm 2 \text{ MeV.} \tag{2.5.12}$$

From $\chi^2/(N-1)$ we find it is necessary to include a scale factor. The final mass is then

$$m = 1428 \pm 17 \text{ MeV}, (S = 8.4). \tag{2.5.13}$$

2.6 Results

Table 2.6.1: Comparison between the glueball mass spectrum and knot energies.

State	State Mass (MeV)	Knot/Link	Estimated Knot energy (MeV)	Link Image
$f_0(600)$	$400 - 1200$	2_1^2	758	
$f_0(980)$	980 ± 10	3_1	988	
$f_0(1200 - 1600)$	1325 ± 15	2_1^2	1376	
$f_0(1370)$	$1200 - 1500$	$3_1 \# 2_1^2$	1490	
$f_0(1500)$	1505 ± 6	5_2	1492	
$f_0(1710)$	1724 ± 7	6_2	1721	
$f_0(2020)$	1992 ± 16	9_{49}^2	1993	
$f_0(2060)$	≈ 2060	8_1^2	2066	
$f_0(2100)$	2103 ± 8	9_{42}	2100	
$f_0(2200)$	2189 ± 13	8_4^2	2190	
$f_0(2330)$	2332 ± 12	8_4^3	2348	

In Table 2.6.1, the mass spectrum of the f_0 states is compared with the identified knot and link energies. Since errors for the knot energies were not reported, the error is assumed to be 0.1% percent. A least squares fit to the data gives

$$E(G) = (-0.4 \pm 15.0) + (60.4 \pm 0.5)\epsilon(K) \text{ [MeV]} \qquad (2.6.1)$$

with $\chi^2 = 19.2$ or a reduced $\chi^2 = 2.1$. The data points used in this fit are the f_0

mass values listed in the PDG. Figure 14 shows the relationship between the mass spectrum of the f_0 states and the knot/link energies. We identify the ground state

Figure 14: Relationship between the glueball spectrum $E(G)$ and knot energies $\epsilon(K)$. Each point in the figure represents a glueball identified with a knot or link.

f particles, f_0, with a single knot or link. The excited f states, e.g. f_1, f_2, ..., are identified with a single knot or link that is rotationally excited. The energy of the ground state has already been discussed above; we approximate the excited states by

$$E(f_J) = E(f_0) + \frac{1}{2}J(J+1)\delta. \tag{2.6.2}$$

where we choose the energy step δ as a parameter fit to the data, that is approximately $4 - 5$ MeV. Each table lists the estimated energy for each state based on this relationship, unless otherwise noted.

The data has been analyzed in three tiers, according to how the data is listed by the PDG. We consider the most established states to be those listed in the Meson Summary Table. We label this 'Tier 1', and there are a total of 13 states in it. 'Tier 2' is comprised of the Meson Particle Listings, which contains all the particles from the

52

Meson Summary Table plus some less established states. There are 27 states in Tier 2. Lastly, 'Tier 3' includes states listed in the Further States section which features states requiring further confirmation. There are 36 states in Tier 3. Plots of the fits for each tier are giving in Figures 15, 16 and 17.

For some listed states in the Further States sections, we have used the technique outlined by the PDG to establish an average when necessary. Additional error has been included in the error estimates for excited states to account for uncertainty in the model. The error scales with the reliability of the data used, we included higher error for less established states. As the data becomes more substantiated, this error will reduce. The additional error for Tier 1 data is ± 3, the additional error for Tier 2 data is ± 5, and for the Tier 3 data we added ± 8. A few knot/state or link/state identifications have been changed from Tier 1 to Tier 2 to Tier 3. We fit the data using a least-squares fit and evaluate our fit with a Chi-squared test. Chi-squared is a sum of squares with the general form

$$\chi^2 = \sum_1^N \left(\frac{\text{observed value} - \text{expected value}}{\text{standard deviation}} \right)^2. \tag{2.6.3}$$

More precisely, we define Chi-Squared as follows

$$\chi^2 = \sum_1^N \left(\frac{y_i - f(x_i)}{\sigma_i} \right)^2. \tag{2.6.4}$$

where y_i is the experimentally measured particle mass, and $f(x_i)$ is the knot energy where x_i is the knot energy, ϵ_k. The uncertainties in both quantities are represented in the standard deviation, σ_i. The standard deviation for each knot length is taken as $10^{-3} \times Rop(K)$.

We expect $\chi^2 \leq d$, where d represents the degrees of freedom. In general, the number of degrees of freedom d is defined as the number of observed data, n, minus the number of parameters computed from the data and used in the calculation, c; $d = n - c$. In our case, we have the number of particles minus the slope, the intercept, and delta or $d = n - 3$. If $\chi^2 >> d$, then the measurements do not fit the model.

For the Tier 1 data, we approximate the energy step to be $\delta = 5.1$ and the $\chi^2 = 10.2$. We used 13 particles in the analysis, which would lead us to expect a $\chi^2 \leq 10$. Therefore, the data agrees well with the expected distribution. The slope is 60.8 ± 0.6 and the intercept is -6.4 ± 14.8.

$$E_1(G) = (60.8 \pm 0.6)\epsilon(K) + (-6.4 \pm 14.8) \text{ [MeV]}. \tag{2.6.5}$$

For the Tier 2 data, we estimate the energy step as $\delta = 3.0$ and $\chi^2 = 23.5$. We used 27 particles in the analysis, which would lead us to expect a $\chi^2 \leq 24$. Therefore, the data agrees well with the expected distribution. The slope is 60.5 ± 0.4 and the intercept is 2.0 ± 10.1.

$$E_2(G) = (60.5 \pm 0.4)\epsilon(K) + (2.0 \pm 10.1) \text{ [MeV]}. \tag{2.6.6}$$

Tables 2.7.1 and 2.7.2 contain Tier 3 data.

We approximated the energy step as $\delta = 5.2$ and $\chi^2 = 33.6$. We used 36 particles in the analysis, which would lead us to expect a $\chi^2 \leq 33$. Therefore, the data agrees with the expected distribution. The slope is 59.9 ± 0.4 and the intercept is 9.8 ± 10.9.

$$E_3(G) = (59.9 \pm 0.4)\epsilon(K) + (10.0 \pm 11) \text{ [MeV]}. \tag{2.6.7}$$

2.7 <u>Conclusion</u>

Where can this model go? What further predictions can we make? How can it be expanded? The model makes some predictions that could be confirmed by experimentalists. We predict more f_0 states than are currently observed, each would be associated with a knot or link. Some of the particular predictions from the model are as follows. In addition to predicting a number of ground states, the model allows for a large number of excited states as well. We predict a f_0 particle with a mass of ≈ 1200 MeV with a width that is greater than about 100 MeV. We predict a ground state f meson with a mass of ≈ 1260 MeV and a width of ≈ 185 MeV. We predict a ground state f meson with a mass of ≈ 1271 MeV and a width of ≈ 24 MeV. We predict a ground state f meson with a mass of ≈ 1424 MeV and a width of ≈ 55 MeV. We predict a ground state f meson with a mass of ≈ 1526 MeV and a width of ≈ 134 MeV. We predict a ground state f meson with a mass of ≈ 1640 MeV and a width of ≈ 99 MeV. We predict another f_0 particle with a mass of ≈ 1500MeV with a width that is wider - greater than 100 MeV - than the currently observed $f_0(1500)$. We predict three particles with masses between $\approx 1674 - 1710$ MeV with widths greater than 100 MeV. We predict a particle with a narrow width, less than 100 MeV, of mass ≈ 1710MeV. In addition, the model can be expanded to include the specific symmetry of each knot and link used. If not all of the knots and links used in the model exhibit a spherical symmetry, the predictions for the rotational states as well as the rotational spectrum of the model will change. These ideas are explored in the following four chapters.

Table 2.7.1: Tier 3 Particle Data. Comparison between the glueball mass spectrum and knot energies.

State	Mass (MeV)	Width (MeV)	K^a	$\epsilon(K)^b$	$E(G)^c$ (MeV)
$f_0(600)$	400 - 1200	600 - 1000	2_1^2	$[4\pi]$	$[763]$
$f_0(980)$	980 ± 10	40 - 100	3_1	16.4	991
			4_1^2	20.0	1209
$f_2(1270)$	1275.1 ± 1.2	185 ± 2.9	$2_1^2 \# 2_1^2$	$[6\pi + 2]$	$[1260] + 3\delta$
$f_1(1285)$	1281.8 ± 0.6	24.2 ± 1.1	4_1	21.0	$1271 + \delta$
$\lfloor f_0(1200 - 1600)\rfloor^d$	1325 ± 15	237 ± 20	2_1^2 e	22.8	1374
$f_1(1420)$	1426.3 ± 0.9	54.9 ± 2.6	5_1	23.6	$1424 + \delta$
$\{f_2(1430)\}^f$	1428 ± 17	$13 - 150$	5_1	23.6	$1424 + 3\delta$
$f_0(1370)$	$1200 - 1500$	200 - 500	$(3_1 \# 2_1^2)$	(24.7)	(1490)
$f_0(1500)$	1505 ± 6	109 ± 7	5_2	24.7	1492
$\{f_1(1510)\}$	1518 ± 5	73 ± 25	5_2	24.7	$1492 + \delta$
$f_2(1525)$	1525 ± 5	73^{+6}_{-5}	5_2	24.7	$1492 + 3\delta$
			5_1^2	24.9	1502
$\{f_2(1565)\}$	1562 ± 13	134 ± 8	6_3^3	25.3	$1526 + 3\delta$
$\{f_2(1640)\}$	1639 ± 6	99 ± 60	6_1^3	27.2	$1640 + 3\delta$
			7_7^2	27.8	1674
			$(2_1^2 \# 2_1^2 \# 2_1^2)$ g	$[8\pi + 3]$	$[1696]$
			6_2^2	28.1	1709
			6_1	28.4	1710
$f_0(1710)$	1724 ± 7	137 ± 8	6_2	28.5	1719
			7_8^2	28.9	1742
			6_1^3	28.9	1743
$\lfloor f_2(1750)\rfloor$	1755 ± 10	67 ± 12	6_3	28.9	$1743 + 3\delta$
			$3_1 \# 3_1 *$	28.9	1745
			$3_1 \# 3_1$	29.0	1746
			6_2^3	29.0	1749
			6_3^2	29.1	1751
			$2_1^2 * 2_1^2$	$[8\pi + 4]$	$[1756]$
$\{f_2(1810)\}$	1815 ± 12	197 ± 22	8_7^3	30.3	$1826 + 3\delta$
			8_{19}	30.5	1839
			7_1	30.7	1850
			$2_1^2 \# 2_1^2$ e	$[30.8^g]$	1858
$\{f_2(1910)\}$	1915 ± 12	163 ± 50	8_{20}	31.6	$1901 + 3\delta$
			7_2	31.9	1925
			7_3	32.0	1926
$f_2(1950)$	1944 ± 12	472 ± 18	7_1^2	32.1	$1935 + 3\delta$
			7_4	32.1	1936
			8_{15}^2	32.2	1937
			7_2^2	32.5	1959
			8_8^3	32.5	1959

[a] Notation n_k^l means a link of l components with n crossings, and occurring in the standard table of links (see e.g.) on the kth place. $K \# K'$ stands for the knot product (connected sum) of knots K and K' and $K * K'$ is the link of the knots K and K'.

[b] Values are from [33] except for our exact calculations in 2_1^2, $2_1^2 * 0_1$ and $(2_1^2 * 0_1) * 0_1$ in square brackets, our analytic estimates given in parentheses.

[c] $E(G)$ is obtained from $\epsilon(K)$ using the fit in Figure 17.

[d] States in $\lfloor \rfloor$ brackets are not in the Particle Data Group (PDG) summary tables; they are listed in the Further States section of the Meson Particle listings.

[e] One of the tubes in the link carries double flux.

[f] States in braces are not in the Particle Data Group (PDG) summary tables; they are listed in the Meson Particle listings.

[g] The exact expression for the knot energy is in Equation (2.4.4).

Table 2.7.2: Tier 3 Particle Data. Comparison between the glueball mass spectrum and knot energies. (continued)

State	Mass (MeV)	Width (MeV)	K^a	$\epsilon(K)^b$	$E(G)$ (MeV)
			7_4^2	32.5	1960
$\lfloor f_1(1970) \rfloor$	1971 ± 15	240 ± 45	7_5	32.6	$1966 + \delta$
$f_4(2050)$	2018 ± 11	237 ± 18	7_5	32.6	$1966 + 10\delta$
			7_2^3	32.7	1969
			8_{21}	32.8	1974
			7_7	32.8	1976
			7_6	32.9	1979
			7_1^3	32.9	1982
$\lfloor f_2(2000) \rfloor$	2001 ± 10	312 ± 32	9_{49}^2	33.0	$1990 + 3\delta$
$\{f_0(2020)\}$	1992 ± 16	442 ± 60	9_{49}^2	33.0	1990
$f_2(2010)$	2011 ± 80	202 ± 60	7_5^2	33.1	$1994 + 3\delta$
			9_{43}^2	33.2	1997
			7_6^2	33.2	1998
			8_3^4	33.2	2000
$\lfloor f_3(2050) \rfloor$	2048 ± 8	213 ± 34	8_{16}^3	33.4	$2013 + 6\delta$
			8_4^2	33.7	2031
			9_{53}^2	34.0	2049
			8_1^2	34.2	2062
$\lfloor f_0(2060) \rfloor$	≈ 2060	$50 - 120$	9_{46}	34.3	2067
			$2_1^2 \# 2_1^2$ ^{e}	$[34.3^h]$	2068
			8_{10}^3	34.5	2077
			9_{50}^2	34.7	2088
			9_{61}	33.7	2089
			9_{42}	33.8	2096
$\{f_0(2100)\}$	2103 ± 8	209 ± 19	$3_1 \# 0_1$	34.9	2102
			9_{47}^2	35.0	2106
			8_9^3	35.1	2113
			9_{51}^2	35.3	2125
$\{f_2(2150)\}$	2156 ± 11	167 ± 30	9_{54}^2	35.5	$2138 + 3\delta$
$\lfloor f_2(2140) \rfloor$	2141 ± 12	49 ± 28	8_1	35.5	$2138 + 3\delta$
$\{f_0(2200)\}$	2189 ± 13	238 ± 50	9_{19}^3	36.3	2188
$\{f_4(2300)\}$	2320 ± 60	250 ± 80	8_1^4	37.6	$2266 + 10\delta$
$f_2(2300)$	2297 ± 28	149 ± 141	9_1	37.9	$2279 + 3\delta$
$\lfloor f_3(2300) \rfloor$	2311 ± 13	200 ± 20	9_1	37.9	$2279 + 6\delta$
$\lfloor f_1(2310) \rfloor$	2310 ± 60	255 ± 70	9_{20}^3	38.1	$2293 + \delta$
$f_0(2330)$	2332 ± 12	144 ± 20	8_3^3	38.9	2342
$f_2(2340)$	2339 ± 60	319 ± 80	8_4^3	38.9	$2342 + 3\delta$
$\{f_6(2510)\}$	2465 ± 50	255 ± 40	9_4	39.2	$2359 + 21\delta$

^{a}Notation n_k^l means a link of l components with n crossings, and occurring in the standard table of links (see e.g.) on the kth place. $K \# K'$ stands for the knot product (connected sum) of knots K and K' and $K * K'$ is the link of the knots K and K'.

$^c E(G)$ is obtained from $\epsilon(K)$ using the fit in Figure 2.4.4.

^{d}States in $\lfloor \rfloor$ brackets are not in the Particle Data Group (PDG) summary tables; they are listed in the Further States section of the Meson Particle listings.

^{e}States in braces are not in the Particle Data Group (PDG) summary tables; they are listed in the Meson Particle listings.

^{h}The exact expression for the knot energy is in Equation (2.4.11).
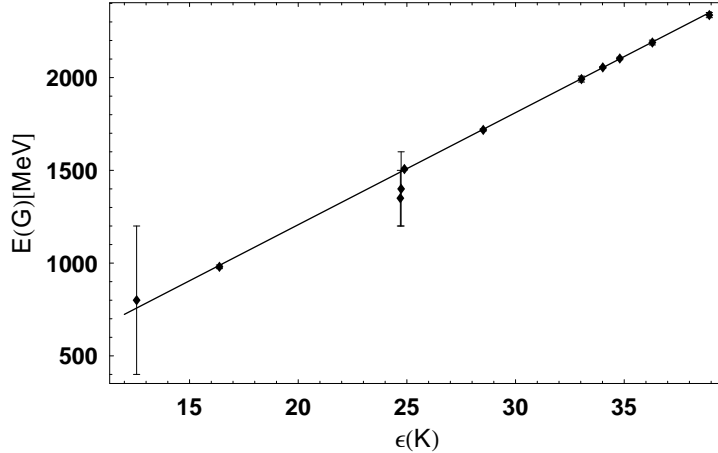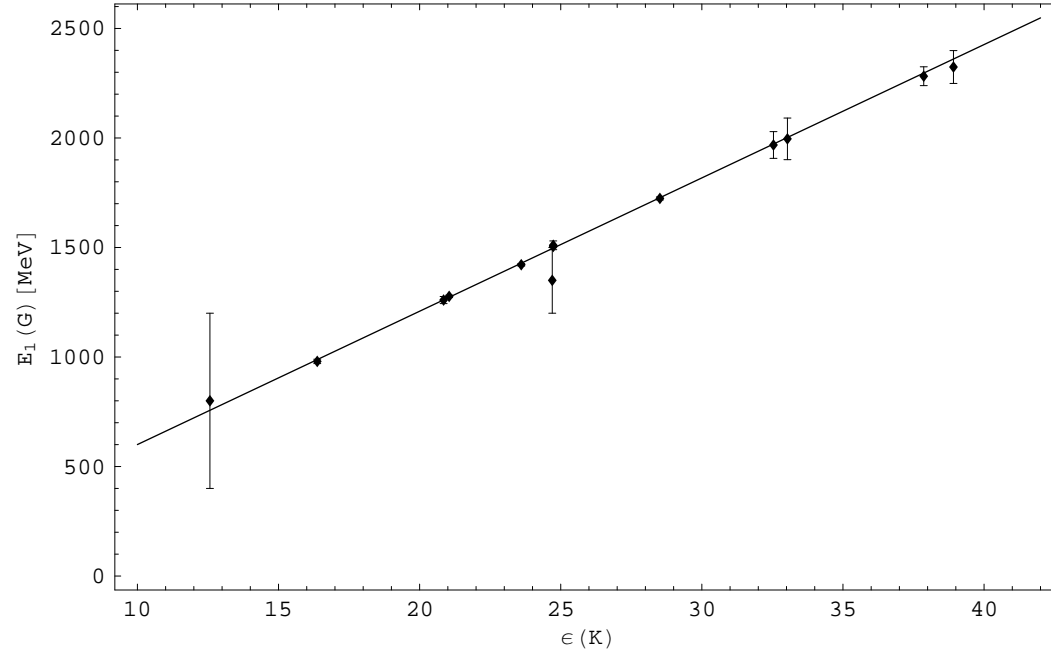
Figure 15: Relationship between the glueball spectrum $E_1(G)$ and knot energies $\epsilon(K)$. Each point represents a glueball identified with a knot or link. The straight line is our model and is drawn for the fit $E_1(G)$
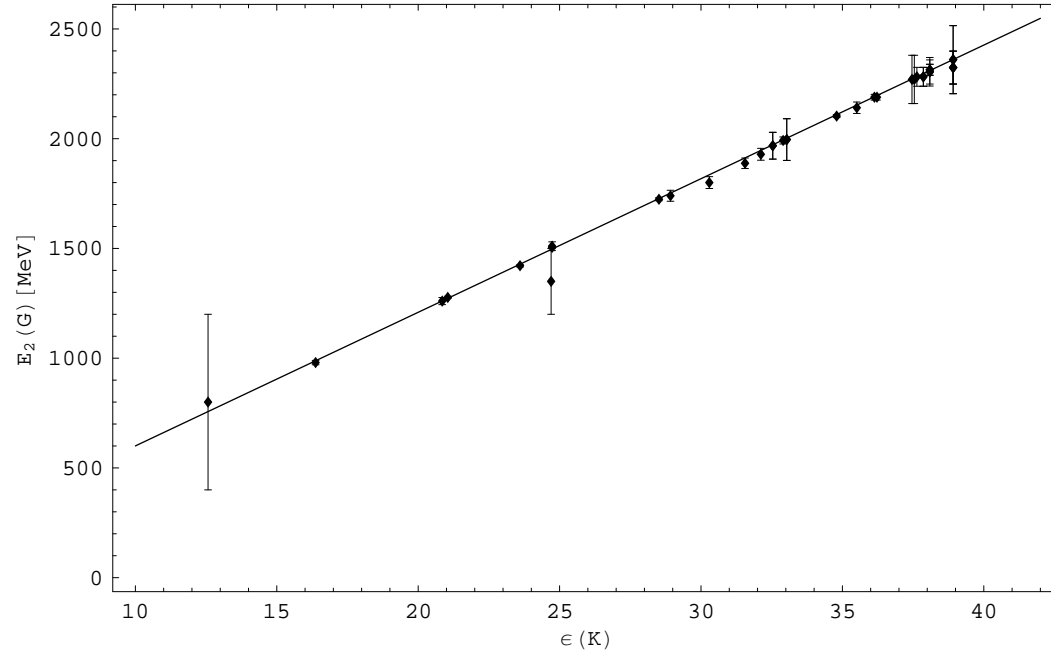
Figure 16: Relationship between the glueball spectrum $E_2(G)$ and knot energies $\epsilon(K)$. Each point represents a glueball identified with a knot or link. The straight line is our model and is drawn for the fit $E_2(G)$
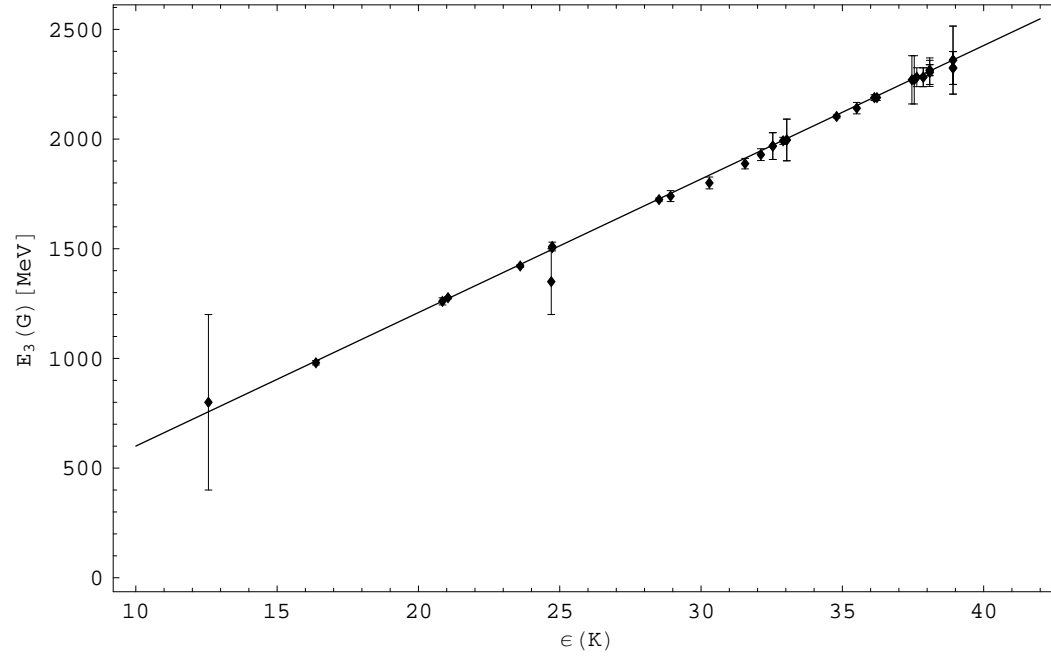
Figure 17: Relationship between the glueball spectrum $E_3(G)$ and knot energies $\epsilon(K)$. Each point represents a glueball identified with a knot or link. The straight line is our model and is drawn for the fit $E_3(G)$.

CHAPTER III

MOMENT OF INERTIA CALCULATIONS FOR SEVERAL GEOMETRIES

3.1 Introduction

In Chpater II we introduced the model of glueballs as tightly knotted or linked flux tubes. A specific knot or link is identified with a glueball ground state, and the excited states are modeled as rotational excitations. In Chapter II we estimated the rotational energy on an approximate spherical symmetry. However, now we would like to determine the actual symmetry of each individual knot and link used in the model. There are a few cases of links where we can calculate the moment of inertia tensor based on the geometry. This chapter details those calculations for several hollow and solid link configurations, and then generalizes the solution for a chain of 'n' elements.

3.2 Exact Calculation of Moment of Inertia Tensor for several geometries

In order to calculate the rotational energy of the tightly knotted and linked flux tubes in our model, we need to determine the inertia tensor of each configuration. We begin with some links where we can use geometry to calculate the moment of inertia tensor exactly. We will examine the remaining cases in Chapter 5. For these few cases, we will look at the link as a composite body where the inertia tensor is found by summing the inertia tensors of its parts, all relative to the same origin. Once we have the moment of inertia tensor, we can calculate the rotational energy as well as

some other useful variables that will allow us to better describe the behavior of a particular link.

3.2.1 Moment of Inertia Tensor

In order to calculate the energy of a rotating body, we need the moment of inertia, which is the rotational equivalent of mass. Physically, the moment of inertia represents how difficult it is to change the angular momentum of an object about a particular axis. The moment of inertia has two forms, the scalar form which is used when the axis of rotation is given, and the more general tensor form where the axis of rotation does not need to be known [35].

Since our model considers the tight links to be chromoelectric flux tubes, we treat all components of the link as solid. In the next section, we will consider an infinitely thin shell link, and discuss its potential applications.

The mathematical definition [36] of the moment of inertia tensor of a solid body with respect to a given axis is given by

$$I = \int_V \rho(x, y, z) r_\perp^2 \, dV \tag{3.2.1}$$

where $\rho = \frac{M}{V}$, is the density and $r_\perp$ is the perpendicular distance from the axis of rotation. If we break I into its constituents, we find

$$I_{ij} = \sum_i m_i (r_i^2 \delta_{ij} - x_{i,j} x_{i,k}) \tag{3.2.2}$$

for a discrete mass distribution, where $r_i^2 = x_i^2 + y_i^2 + z_i^2$ is now the distance to a point, δ_{jk} is the Kronecker delta and $x_{i,1} = x_i$, $x_{i,2} = y_i$ and $x_{i,3} = z_i$.

For a continous mass distibution, which is the case for the links we will be examining more closely in this chapter, we can write I_{ij} as

$$I_{ij} = \int_V \rho(\mathbf{r})(r^2 \delta_j - x_j x_k) dV \qquad (3.2.3)$$

We can expand Equation (3.2.3) by writing it out in Cartesian coordinates, which gives us the following

$$I = \int_V \rho(x, y, z) \mathbf{Q} dx dy dz \qquad (3.2.4)$$

where $\mathbf{Q}$ is a 2nd rank tensor defined as follows

$$\mathbf{Q} = \begin{pmatrix} y^2 + x^2 & -xy & -xz \\ -xy & z^2 + x^2 & -yz \\ -xz & -yz & z^2 + x^2 \end{pmatrix} \qquad (3.2.5)$$

From the above, it can be seen that the moment of inertia tensor is additive.

3.2.2 Moment of Inertia Tensor of a Solid Torus

All of the links we will consider contain at least one toroidal component, so we begin by calculating the inertia tensor of a torus. To calculate the inertia tensor, we parametrize the torus; we define the parametric equations [37] for a torus azimuthally symmetric about the z-axis as

$$x = (c + r \cos \nu) \cos u$$

$$y = (c + r \cos \nu) \sin u$$

$$z = r \sin \nu \qquad (3.2.6)$$

where ν and u run from 0 to 2π, c is the distance from the center of the hole to the center of the torus tube and r goes from 0 to a, where a is the radius of the tube [37]. Figure 18 shows a schematic of a torus with a and c. For a tight link, the radius of the tube is related to c by $c = 2a$. We will express all results in terms of a. The
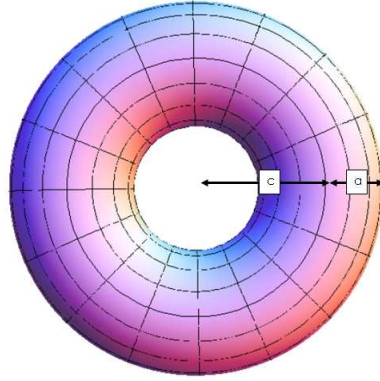
Figure 18: The variables a and c for a torus.

torus corresponding to Equation (3.2.6) is shown in Figure 19. Since the parametric equations are expressed in terms of r, ν and u, we need to express the moment of inertia tensor in terms of these new variables.

$$I^{torus} = \rho \int_0^{2\pi} \int_0^{2\pi} \int_0^a \mathbf{Q} r(2a + r\cos\nu) dr\, du\, d\nu \qquad (3.2.7)$$

where the factor $r(2a + r\cos\nu)$ is the Jacobian. Because we assume the density in the flux tube is constant, we can factor it out of the integral.

Using Equation (3.2.6) in Equation (3.2.7), we calculate the inertia tensor sym-

64

metric about the z-axis to be

$$
\begin{pmatrix}
\frac{21}{2} & 0 & 0 \\
0 & \frac{21}{2} & 0 \\
0 & 0 & 19
\end{pmatrix}
a^5 \pi^2 \rho.
\tag{3.2.8}
$$

In our calculations, we will also need the inertia tensor of a torus azimuthally sym-
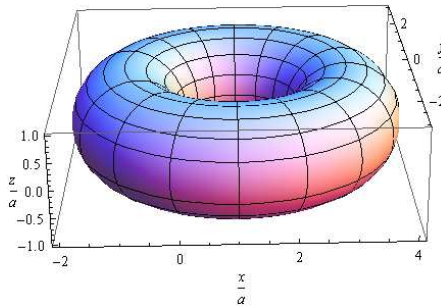
Figure 19: Torus azimuthally symmetric about the z-axis.

metric about the y-axis. The parametric equations are now

$$
\begin{aligned}
x &= (c + r\cos\nu)\cos u \\
y &= r\sin\nu \\
z &= (c + r\cos\nu)\sin u
\end{aligned}
\tag{3.2.9}
$$

Following the same method, we find

$$
\begin{pmatrix}
\frac{21}{2} & 0 & 0 \\
0 & 19 & 0 \\
0 & 0 & \frac{21}{2}
\end{pmatrix}
a^5 \pi^2 \rho.
\tag{3.2.10}
$$

3.2.3 Inertia Tensor for a Solid Hopf Link

The Hopf link consists of two tori linked together, as shown in Figure 20. We can calculate the inertia tensor for the Hopf link using two different methods. We can apply the parallel axis theorem, or we can alter the parametric equations, i.e. Equations (3.2.6) and (3.2.9). We will go through both methods to show that both yield the same results. In future calculations, we will most often employ the parallel axis theorem since it greatly simplifies the calculation.
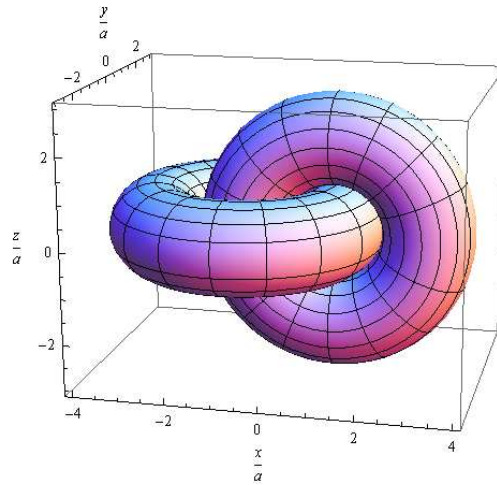
Figure 20: Hopf link in its center of mass system.

Parametric Equations

The Hopf link is composed of two tori. To calculate the inertia tensor of the Hopf link, we will calculate the moment of inertia tensor of each torus and then add them

together since the moment of inertia tensor is additive. We will call the center of mass system of the Hopf link, S. The first torus, T_1, is azimuthally symmetric about the z-axis and its center of mass system, S_1, is shifted in the $+x$ direction by a distance a from O. The second torus, T_2, is azimuthally symmetric about the y-axis and its center of mass system, S_2, is shifted in the $-x$ direction by a distance a from O. Figures 21 and 22 illustrate T_1, T_2, S_1 and I_2. For T_1, the torus is described by the
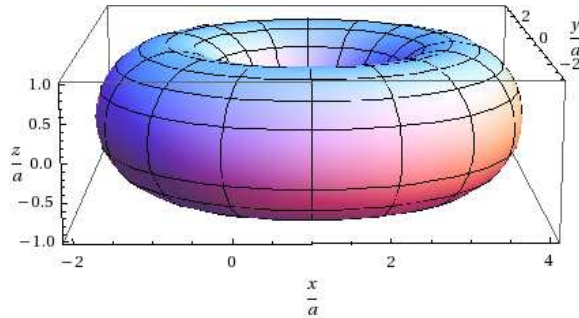
Figure 21: Torus, T_1, centered at $(a, 0, 0)$ in its center of mass system, S_1.

following parametric equations

$$
\begin{aligned}
x &= (2a + r\cos\nu)\cos u + a \\
y &= (2a + r\cos\nu)\sin u \\
z &= r\sin\nu
\end{aligned}
\tag{3.2.11}
$$
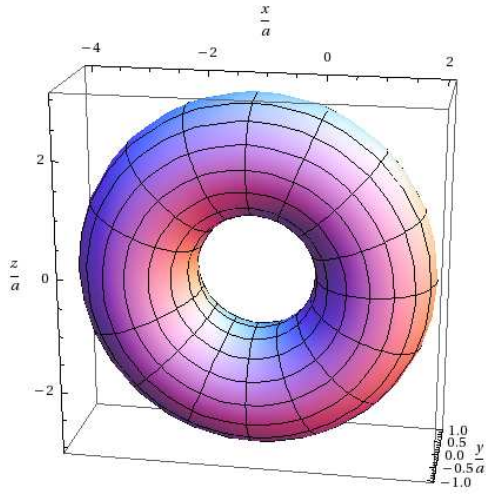
Figure 22: Torus, T_2, centered at $(-a,\, 0,\, 0)$ in its center of mass system, S_2.

We use Mathematica to solve the individual integrals and to calculate the eigenvalues

of the moment of inertia tensor. We find the following result for T_1:

$$I_1 = \begin{pmatrix} \frac{21}{2} & 0 & 0 \\ 0 & \frac{29}{2} & 0 \\ 0 & 0 & 23 \end{pmatrix} a^5 \pi^2 \rho \tag{3.2.12}$$

For T_2, the parametric equations are

$$x = (2a + r\cos\nu)\cos u - a$$

$$y = r\sin\nu$$

$$z = (2a + r\cos\nu)\sin u \tag{3.2.13}$$

And we find the following result for T_2:

$$I_2 = \begin{pmatrix} \frac{21}{2} & 0 & 0 \\ 0 & 23 & 0 \\ 0 & 0 & \frac{29}{2} \end{pmatrix} a^5 \pi^2 \rho \tag{3.2.14}$$

We now add I_1 to I_2 to compute the moment of inertia of the Hopf link, I^{hopf}, in its center of mass frame, S.

$$I^{hopf} = \begin{pmatrix} 21 & 0 & 0 \\ 0 & \frac{75}{2} & 0 \\ 0 & 0 & \frac{75}{2} \end{pmatrix} a^5 \pi^2 \rho \tag{3.2.15}$$

Parallel Axis Theorem

Alternately, we can use the parallel axis theorem to calculate the inertia tensor for the Hopf link. We denote the origin of the x-, y-, z-axes as O, and the inertia tensor for the link in this system as I_O. For the individual tori that make up the Hopf link, we start in their center of mass frame denoted by the x'-, y'-, z'-axes; the inertia tensor for each tori in its center of mass frame is given by I_{CM}. Figure 23 sketches these two frames. The following describes the relationship between the inertia tensor, I_O, relative to an arbitrary origin, O, in terms of the inertia tensor, I_{CM}, relative to the center of mass. Let $\mathbf{r}$ and $\mathbf{r}'$ be position vectors of any point P in the body relative to O and the center of mass of the individual tori respectively, and let $\mathbf{R}$ be the coordinate of the center of mass system relative to O,

$$\mathbf{r} = \mathbf{r}' + \mathbf{R}. \tag{3.2.16}$$

69

The relationship between I_O and I_{CM} is then defined as

$$I_O = I_{CM} + M(R^2\mathbf{1} - \mathbf{R} \otimes \mathbf{R}). \tag{3.2.17}$$

Where $\mathbf{1}$ is the 3×3 identity matrix and $\mathbf{R} \otimes \mathbf{R}$ is their outer product which refers to the tensor product of two vectors. In our case, we have already calculated I_{CM}
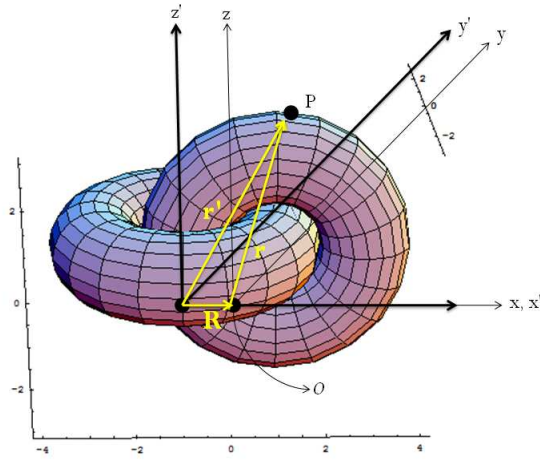
Figure 23: The x-, y-, z-axes and the x'-, y'-, z'-axes for the Hopf link.

for both tori of the Hopf link; the inertia tensor in the center of mass for a torus azimuthally symmetric about the z-axis is given by (3.2.8) and the inertia tensor in the center of mass for a torus azimuthally symmetric about the y-axis is given by (3.2.10). In order to use Equation (3.2.16), we need to determine the mass, M, of a solid torus in terms of its density. $M = \rho V = 4\pi^2 a^3 \rho$, where the volume of the torus is computed to be $V = 2\pi^2 a^2 c = 4\pi^2 a^3$ since $c = 2a$. We need to apply Equation (3.2.17) to find the inertia tensor relative to the x-, y-, z-axes with origin at O.

The coordinates for the torus azimuthally symmetric about the z-axis in its center

70

of mass system are (0, 0, 0), and the coordinates in the center of mass system of the Hopf Link are $(-a, 0, 0)$. As a result, we determine that $\mathbf{R} = -a\mathbf{i}$, where $\mathbf{i}$ is a unit vector in the x direction. Given these values, we can determine Iz_O^{torus}:

$$
\begin{aligned}
Iz_O^{torus} &= Iz^{torus} + M((-a)^2\mathbf{1} - (-a)^2\mathbf{ii}) = \\
&= \begin{pmatrix} \frac{21}{2}a^5 & 0 & 0 \\ 0 & \frac{21}{2}a^5 + 4a^3(-a)^2 & 0 \\ 0 & 0 & 19a^5 + 4a^3(-a)^2 \end{pmatrix} \pi^2\rho \quad (3.2.18)
\end{aligned}
$$

which can be simplified to

$$
Iz_O^{torus} = \begin{pmatrix} \frac{21}{2} & 0 & 0 \\ 0 & \frac{29}{2} & 0 \\ 0 & 0 & 23 \end{pmatrix} a^5\pi^2\rho \quad (3.2.19)
$$

The coordinates for the torus azimuthally symmetric about the y-axis in its center of mass system are (0, 0, 0), and the coordinates in the center of mass system of the Hopf Link are $(a, 0, 0)$. As a result, we determine that $\mathbf{R} = a\mathbf{i}$. Again, we can determine Iy_O^{torus} to be

$$
\begin{aligned}
Iy_O^{torus} &= Iy^{torus} + M(a^2\mathbf{1} - a^2\mathbf{ii}) = \\
&= \begin{pmatrix} \frac{21}{2}a^5 & 0 & 0 \\ 0 & 19a^5 + 4a^3(a^2) & 0 \\ 0 & 0 & \frac{21}{2}a^5 + 4a^3(a^2) \end{pmatrix} \pi^2\rho \quad (3.2.20)
\end{aligned}
$$

or simplified to

$$Iy_O^{torus} = \begin{pmatrix} \frac{21}{2} & 0 & 0 \\ 0 & 23 & 0 \\ 0 & 0 & \frac{29}{2} \end{pmatrix} a^5 \pi^2 \rho \tag{3.2.21}$$

Adding both tori together gives us the same result as (3.2.15), showing that both methods yield the same inertia tensor.

Solid Hopf Link with Double Flux

In addition to the Hopf link described above, our model uses the particular case of a Hopf link where one of the tori has double flux. We can also calculate the inertia tensor for this configuration. The procedure is identical to the Hopf link; but the distances by which the parametric equations are moved will be different. Assuming both tubes have the same field density, the radius of the torus with double flux is $b = \sqrt{2}a$. The value of c for both tori then becomes $c = a + b = a + \sqrt{2}a$. An image of this configuration is shown in Figure 24. We will call the torus with double flux, T_1^{double}, and its parametric equations are

$$
\begin{aligned}
x &= (a + \sqrt{2}a + r\cos\nu)\cos u - \sqrt{2}a \\
y &= (a + \sqrt{2}a + r\cos\nu)\sin u \\
z &= r\sin\nu
\end{aligned}
\tag{3.2.22}
$$

where, in this case, r goes from 0 to b. We input the parametric equations and solve the individual integrals in Mathematica to find the final form for the moment of

72
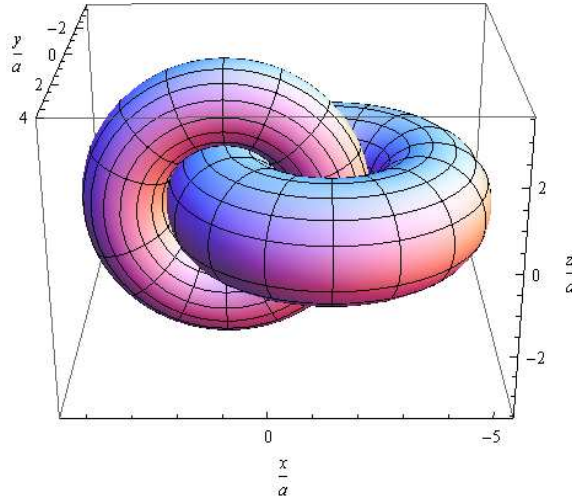
Figure 24: Hopf link where one torus has double flux.

inertia tensor. We find the following for a torus with double flux

$$
I_1^{double} = \begin{pmatrix} \frac{1}{4}(33 + 25\sqrt{2}) & 0 & 0 \\ 0 & \frac{1}{2}(39 + 31\sqrt{2}) & 0 \\ 0 & 0 & \frac{1}{4}(49 + 41\sqrt{2}) \end{pmatrix} a^5\pi^2\rho \qquad (3.2.23)
$$

The second torus, T_2^{double}, does not carry double flux. And, its parametric equations are

$$
\begin{aligned}
x &= (a + \sqrt{2}a + r\cos\nu)\cos u + a \\
y &= r\sin\nu \\
z &= (a + \sqrt{2}a + r\cos\nu)\sin u
\end{aligned}
$$

(3.2.24)

where r goes from 0 to a. We calculate the moment of inertia tensor to be

$$I_2^{double} = \begin{pmatrix} 19 + 15\sqrt{2} & 0 & 0 \\ 0 & 23 + 19\sqrt{2} & 0 \\ 0 & 0 & 2(19 + 15\sqrt{2}) \end{pmatrix} a^5\pi^2\rho \qquad (3.2.25)$$

The inertia tensors of both tori can be added, and we find the inertia tensor for the Hopf link with double flux to be

$$I^{double} = \begin{pmatrix} \frac{1}{4}(109 + 85\sqrt{2}) & 0 & 0 \\ 0 & \frac{1}{2}(85 + 69\sqrt{2}) & 0 \\ 0 & 0 & \frac{1}{4}(201 + 161\sqrt{2}) \end{pmatrix} a^5\pi^2\rho \quad (3.2.26)$$

3.2.4   Inertia Tensor for a solid chain of 3, 4, 5, and 6 links

Our approach for the inertia tensor of a chain of links will be to calculate the two repeating components of a chain, a torus and a stretched torus, rotate and shift the appropriate components and then add up all of the individual chain link parts. We calculate a few simple chains, and then we generalize the process for a chain of 'n' links.

The inertia tensor for a torus has already been calculated. In addition, we need a stretched torus azimuthally symmetric about the y-axis which can be constructed from two half tori and two cylinders as shown in Figure 25. We will compute the inertia tensor for these individual parts, and then add them together to obtain the inertia tensor of the stretched torus. Let's examine the cylindrical components first. Both cylinders are of length $2a$ and radius a. The parametric equations for a cylinder

74
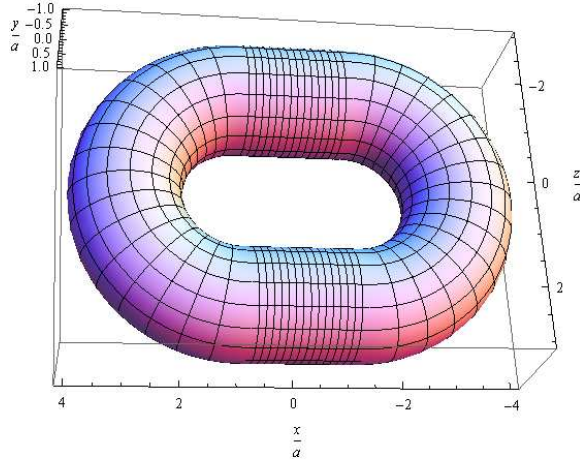
Figure 25: Stretched torus made up of two cylinders and two half tori.

are given by

$$
\begin{aligned}
x &= x \\
y &= r\sin\theta \\
z &= r\cos\theta
\end{aligned}
\tag{3.2.27}
$$

where θ goes from 0 to 2π, x goes from $-a$ to a and r goes from 0 to a.

The form of the moment of inertia tensor is

$$
I^{cyl} = \rho \int_{-a}^{a} \int_{0}^{2\pi} \int_{0}^{a} \mathbf{Q} r \, dr \, d\theta \, dx
\tag{3.2.28}
$$

Which gives an inertia tensor for the cylinder in its center of mass frame of

$$
I_{CM}^{cyl} =
\begin{pmatrix}
1 & 0 & 0 \\
0 & \frac{7}{6} & 0 \\
0 & 0 & \frac{7}{6}
\end{pmatrix}
a^5 \pi \rho
\tag{3.2.29}
$$

75

This represents the inertia tensor for the cylinder in its center of mass coordinate system. Now, we would like to find the inertia tensor about O. As before, we utilize (3.2.17) to find the inertia tensor about O. We need to determine the mass, M, of a solid cylinder in terms of its density. $M = \rho V = 2\pi a^3 \rho$; the volume of the torus is computed to be $V = \pi R^2 h = 2\pi a^3$, where R is the radius of the cylinder and h is the height of the cylinder. We have two cylindrical components, one at $z = 2a$ and one at $z = -2a$. The coordinate system needs to be shifted up and down, respectively, by $2a$ in the z-direction. Moving the coordinate system in the z-direction by a distance of $2a$ gives us

$$I_O^{cyl} = \begin{pmatrix} a^5 + 2a^3(2a)^2 & 0 & 0 \\ 0 & \frac{7}{6}a^5 + 2a^3(2a)^2 & 0 \\ 0 & 0 & \frac{7}{6}a^5 \end{pmatrix} \pi\rho \qquad (3.2.30)$$

which simplifies to

$$I_O^{cyl} = \begin{pmatrix} 9 & 0 & 0 \\ 0 & \frac{55}{6} & 0 \\ 0 & 0 & \frac{7}{6} \end{pmatrix} a^5 \pi\rho \qquad (3.2.31)$$

Moving the coordinate system in the $-z$ direction by a distance of $2a$ gives us the same result as Equation (3.2.31). Next, we need to examine the two half tori components. We first change the limits of the inertia integral of the torus defined in Equation (3.2.7): the variable u now ranges from $-\frac{\pi}{2}$ to $\frac{\pi}{2}$ instead of from 0 to 2π. This change will produce the right-hand half of the torus. In addition, we need to find its center of mass. Due to symmetry, we know that the center of mass will be along the x-axis.

We calculate the x-component of the center of mass as follows

$$X_{CM} = \frac{1}{M} \int_0^{2\pi} \int_{-\frac{\pi}{2}}^{\frac{\pi}{2}} \int_0^a \rho x r (2a + r \cos \nu) \, dr \, du \, d\nu \qquad (3.2.32)$$

where x is as defined in (3.2.9) and M is the mass of half of a torus, which in terms of the density can be written as $M = 2\pi^2 a^3 \rho$. We find the center of mass for the right-hand half torus to be $(-\frac{17a}{4\pi}, 0, 0)$. Knowing the center of mass, we can now define the parametric equations for the half-torus so that we can calculate its inertia tensor in the center of mass frame. The parametric equations for the right-hand torus are

$$x = (2a + r \cos \nu) \cos u - \frac{17a}{4\pi}$$

$$y = (2a + r \cos \nu) \sin u$$

$$z = r \sin \nu \qquad (3.2.33)$$

In order to find the left-hand half of the torus, we make the following change $x \to -x$. Due to symmetry, however, both halves yield the same inertia tensor.

$$I_{CM}^{\frac{1}{2}torus} = \begin{pmatrix} \frac{21\pi^2}{4} & 0 & 0 \\ 0 & \frac{1}{8}(76\pi^2 - 289) & 0 \\ 0 & 0 & \frac{1}{8}(42\pi^2 - 289) \end{pmatrix} a^5 \rho \qquad (3.2.34)$$

Since the origin of the primed system is at $x = a$, we again use (3.2.17) to obtain the inertia tensor about O, relative to x-, y-, z-axes with origin at O:

$$I_O^{\frac{1}{2}torus} = \begin{pmatrix} \frac{21\pi}{4} & 0 & 0 \\ 0 & \frac{1}{2}(23\pi + 34) & 0 \\ 0 & 0 & \frac{1}{4}(29\pi + 68) \end{pmatrix} a^5 \pi \rho \qquad (3.2.35)$$

77

We can now add the inertia tensors for the top and bottom cylinders and the right-
and left-hand half-tori, and we obtain

$$Iy_O^{stretched} = \begin{pmatrix} 18 + \frac{21\pi}{2} & 0 & 0 \\ 0 & \frac{1}{3}(69\pi + 157) & 0 \\ 0 & 0 & \frac{1}{6}(87\pi + 218) \end{pmatrix} a^5\pi\rho \qquad (3.2.36)$$

This represents the inertia tensor of a stretched torus azimuthally symmetric about
the y-axis. We can rotate the coordinate system to obtain the inertia tensor of a
torus azimuthally symmetric about the z-axis, and we find

$$Iz_O^{stretched} = \begin{pmatrix} 18 + \frac{21\pi}{2} & 0 & 0 \\ 0 & \frac{1}{6}(87\pi + 218) & 0 \\ 0 & 0 & \frac{1}{3}(69\pi + 157) \end{pmatrix} a^5\pi\rho \qquad (3.2.37)$$

<u>Solid Link $2_1^2 \# 2_1^2$</u>

We will calculate the link $2_1^2 \# 2_1^2$, a link used in our model for which we do not
have vertex points. $2_1^2 \# 2_1^2$ can be imagined as stretching one of the tori in the Hopf
link and putting another torus through it as shown in Figure 26. Our components
consist of two tori azimuthally symmetric about the z-axis centered at $x = 3a$ and
$x = -3a$ respectively, and one stretched torus azimuthally symmetric about the y-axis
centered at the origin. For left-hand torus, we need to shift the coordinate system
from $x = -3a$ to $x = 0$ to find the inertia tensor of the torus relative to the x-, y-,
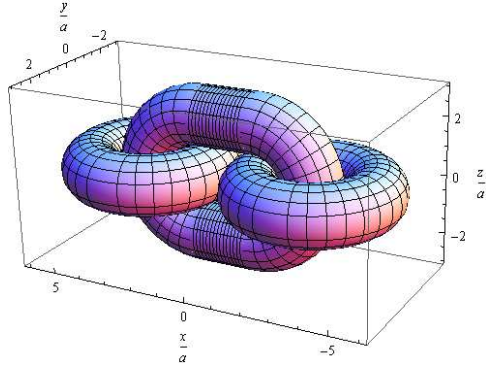
Figure 26: Link $2_1^2 \# 2_1^2$

z-axes relative to O. Using Equation (3.2.17), we obtain

$$
Iz_O^{torus} = \begin{pmatrix} \frac{21}{2} & 0 & 0 \\ 0 & \frac{93}{2} & 0 \\ 0 & 0 & 55 \end{pmatrix} a^5 \pi^2 \rho \tag{3.2.38}
$$

We obtain the same result for the right-hand torus, whose coordinate system is shifted

from $x = 3a$ to $x = 0$. We can now add up the three separate components of the link,

$I_O^{2_1^2 \# 2_1^2} = Iy_O^{stretched} + 2(Iz_O^{torus})$, to obtain the inertia tensor about O for $2_1^2 \# 2_1^2$

$$
I_O^{2_1^2 \# 2_1^2} = \begin{pmatrix} \frac{9}{2}(4 + 7\pi) & 0 & 0 \\ 0 & \frac{1}{3}(348\pi + 157) & 0 \\ 0 & 0 & \frac{1}{6}(747\pi + 218) \end{pmatrix} a^5 \pi \rho \tag{3.2.39}
$$

<u>Solid Link with 4 components</u>

A link with four components centered with origin at O consists of a torus az-

imuthally symmetric about the y-axis centered at $x = -5a$, a torus azimuthally sym-

79

metric about the z-axis centered at $x = 5a$, a stretched torus azimuthally symmetric about the z-axis centered at $x = -2a$ and a stretched torus azimuthally symmetric about the y-axis centered at $x = 2a$. This link is shown in Figure 27. To find the in-
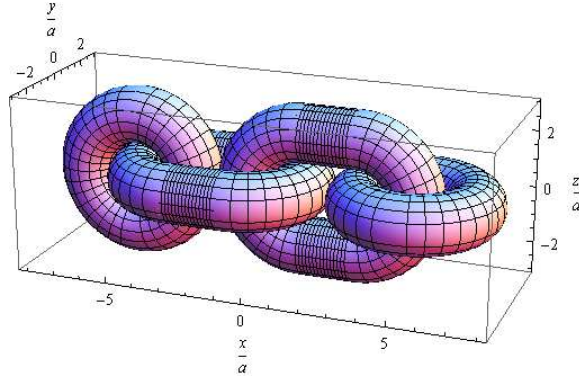
Figure 27: Link with four components.

ertia tensor about O, we go through the steps outlined previously. We summarize the results. For the torus azimuthally symmetric about the z-axis centered at $x = -5a$, we find

$$Iz_O^{torus} = \begin{pmatrix} \frac{21}{2} & 0 & 0 \\ 0 & \frac{221}{2} & 0 \\ 0 & 0 & 119 \end{pmatrix} a^5 \pi^2 \rho \qquad (3.2.40)$$

For the torus centered at $x = 5a$, we find

$$Iy_O^{torus} = \begin{pmatrix} \frac{21}{2} & 0 & 0 \\ 0 & 119 & 0 \\ 0 & 0 & \frac{221}{2} \end{pmatrix} a^5 \pi^2 \rho \qquad (3.2.41)$$

80

For the stretched torus azimuthally symmetric about the z-axis centered at $x = -2a$, we find

$$Iz_O^{stretchedtorus} = \begin{pmatrix} 18 + \frac{21\pi}{2} & 0 & 0 \\ 0 & \frac{1}{6}(314 + 183\pi) & 0 \\ 0 & 0 & \frac{1}{3}(205 + 117\pi) \end{pmatrix} a^5 \pi \rho \quad (3.2.42)$$

And, for the stretched torus centered at $x = 2a$, we find

$$Iy_O^{stretchedtorus} = \begin{pmatrix} 18 + \frac{21\pi}{2} & 0 & 0 \\ 0 & \frac{1}{3}(205 + 117\pi) & 0 \\ 0 & 0 & \frac{1}{6}(314 + 183\pi) \end{pmatrix} a^5 \pi \rho \quad (3.2.43)$$

The inertia tensors of all the components may be added, and for the 4-component link we obtain

$$I_O^{4-link} = \begin{pmatrix} 6(6 + 7\pi) & 0 & 0 \\ 0 & \frac{1}{3}(362 + 897\pi) & 0 \\ 0 & 0 & \frac{1}{3}(362 + 897\pi) \end{pmatrix} a^5 \pi \rho \quad (3.2.44)$$

Solid Link with 5 components

A link with five components centered at the origin, O, consists of a torus azimuthally symmetric about the y-axis centered at $x = -7a$ and at $x = 7a$, a stretched torus azimuthally symmetric about the y-axis centered at $x = 0$ and two stretched tori azimuthally symmetric about the z-axis centered at $x = -4a$ and $x = 4a$. The link is shown in Figure 28. Following the same process as above, we just report the
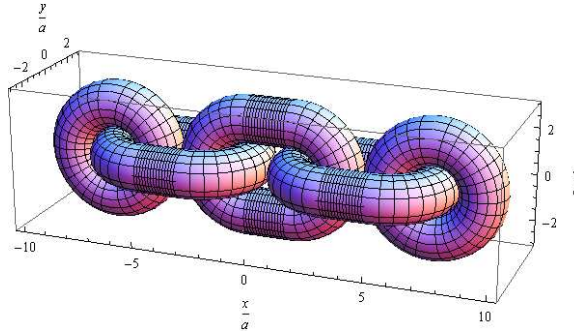
Figure 28: Link with five components.

resultant inertia tensor

$$I_O^{5-link} = \begin{pmatrix} \frac{1}{2}(108 + 105\pi) & 0 & 0 \\ 0 & \frac{1}{2}(538 + 1203\pi) & 0 \\ 0 & 0 & (253 + 610\pi) \end{pmatrix} a^5 \pi \rho \quad (3.2.45)$$

Solid Link with 6 components

A link with six components centered at the origin, O, consists of a torus azimuthally symmetric about the y-axis centered at $x = -9a$, a torus azimuthally symmetric about the z-axis centered at $x = 9a$, two stretched torus azimuthally symmetric about the y-axis centered at $x = -2a$ and $x = 6a$, and two stretched tori azimuthally symmetric about the z-axis centered at $x = 2a$ and $x = -6a$. This link is shown in Figure 29 Following the same process as above, we just report the resultant
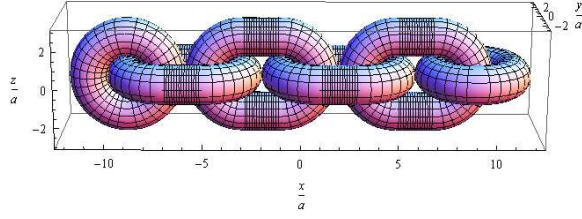
Figure 29: Chain link with six components.

inertia tensor

$$I_O^{6-link} = \begin{pmatrix} 9(8+7\pi) & 0 & 0 \\ 0 & \frac{1}{6}(2984+6435\pi) & 0 \\ 0 & 0 & \frac{1}{6}(2984+6435\pi) \end{pmatrix} a^5\pi\rho \quad (3.2.46)$$

3.2.5 Generalization of the Inertia Tensor for a solid chain of 'n' components

We would like to generalize the relationship for the inertia tensor of a chain with 'n' components. We define the generalized inertia tensor as follows

$$I_O^{n-link} = \begin{pmatrix} I_{xx} & 0 & 0 \\ 0 & I_{yy} & 0 \\ 0 & 0 & I_{zz} \end{pmatrix} a^5\pi\rho \quad (3.2.47)$$

For a chain with an odd number of components, we notice that $I_{xx} \neq I_{yy} \neq I_{zz}$. Whereas, given a chain with even number of components, we find that $I_{yy} = I_{zz}$. We will divide our generalizations into odd and even 'n'. For both even and odd n, the I_{xx} component can be generalized as

$$I_{xx} = 21\pi + (n-2)\left(18 + \frac{21\pi}{2}\right) \quad (3.2.48)$$

83

For odd n, we define $k = \frac{n-3}{2}$ and $S_k^i = 4i$ where i is an index defined as $i = 0, 1, 2, ..., k$, and we find the following for the diagonal components I_{yy} and I_{zz}

$$I_{yy} = \frac{1}{12}(-968 + 717\pi + n(532 - 927\pi + 384n\pi)) + (8 + 8\pi)\sum_{i=0}^{k}(S_k^i)^2 \quad (3.2.49)$$

$$I_{zz} = \frac{1}{12}(-1120 + 819\pi + n(532 - 927\pi + 384n\pi)) + (8 + 8\pi)\sum_{i=0}^{k}(S_k^i)^2 \quad (3.2.50)$$

For even n, we define $m = \frac{n}{2}$, and $T_m^j = 4j - 2$ where j is an index defined as $j = 1, 2, ..., m - 1$, and because of symmetry we find the same value for both I_{yy} and I_{zz}

$$I_{yy} = I_{zz} = -\frac{266}{3} + 64\pi + n\left(\frac{133}{3} - \frac{309\pi}{4} + 32n\pi\right) + (8 + 8\pi)\sum_{j=1}^{m-1}(T_m^j)^2 \quad (3.2.51)$$

3.2.6 Exact Calculation of Moment of Inertia Tensor for a Solid Link with 4 tori

We will now consider two additional chain link configurations. The first inertia tensor we will calculate is for a link shown in Figure 30. The link is composed of three solid tori, and a solid stretched torus which can be broken into three toroidal components and three cylindrical components. We want the moment of inertia tensor about the origin of the coordinate system [38]. For each component of the link, we will need to first calculate the moment of inertia, I_{CM} in its center of mass frame, which is denoted by the x'-, y'-, z'-axes. From the center of mass frame, we will use the the Parallel Axis Theorem as defined in Section 1.1.2, as well as coordinate transformations. We define the coordinate transformation from x'-, y'-, z'-axes to x-,

84
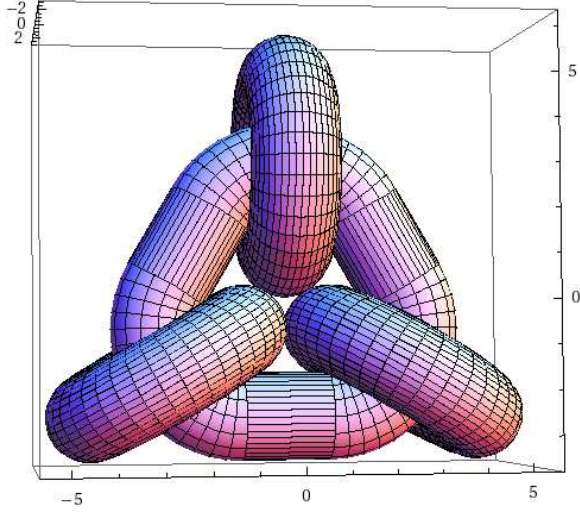
Figure 30: Link with 4 tori (3 tori going through the center of the 4th torus).

y-, z-axes as

$$\mathbf{A} = \begin{pmatrix} a_{xx'} & a_{xy'} & a_{xz'} \\ a_{yx'} & a_{yy'} & a_{yz'} \\ a_{zx'} & a_{zy'} & a_{zz'} \end{pmatrix} \qquad (3.2.52)$$

We first calculate the inertia tensors of the three unstretched tori going through the center of the stretched torus. We start with the inertia tensor of a torus azimuthally symmetric about the z-axis; so the inertia tensor, I_{CM}, relative to its principal axes x', y', z' is given by Equation (3.2.8). The origin of the center of mass system of the right-hand torus is at $(\frac{6+2\sqrt{3}}{3}a,\, 0,\, \frac{-1-\sqrt{3}}{3}a)$, and the angle between the z-axis and the z'-axis is 30°. We first apply Equation (3.2.17) to obtain the inertia tensor about O, relative to axes parallel to x', y', z'. $\mathrm{I}^{torus}_{O(x',y',z')}$ is then the moment of inertia of a torus whose principal axes are parallel to x, y, z. From the geometry, it can be shown

85

that the origin of the primed system is moved by a distance $\frac{6+2\sqrt{3}}{3}a$ in the negative

x'-direction.

$$I^{torus}_{O(x',y',z')} = \begin{pmatrix} \frac{21}{2}a^5 & 0 & 0 \\ 0 & \frac{21}{2}a^5 + 4a^3(\frac{-6-2\sqrt{3}}{3}a)^2 & 0 \\ 0 & 0 & 19a^5 + 4a^3(\frac{-6-2\sqrt{3}}{3}a)^2 \end{pmatrix} \pi^2\rho \quad (3.2.53)$$

or simplified to

$$I^{torus}_{O(x',y',z')} = \begin{pmatrix} \frac{21}{2} & 0 & 0 \\ 0 & \frac{191}{6} + \frac{32}{\sqrt{3}} & 0 \\ 0 & 0 & \frac{121}{3} + \frac{32}{\sqrt{3}} \end{pmatrix} a^5\pi^2\rho \quad (3.2.54)$$

The final step is the transformation from x'-, y'-, z'-axes to the x-, y-, z-axes. We use

an orthogonal transformation, which is defined as

$$I^{torus}_{O(x,y,z)} = \mathbf{A} \cdot I^{torus}_{O(x',y',z')} \cdot \mathbf{A}^t \quad (3.2.55)$$

For the right-hand torus, the transformation is given by

$$\mathbf{A} = \begin{pmatrix} \frac{\sqrt{3}}{2} & 0 & \frac{1}{2} \\ 0 & 1 & 0 \\ -\frac{1}{2} & 0 & \frac{\sqrt{3}}{2} \end{pmatrix} \quad (3.2.56)$$

We can now carry out Equation (3.2.55) in two steps.

$$\mathbf{A} \cdot I^{torus}_{O(x',y',z')} = \begin{pmatrix} \frac{21\sqrt{3}}{4} & 0 & \frac{121}{6} + \frac{16}{\sqrt{3}} \\ 0 & \frac{95}{6} + \frac{32}{\sqrt{3}} & 0 \\ -\frac{21}{4} & 0 & 16 + \frac{121}{2\sqrt{3}} \end{pmatrix} a^5\pi^2\rho \quad (3.2.57)$$

And, finally

$$
\begin{aligned}
I^{torus}_{O(x,y,z)} &= (\mathbf{A} \cdot I^{torus}_{O(x',y',z')}) \cdot \mathbf{A}^t = \\
&= \begin{pmatrix}
\frac{431}{24} + \frac{8}{\sqrt{3}} & 0 & 8 + \frac{179}{8\sqrt{3}} \\
0 & \frac{191}{6} + \frac{32}{\sqrt{3}} & 0 \\
8 + \frac{179}{8\sqrt{3}} & 0 & \frac{263}{8} + 8\sqrt{3}
\end{pmatrix} a^5 \pi^2 \rho
\end{aligned}
\qquad (3.2.58)
$$

We follow the same steps to calculate the inertia tensor for the left-hand torus. The origin of the center of mass system of the left-hand torus is at $(\frac{-6-2\sqrt{3}}{3}a,\, 0,\, \frac{-1-\sqrt{3}}{3}a)$, and the angle between the z-axis and the z'-axis is $150°$. The transformation from x'-, y'-, z'-axes to the x-, y-, z-axes is given by

$$
\mathbf{A} = \begin{pmatrix}
-\frac{\sqrt{3}}{2} & 0 & \frac{1}{2} \\
0 & 1 & 0 \\
-\frac{1}{2} & 0 & -\frac{\sqrt{3}}{2}
\end{pmatrix}
\qquad (3.2.59)
$$

And, its corresponding inertia tensor is

$$
I^{torus}_{O(x,y,z)} = \begin{pmatrix}
\frac{431}{24} + \frac{8}{\sqrt{3}} & 0 & -8 - \frac{179}{8\sqrt{3}} \\
0 & \frac{191}{6} + \frac{32}{\sqrt{3}} & 0 \\
-8 - \frac{179}{8\sqrt{3}} & 0 & \frac{263}{8} + 8\sqrt{3}
\end{pmatrix} a^5 \pi^2 \rho
\qquad (3.2.60)
$$

For the top torus the origin of the center of mass system is at $(0,\, 0,\, \frac{-6-2\sqrt{3}}{3}a)$, and the angle between the z-axis and the z'-axis is $270°$. The transformation from x'-, y'-, z'-axes to the x-, y-, z-axes is given by

$$
\mathbf{A} = \begin{pmatrix}
0 & 0 & -1 \\
0 & 1 & 0 \\
1 & 0 & 0
\end{pmatrix}
\qquad (3.2.61)
$$

87

And, the final inertia tensor for this torus is

$$
I_{O(x,y,z)}^{torus} = \begin{pmatrix} \frac{121}{3} + \frac{32}{\sqrt{3}} & 0 & 0 \\ 0 & \frac{191}{6} + \frac{32}{\sqrt{3}} & 0 \\ 0 & 0 & \frac{21}{2} \end{pmatrix} a^5 \pi^2 \rho \tag{3.2.62}
$$

The inertia tensors of the three tori may be added and we obtain

$$
I_{O}^{3tori} = \begin{pmatrix} \frac{305}{4} + 16\sqrt{3} & 0 & 0 \\ 0 & \frac{191}{2} + \frac{32}{\sqrt{3}} & 0 \\ 0 & 0 & \frac{305}{4} + 16\sqrt{3} \end{pmatrix} a^5 \pi^2 \rho \tag{3.2.63}
$$

Lastly, we look at the stretched torus component which we break it up into cylindrical parts and toroidal parts. We begin with the inertia tensor of a cylinder described by the following parametric equations

$$
\begin{aligned}
x &= r\cos\theta \\
y &= r\sin\theta \\
z &= z
\end{aligned} \tag{3.2.64}
$$

where θ goes from 0 to 2π, z goes from $-a$ to a and r goes from 0 to a. Which gives an inertia tensor for the cylinder in its center of mass frame of

$$
I_{CM}^{cyl} = \begin{pmatrix} \frac{7}{6} & 0 & 0 \\ 0 & \frac{7}{6} & 0 \\ 0 & 0 & 1 \end{pmatrix} a^5 \pi \rho \tag{3.2.65}
$$

For the bottom cylinder, the origin of the center of mass system is at $(0, 0, \frac{-\sqrt{3}}{3}a - 2a)$, and the angle between the z-axis and the z'-axis is $90°$. We need to move the

88

coordinate system by $\frac{\sqrt{3}}{3}a + 2a$ in the -x′-direction to obtain its inertia tensor relative to the origin at O.

$$I^{cyl}_{O(x',y',z')} = \begin{pmatrix} \frac{7}{6} & 0 & 0 \\ 0 & \frac{11}{2} + \frac{4}{\sqrt{3}} & 0 \\ 0 & 0 & \frac{4}{3}(4 + \sqrt{3}) \end{pmatrix} a^5 \pi \rho \qquad (3.2.66)$$

The transformation from x'-, y'-, z'-axes to x-, y-, z-axes is given by

$$\mathbf{A} = \begin{pmatrix} 0 & 0 & 1 \\ 0 & 1 & 0 \\ -1 & 0 & 0 \end{pmatrix} \qquad (3.2.67)$$

And the final result is

$$I^{cyl}_{O(x,y,z)} = \begin{pmatrix} \frac{4}{3}(4 + \sqrt{3}) & 0 & 0 \\ 0 & \frac{11}{2} + \frac{4}{\sqrt{3}} & 0 \\ 0 & 0 & \frac{7}{6} \end{pmatrix} a^5 \pi \rho \qquad (3.2.68)$$

For the right-hand cylinder, the origin of the center of mass system is at $(\frac{\sqrt{3}}{3}a + 2a,\ 0,\ \frac{\sqrt{3}}{6}a + a)$, and the angle between the z-axis and the z'-axis is $330°$. The transformation from x'-, y'-, z'-axes to x-, y-, z-axes is

$$\mathbf{A} = \begin{pmatrix} \frac{\sqrt{3}}{2} & 0 & -\frac{1}{2} \\ 0 & 1 & 0 \\ \frac{1}{2} & 0 & \frac{\sqrt{3}}{2} \end{pmatrix} \qquad (3.2.69)$$

And, the result is

$$I^{cyl}_{O(x,y,z)} = \begin{pmatrix} \frac{53}{24} + \frac{1}{3\sqrt{3}} & 0 & -1 - \frac{25}{48\sqrt{3}} \\ 0 & \frac{11}{2} + 4\sqrt{3} & 0 \\ -1 - \frac{25}{48\sqrt{3}} & 0 & \frac{103}{24} + \sqrt{3} \end{pmatrix} a^5 \pi \rho \qquad (3.2.70)$$

89

For the left-hand cylinder, the origin of the center of mass system is at $(\frac{-\sqrt{3}}{3}a - 2a, 0, \frac{\sqrt{3}}{6}a + a)$, and the angle between the z-axis and the z'-axis is $30°$. The transformation is given by Equation (3.2.56), and the inertia tensor is

$$I^{cyl}_{O(x,y,z)} = \begin{pmatrix} \frac{53}{24} + \frac{1}{3\sqrt{3}} & 0 & 1 + \frac{25}{48\sqrt{3}} \\ 0 & \frac{11}{2} + 4\sqrt{3} & 0 \\ 1 + \frac{25}{48\sqrt{3}} & 0 & \frac{103}{24} + \sqrt{3} \end{pmatrix} a^5 \pi \rho \qquad (3.2.71)$$

The inertia tensors of the three cylindrical components may be added and we obtain

$$I^{cyl}_{O} = \begin{pmatrix} \frac{39}{4} + 2\sqrt{3} & 0 & 0 \\ 0 & \frac{33}{2} + \frac{4}{\sqrt{3}} & 0 \\ 0 & 0 & \frac{39}{4} + 2\sqrt{3} \end{pmatrix} a^5 \pi \rho \qquad (3.2.72)$$

For the right-hand $\frac{1}{3}$-torus, the origin of the center of mass system is at $(\frac{2\sqrt{3}a}{3}, 0, \frac{-\sqrt{3}a}{3})$, and the angle between the z-axis and the z'-axis is $30°$. We need to move the coordinate system by $\frac{\sqrt{3}}{3}a + 2a$ in the -x'-direction to obtain its inertia tensor relative to the origin at O. Lastly, we need the toroidal components of the stretched torus azimuthally symmetric about the y-axis. First we need to find the center of mass of a third of a torus, again using Equation (3.2.32). For a third of a torus that is symmetric about the x-axis the center of mass is $(-\frac{51\sqrt{3}a}{16\pi}, 0, 0)$ and its inertia tensor is

$$I^{\frac{1}{3}torus}_{CM} = \begin{pmatrix} A & 0 & 0 \\ 0 & C & 0 \\ 0 & 0 & D \end{pmatrix} a^5 \rho \qquad (3.2.73)$$

where $A = \frac{1}{8}\pi(-19\sqrt{3} + 28\pi)$, $C = \frac{-2601}{64} + \frac{19\pi^2}{3}$ and $D = \frac{1}{64}(-2601 + 152\sqrt{3}\pi + 224\pi^2)$.

For the right-hand $\frac{1}{3}$-torus, the origin of the center of mass system is at $(\frac{2\sqrt{3}a}{3}, 0, \frac{-\sqrt{3}a}{3})$,

and the angle between the z-axis and the z'-axis is $30°$. To find the inertia tensor about O, relative to axes parallel to x', y', z', we first apply (3.2.17) to move the origin of the center of mass system of the torus from $(-\frac{51\sqrt{3}a}{16\pi},0,0)$ to $(\frac{2\sqrt{3}a}{3},0,0)$. This results in

$$I_{O(x',y',z')}^{\frac{1}{3}torus} = \begin{pmatrix} A & 0 & 0 \\ 0 & C & 0 \\ 0 & 0 & D \end{pmatrix} a^5\pi\rho \tag{3.2.74}$$

where $A = \frac{1}{8}(-19\sqrt{3}+28\pi)$, $C = \frac{1}{9}(153+73\pi)$ and $D = \frac{1}{72}(1224+171\sqrt{3}+380\pi)$. The transformation from x'-, y'-, z'-axes to x-, y-, z-axes is given by (3.2.56). Carrying out the transformation yields

$$I_{O(xyz)}^{\frac{1}{3}torus} = \begin{pmatrix} A & 0 & B \\ 0 & C & 0 \\ B & 0 & D \end{pmatrix} a^5\pi\rho \tag{3.2.75}$$

where $A = \frac{1}{144}(612-171\sqrt{3}+568\pi)$, $B = \frac{1}{144}(513+612\sqrt{3}+64\sqrt{3}\pi)$, $C = \frac{1}{9}(153+73\pi)$ and $D = \frac{1}{48}(612+57\sqrt{3}+232\pi)$. For the left-hand $\frac{1}{3}$-torus, the origin of the center of mass system is at $(\frac{-2\sqrt{3}a}{3}, 0, \frac{-\sqrt{3}a}{3})$, and the angle between the z-axis and the z'-axis is $150°$. Similarly, for the left-hand $\frac{1}{3}$-torus we find

$$I_{O(xyz)}^{\frac{1}{3}torus} = \begin{pmatrix} A & 0 & B \\ 0 & C & 0 \\ B & 0 & D \end{pmatrix} a^5\pi\rho \tag{3.2.76}$$

where $A = \frac{1}{144}(612-171\sqrt{3}+568\pi)$, $B = -\frac{1}{144}(513+612\sqrt{3}+64\sqrt{3}\pi)$, $C = \frac{1}{9}(153+73\pi)$ and $D = \frac{1}{48}(612+57\sqrt{3}+232\pi)$. For the left-hand $\frac{1}{3}$-torus, the origin of the

91

center of mass system is at $(0, 0, \frac{2\sqrt{3}a}{3})$, and the angle between the z-axis and the

z'-axis is $90°$. For the top $\frac{1}{3}$-torus we calculate

$$I_{O(x',y',z')}^{\frac{1}{3}torus} = \begin{pmatrix} A & 0 & 0 \\ 0 & C & 0 \\ 0 & 0 & D \end{pmatrix} a^5 \pi \rho \qquad (3.2.77)$$

where $A = \frac{1}{72}(1224 + 171\sqrt{3} + 380\pi)$, $C = \frac{1}{9}(153 + 73\pi)$ and $D = \frac{1}{8}(-19\sqrt{3} + 28\pi)$.

The inertia tensors of the fractional toroidal components may be added to give

$$I_O^{\frac{1}{3}torus} = \begin{pmatrix} \frac{1}{6}(153 + 79\pi) & 0 & 0 \\ 0 & \frac{1}{3}(153 + 73\pi) & 0 \\ 0 & 0 & \frac{1}{6}(153 + 79\pi) \end{pmatrix} a^5 \pi \rho \qquad (3.2.78)$$

Finally, we sum all of the inertia tensor components to determine the inertia tensor

of the link, $I_O^{link} = I_O^{\frac{1}{3}torus} + I_O^{cyl} + I_O^{torus}$, and we find

$$I_O^{link} = \begin{pmatrix} \frac{1}{12}(A + B\pi) & 0 & 0 \\ 0 & \frac{1}{6}(C + D\pi) & 0 \\ 0 & 0 & \frac{1}{12}(A + B\pi) \end{pmatrix} a^5 \pi \rho \qquad (3.2.79)$$

where $A = 423 + 24\sqrt{3}$, $B = 1073 + 192\sqrt{3}$, $C = 405 + 8\sqrt{3}$ and $D = 719 + 192\sqrt{3}$.

3.2.7   Exact Calculation of Moment of Inertia Tensor for a Solid Link with 5 tori

The next link we will examine has 4 tori going through one stretched torus, and

is shown in Figure 31. Following the previous calculation, we begin with the I_{CM}^{torus}

as defined in Equation (3.2.8). For this geometry, the origin of the primed system is
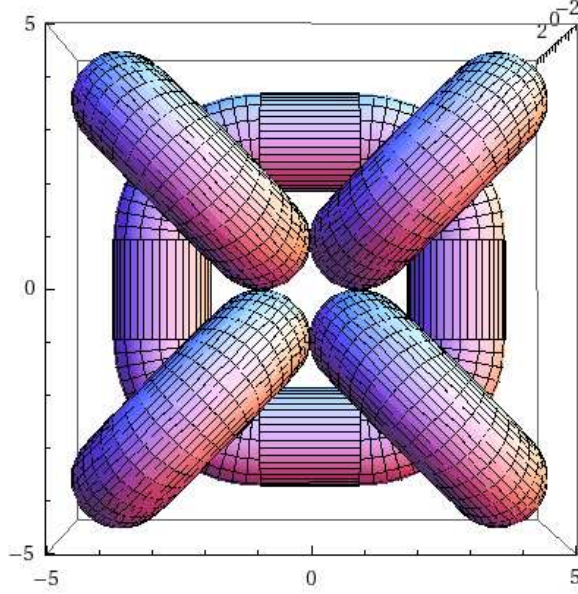
Figure 31: Link with 5 tori (4 tori going through the center of the 5th torus).

moved by a distance $\sqrt{2}a + 2a$ in the negative x'-direction; this is true for all four tori passing through the center of the stretched torus. Applying (3.2.17), we find

$$
I^{torus}_{O(x',y',z')} = \begin{pmatrix} \frac{21}{2} & 0 & 0 \\ 0 & \frac{69}{2} + 16\sqrt{2} & 0 \\ 0 & 0 & 43 + 16\sqrt{2} \end{pmatrix} a^5\pi^2\rho \qquad (3.2.80)
$$

The next step is to transform the system from x'-, y'-, z'-axes to x-, y-, z-axes. We choose the right-hand top torus first, the transformation is given by

$$
\mathbf{A} = \begin{pmatrix} \frac{\sqrt{2}}{2} & 0 & -\frac{\sqrt{2}}{2} \\ 0 & 1 & 0 \\ \frac{\sqrt{2}}{2} & 0 & \frac{\sqrt{2}}{2} \end{pmatrix} \qquad (3.2.81)
$$

93

Applying (3.2.55), we obtain

$$I_{O(x,y,z)}^{torus} = (\mathbf{A} \cdot I_{O(x',y',z')}^{torus}) \cdot \mathbf{A}^t =$$

$$= \begin{pmatrix} \frac{107}{4} + 8\sqrt{2} & 0 & -\frac{65}{4} - 8\sqrt{2} \\ 0 & \frac{69}{2} + 16\sqrt{2} & 0 \\ -\frac{65}{4} - 8\sqrt{2} & 0 & \frac{107}{4} + 8\sqrt{2} \end{pmatrix} a^5 \pi^2 \rho \qquad (3.2.82)$$

The transformation for the bottom right-hand torus from x'-, y'-, z'-axes to x-, y-,

z-axes is given by

$$\mathbf{A} = \begin{pmatrix} \frac{\sqrt{2}}{2} & 0 & \frac{\sqrt{2}}{2} \\ 0 & 1 & 0 \\ -\frac{\sqrt{2}}{2} & 0 & \frac{\sqrt{2}}{2} \end{pmatrix} \qquad (3.2.83)$$

Applying (3.2.55), for the bottom right-hand torus we obtain

$$I_{O(x,y,z)}^{torus} = (\mathbf{A} \cdot I_{O(x',y',z')}^{torus}) \cdot \mathbf{A}^t =$$

$$= \begin{pmatrix} \frac{107}{4} + 8\sqrt{2} & 0 & \frac{65}{4} + 8\sqrt{2} \\ 0 & \frac{69}{2} + 16\sqrt{2} & 0 \\ \frac{65}{4} + 8\sqrt{2} & 0 & \frac{107}{4} + 8\sqrt{2} \end{pmatrix} a^5 \pi^2 \rho \qquad (3.2.84)$$

The transformation for the bottom left-hand torus from x'-, y'-, z'-axes to x-, y-,

z-axes is given by

$$\mathbf{A} = \begin{pmatrix} -\frac{\sqrt{2}}{2} & 0 & \frac{\sqrt{2}}{2} \\ 0 & 1 & 0 \\ -\frac{\sqrt{2}}{2} & 0 & -\frac{\sqrt{2}}{2} \end{pmatrix} \qquad (3.2.85)$$

Applying Equation (3.2.17), for the bottom left-hand torus we obtain

$$I_{O(x,y,z)}^{torus} = (\mathbf{A} \cdot_{O(x',y',z')}^{torus}) \cdot \mathbf{A}^t =$$

94

$$
= \begin{pmatrix} \frac{107}{4} + 8\sqrt{2} & 0 & -\frac{65}{4} - 8\sqrt{2} \\ 0 & \frac{69}{2} + 16\sqrt{2} & 0 \\ -\frac{65}{4} - 8\sqrt{2} & 0 & \frac{107}{4} + 8\sqrt{2} \end{pmatrix} a^5 \pi^2 \rho \qquad (3.2.86)
$$

The transformation for the top left-hand torus from x', y', z'-axes to x, y, z-axes is given by

$$
\mathbf{A} = \begin{pmatrix} -\frac{\sqrt{2}}{2} & 0 & -\frac{\sqrt{2}}{2} \\ 0 & 1 & 0 \\ \frac{\sqrt{2}}{2} & 0 & -\frac{\sqrt{2}}{2} \end{pmatrix} \qquad (3.2.87)
$$

Applying (3.2.17), for the top left-hand torus we obtain

$$
\begin{aligned}
I^{torus}_{O(x,y,z)} &= (\mathbf{A} \cdot I^{torus}_{O(x',y',z')}) \cdot \mathbf{A}^t = \\
&= \begin{pmatrix} \frac{107}{4} + 8\sqrt{2} & 0 & \frac{65}{4} + 8\sqrt{2} \\ 0 & \frac{69}{2} + 16\sqrt{2} & 0 \\ \frac{65}{4} + 8\sqrt{2} & 0 & \frac{107}{4} + 8\sqrt{2} \end{pmatrix} a^5 \pi^2 \rho \qquad (3.2.88)
\end{aligned}
$$

The inertia tensor of the four fractional tori may be added and we obtain

$$
I^{torus}_O = \begin{pmatrix} 107 + 32\sqrt{2} & 0 & 0 \\ 0 & 138 + 64\sqrt{2} & 0 \\ 0 & 0 & 107 + 32\sqrt{2} \end{pmatrix} a^5 \pi^2 \rho \qquad (3.2.89)
$$

Now, we turn our attention to the stretched torus. We first look at the cylindrical parts. The inertia tensor of the single cylinder about its center, relative to its principal axes x', y', z', is given by Equation (3.2.65).

For the right-hand cylinder, we only need to move the x', y', z' coordinate system by $3a$ in the negative x′-direction to obtain the inertia tensor relative to the origin at

O.

$$I^{cyl}_{O(xyz)} = \begin{pmatrix} \frac{7}{6} & 0 & 0 \\ 0 & \frac{115}{6} & 0 \\ 0 & 0 & 19 \end{pmatrix} a^5 \pi \rho \tag{3.2.90}$$

We obtain the same result for the left-hand cylinder.

For the top and bottom cylinders, we need to take the above result and rotate it by $90°$ which is described by the transformation in Equation (3.2.67). For the top and bottom cylinder, we find an inertia tensor of

$$I^{cyl}_{O(xyz)} = \begin{pmatrix} 19 & 0 & 0 \\ 0 & \frac{115}{6} & 0 \\ 0 & 0 & \frac{7}{6} \end{pmatrix} a^5 \pi \rho \tag{3.2.91}$$

The inertia tensors of the four cylindrical components can be added and we find

$$I^{cyl}_{O} = \begin{pmatrix} \frac{121}{3} & 0 & 0 \\ 0 & \frac{230}{3} & 0 \\ 0 & 0 & \frac{121}{3} \end{pmatrix} a^5 \pi \rho \tag{3.2.92}$$

The last parts we need are the toroidal components of the stretched torus. We begin with a quarter of a torus. We need to find the center of mass for a quarter of a torus; for a quarter of a torus that is symmetric about the x-axis the center of mass is ($-\frac{17a}{2\sqrt{2}\pi}$,0,0). The inertia tensor for a quarter torus, relative to its principal axes x', y', z', in its center of mass is

$$I^{\frac{1}{4}torus}_{CM} = \rho \int_0^{2\pi} \int_{-\frac{\pi}{4}}^{\frac{\pi}{4}} \int_0^a \mathbf{Q}[r(2a + r\cos\nu)]dr\,du\,d\nu \tag{3.2.93}$$

96

or

$$I_{CM}^{\frac{1}{4}torus} = \begin{pmatrix} A & 0 & 0 \\ 0 & C & 0 \\ 0 & 0 & D \end{pmatrix} a^5\rho \qquad (3.2.94)$$

where $A = \frac{1}{8}\pi(-38 + 21\pi)$, $C = \frac{1}{8}(-289 + 38\pi^2)$ and $D = \frac{1}{8}(-289 + 38\pi + 21\pi^2)$.

We then follow the same steps as outlined for the four full tori above. Each quarter-torus is shifted from $(-\frac{17a}{2\sqrt{2\pi}},0,0)$ to $(\sqrt{2}a,0,0)$ and the transformations are given by Equations (3.2.81), (3.2.83), (3.2.85) and (3.2.87). We will summarize the results.

For the bottom right-hand quarter-torus and the top left-hand torus, we find

$$I_{O}^{\frac{1}{4}torus} = \begin{pmatrix} \frac{1}{8}(68 + 29\pi) & 0 & \frac{1}{4}(53 + 4\pi) \\ 0 & \frac{1}{4}(68 + 27\pi) & 0 \\ \frac{1}{4}(53 + 4\pi) & 0 & \frac{1}{8}(68 + 29\pi) \end{pmatrix} a^5\pi\rho \qquad (3.2.95)$$

For the top right-hand quarter torus and the bottom left-hand torus, we find

$$I_{O}^{\frac{1}{4}torus} = \begin{pmatrix} \frac{1}{8}(68 + 29\pi) & 0 & -\frac{1}{4}(53 + 4\pi) \\ 0 & \frac{1}{4}(68 + 27\pi) & 0 \\ -\frac{1}{4}(53 + 4\pi) & 0 & \frac{1}{8}(68 + 29\pi) \end{pmatrix} a^5\pi\rho \qquad (3.2.96)$$

Adding all four components together, we find the inertia tensor of the four quarter pieces of a torus to be

$$I_{O}^{\frac{1}{4}torus} = \begin{pmatrix} \frac{1}{2}(68 + 29\pi) & 0 & 0 \\ 0 & \frac{1}{2}(68 + 27\pi) & 0 \\ 0 & 0 & \frac{1}{2}(68 + 29\pi) \end{pmatrix} a^5\pi\rho \qquad (3.2.97)$$

97

We can now add all of the inertia tensor components together to determine the inertia tensor of the link, $I_O^{link} = I_O^{\frac{1}{4}tensor} + I_O^{cyl} + I_O^{torus}$:

$$I_O^{link} = \begin{pmatrix} A & 0 & 0 \\ 0 & C & 0 \\ 0 & 0 & D \end{pmatrix} a^5 \pi \rho \tag{3.2.98}$$

where $A = \frac{1}{6}(446 + 3(243 + 64\sqrt{2})\pi)$, $C = \frac{1}{3}(434 + 3(165 + 64\sqrt{2})\pi)$ and $D = \frac{1}{6}(446 + 3(243 + 64\sqrt{2})\pi)$.

3.3 Exact Calculation of Moment of Inertia Tensor for several hollow geometries

In addition to calculating the moment of inertia tensor of a solid link, we can imagine the links composed of hollow tubes. This would be applicable, for example, when considering nanotubes.

3.3.1 Inertia Tensor for a Hollow Torus

We again begin with our primary chain link component, the torus. In this case we treat the torus, as well as subsequent parts of more complicated geometries, as an infinitely thin shell. We will go through the calculation for the moment of inertia tensor of an infinitely thin toroidal shell using two different methods: a surface integral and a volume integral, and we will show that both produce the same result.

We first go through the calculation by redefining the moment of inertia tensor as a surface integral, which is given by the following

$$I = \int_S \sigma(x, y, z) \mathbf{Q} dS \tag{3.3.1}$$

98

where σ is the surface density which is defined as $\sigma = \frac{M}{A}$, A being the surface area of the object. And $\mathbf{Q}$ is as defined in Equation (3.2.5).

The parametric equations for the torus defined in Equation (3.2.6) reduce to the following

$$
\begin{aligned}
x &= (c + a\cos\nu)\cos u \\
y &= (c + a\cos\nu)\sin u \\
z &= r\sin\nu
\end{aligned}
\tag{3.3.2}
$$

Using the parametric equations, we calculate the inertia tensor to be

$$
Iz^{torus} = \sigma \int_0^{2\pi} \int_0^{2\pi} \mathbf{Q}a^2(2 + \cos\nu)du d\nu
\tag{3.3.3}
$$

or

$$
Iz^{torus} = \begin{pmatrix} 26 & 0 & 0 \\ 0 & 26 & 0 \\ 0 & 0 & 44 \end{pmatrix} a^4\pi^2\sigma
\tag{3.3.4}
$$

The second method for calculating the inertia tensor of a hollow torus follows Equations (3.2.4) - (3.2.6), and redefines the limits in Equation (3.2.7) to be the following

$$
Iz^{torus} = \rho \int_0^{2\pi} \int_0^{2\pi} \int_a^{a+\epsilon} \mathbf{Q}r(2a + r\cos\nu)dr du d\nu
\tag{3.3.5}
$$

Calculating the integrals gives the following inertia tensor

$$
Iz^{torus} = \begin{pmatrix} A & 0 & 0 \\ 0 & C & 0 \\ 0 & 0 & D \end{pmatrix} a(2a + \epsilon)\pi^2\epsilon\rho
\tag{3.3.6}
$$

99

where $A = \frac{1}{2}(26a^2 + 10a\epsilon + 5\epsilon^2)$, $C = \frac{1}{2}(26a^2 + 10a\epsilon + 5\epsilon^2)$ snd $D = (22a^2 + 6a\epsilon + 3\epsilon^2)$.

The thin shell has a surface density, not a volume density; the surface density is $\sigma = \epsilon\rho$. Since we want an infinitely thin shell, we take the limit as $\epsilon \to 0$. Replacing the volume density by a surface density and taking the limit produces the same result as Equation (3.3.4).

3.3.2   Inertia Tensor of a Hollow Hopf link

The process of calculating the inertia tensor of a hollow Hopf link is the same as for a solid Hopf link. We will list the final result only

$$
I^{hopf} = \begin{pmatrix} 52 & 0 & 0 \\ 0 & 86 & 0 \\ 0 & 0 & 86 \end{pmatrix} a^4 \pi^2 \sigma \tag{3.3.7}
$$

3.3.3   Inertia Tensor for a Hollow Chain of 3, 4, 5, and 6 Links

We will follow the same process as for the inertia tensor for a solid chain link. First we will calculate the stretched torus, then we will add the components together sometimes after necessary rotations or translations. Since the details have been worked out previously, we will simply list the results.

$$
Iz_O^{stretched} = \begin{pmatrix} 2(20 + 13\pi) & 0 & 0 \\ 0 & \frac{2}{3}(118 + 51\pi) & 0 \\ 0 & 0 & \frac{4}{3}(83 + 39\pi) \end{pmatrix} a^4 \pi \sigma \tag{3.3.8}
$$

100

3.3.4 Hollow Link $2_1^2 \# 2_1^2$

The result for the link $2_1^2 \# 2_1^2$ composed of components that are thin shells is

$$
I_O^{2_1^2 \# 2_1^2} = \begin{pmatrix} 2(20 + 39\pi) & 0 & 0 \\ 0 & \frac{4}{3}(83 + 186\pi) & 0 \\ 0 & 0 & \frac{2}{3}(118 + 399\pi) \end{pmatrix} a^4 \pi \sigma \qquad (3.3.9)
$$

3.3.5 Hollow Chain Link with 4 components

The result for a chain link with four components composed of thin shells is

$$
I_O^{4-link} = \begin{pmatrix} 8(10 + 13\pi) & 0 & 0 \\ 0 & \frac{760}{3} + 620\pi & 0 \\ 0 & 0 & \frac{760}{3} + 620\pi \end{pmatrix} a^4 \pi \sigma \qquad (3.3.10)
$$

3.3.6 Hollow Chain link with 5 components

The result for a chain link with five components composed of thin shells is

$$
I_O^{5-link} = \begin{pmatrix} 120 + 130\pi & 0 & 0 \\ 0 & 556 + 1230\pi & 0 \\ 0 & 0 & 524 + 1248\pi \end{pmatrix} a^4 \pi \sigma \qquad (3.3.11)
$$

3.3.7 Hollow Chain link with 6 components

The result for a chain link with five components composed of thin shells is

$$
I_O^{6-link} = \begin{pmatrix} 4(40 + 39\pi) & 0 & 0 \\ 0 & \frac{3056}{3} + 2178\pi & 0 \\ 0 & 0 & \frac{3056}{3} + 2178\pi \end{pmatrix} a^4 \pi \sigma \qquad (3.3.12)
$$

3.3.8 Generalization of Inertia Tensor for a hollow chain of 'n' components

We again note that a chain with an even number of components yields a symmetric top, whereas a chain with an odd number of components produces an asymmetric top. We will generalize the relationship for the inertia tensor of a chain with 'n' components, and we note that it follows the same form as for a solid chain but with different coefficients.

$$I_O^{n-link} = \begin{pmatrix} I_{xx} & 0 & 0 \\ 0 & I_{yy} & 0 \\ 0 & 0 & I_{zz} \end{pmatrix} a^4 \pi \sigma \tag{3.3.13}$$

For both even and odd n, the I_{xx} component can be generalized as

$$I_{xx} = -80 + n(40 + 26\pi) \tag{3.3.14}$$

For odd n, we define $k = \frac{n-3}{2}$ and $S_k^i = 4i$ where i is an index defined as $i = 0, 1, 2, ..., k$, and we find the following for the diagonal components I_{yy} and I_{zz}

$$I_{yy} = -\frac{319}{3} + 83\pi + n\left(\frac{217}{3} - 137\pi + 64n\pi\right) + 2(8 + 8\pi)\sum_{i=0}^{k}(S_k^i)^2 \tag{3.3.15}$$

$$I_{zz} = 9(-13 + 15\pi) + n\left(\frac{185}{3} - 137\pi + 64n\pi\right) + 2(8 + 8\pi)\sum_{i=0}^{k}(S_k^i)^2 \tag{3.3.16}$$

For even n, we define $m = \frac{n}{2}$, and $T_m^j = 4j - 2$ where j is an index defined as $j = 1, 2, ..., m - 1$, and because of symmetry we find the same value for both I_{yy} and I_{zz}

$$I_{yy} = I_{zz} = -\frac{568}{3} + \frac{n}{2} + 64(-2 + n)(-1 + n)\pi + 2(8 + 8\pi)\sum_{j=1}^{m-1}(T_m^j)^2 \tag{3.3.17}$$

3.3.9 Exact Calculation of Inertia Tensor for a Hollow Link with 4 tori

We will go through the sames steps for the thin shell calculation of the inertia tensor of 4 tori, where three go through the center of the fourth. We again start with the inertia tensor of a torus azimuthally symmetric about the z-axis, which is given by

$$Iy^{torus} = \begin{pmatrix} 26 & 0 & 0 \\ 0 & 44 & 0 \\ 0 & 0 & 26 \end{pmatrix} a^4\pi^2\sigma \tag{3.3.18}$$

For the right-hand torus, we need to move the torus by a distance of $\frac{6+2\sqrt{3}}{3}a$ in the positive x'-direction.

$$I_{O(x',y',z')}^{torus} = \begin{pmatrix} 26a^4 & 0 & 0 \\ 0 & 44a^4 + 8a^2(\frac{6+2\sqrt{3}}{3}a)^2 & 0 \\ 0 & 0 & 26a^5 + 8a^2(\frac{6+2\sqrt{3}}{3}a)^2 \end{pmatrix} \pi^2\sigma \tag{3.3.19}$$

or simplified to

$$I_{O(x',y',z')}^{torus} = \begin{pmatrix} 26 & 0 & 0 \\ 0 & \frac{4}{3}(65 + 16\sqrt{3}) & 0 \\ 0 & 0 & \frac{2}{3}(103 + 32\sqrt{3}) \end{pmatrix} a^4\pi^2\sigma \tag{3.3.20}$$

And lastly, we need to transform the system from x'-, y'-, z'-axes to the x-, y-, z-axes, using the transformation defined in Equations (3.2.55) - (3.2.56). The result is

$$I_{O(x,y,z)}^{torus} = (\mathbf{A} \cdot I_{O(x',y',z')}^{torus}) \cdot \mathbf{A}^t =$$

$$
= \begin{pmatrix} \frac{2}{3}(55 + 8\sqrt{3}) & 0 & \frac{16}{3}(3 + 2\sqrt{3}) \\ 0 & \frac{4}{3}(65 + 16\sqrt{3}) & 0 \\ \frac{16}{3}(3 + 2\sqrt{3}) & 0 & 2(29 + 8\sqrt{3}) \end{pmatrix} a^4\pi^2\sigma \quad (3.3.21)
$$

The inertia tensor of the left-hand torus is calculated to be

$$
I^{torus}_{O(x,y,z)} = \begin{pmatrix} \frac{2}{3}(55 + 8\sqrt{3}) & 0 & -\frac{16}{3}(3 + 2\sqrt{3}) \\ 0 & \frac{4}{3}(65 + 16\sqrt{3}) & 0 \\ -\frac{16}{3}(3 + 2\sqrt{3}) & 0 & 2(29 + 8\sqrt{3}) \end{pmatrix} a^4\pi^2\sigma \quad (3.3.22)
$$

The inertia tensor of top torus is given by

$$
I^{torus}_{O(x,y,z)} = \begin{pmatrix} \frac{2}{3}(103 + 32\sqrt{3}) & 0 & 0 \\ 0 & \frac{4}{3}(65 + 16\sqrt{3}) & 0 \\ 0 & 0 & 26 \end{pmatrix} a^4\pi^2\sigma \quad (3.3.23)
$$

The inertia tensors of the three tori may be added and we obtain

$$
I^{torus}_{O(x,y,z)} = \begin{pmatrix} 2(71 + 16\sqrt{3}) & 0 & 0 \\ 0 & 4(65 + 16\sqrt{3}) & 0 \\ 0 & 0 & 2(71 + 16\sqrt{3}) \end{pmatrix} a^4\pi^2\sigma \quad (3.3.24)
$$

Next, we look at the fourth component of the link which is a stretched torus. As in the previous section, we break it up into cylindrical parts and toroidal parts. We can write the inertia tensor of the single cylinder about its center, relative to its principal axes x', y', z' as

$$
I^{cyl}_{CM} = \begin{pmatrix} \frac{10}{3} & 0 & 0 \\ 0 & \frac{10}{3} & 0 \\ 0 & 0 & 4 \end{pmatrix} a^4\pi\sigma \quad (3.3.25)
$$

104

For the bottom cylinder, we first need to move the coordinate system by $\frac{\sqrt{3}}{3}a + 2a$ in the x'-direction to obtain its inertia tensor relative to the origin at O:

$$I^{cyl}_{O(x',y',z')} = \begin{pmatrix} \frac{10}{3} & 0 & 0 \\ 0 & \frac{2}{3}(31 + 8\sqrt{3}) & 0 \\ 0 & 0 & \frac{16}{3}(4 + \sqrt{3}) \end{pmatrix} a^4 \pi \sigma \qquad (3.3.26)$$

The transformation from x'-, y'-, z'-axes to x, y, z-axes is given by Equation (3.2.61). The result of the transformation is

$$I^{cyl}_{O(x,y,z)} = \begin{pmatrix} \frac{16}{3}(4 + \sqrt{3}) & 0 & 0 \\ 0 & \frac{2}{3}(31 + 8\sqrt{3}) & 0 \\ 0 & 0 & \frac{10}{3} \end{pmatrix} a^4 \pi \sigma \qquad (3.3.27)$$

The result for right-hand cylinder is

$$I^{cyl}_{O(x,y,z)} = \begin{pmatrix} \frac{1}{6}(47 + 8\sqrt{3}) & 0 & -\frac{1}{2}(8 + 9\sqrt{3}) \\ 0 & \frac{2}{3}(31 + 8\sqrt{3}) & 0 \\ -\frac{1}{2}(8 + 9\sqrt{3}) & 0 & \frac{1}{6}(101 + 24\sqrt{3}) \end{pmatrix} a^4 \pi \sigma \qquad (3.3.28)$$

For the left-hand cylinder, we find

$$I^{cyl}_{O(x,y,z)} = \begin{pmatrix} \frac{1}{6}(47 + 8\sqrt{3}) & 0 & \frac{1}{2}(8 + 9\sqrt{3}) \\ 0 & \frac{2}{3}(31 + 8\sqrt{3}) & 0 \\ \frac{1}{2}(8 + 9\sqrt{3}) & 0 & \frac{1}{6}(101 + 24\sqrt{3}) \end{pmatrix} a^4 \pi \sigma \qquad (3.3.29)$$

The inertia tensors of the three cylindrical components are summed giving

$$I^{cyl}_{O(x,y,z)} = \begin{pmatrix} 37 + 8\sqrt{3} & 0 & 0 \\ 0 & 2(31 + 8\sqrt{3}) & 0 \\ 0 & 0 & 37 + 8\sqrt{3} \end{pmatrix} a^4 \pi \sigma \qquad (3.3.30)$$

105

Lastly, we need the toroidal components of the stretched torus. For the right-hand $\frac{1}{3}$-torus, we calculate the inertia tensor at $(\frac{2\sqrt{3}a}{3},0,0)$ to find the inertia tensor about O, relative to axes parallel to x', y', z':

$$I_{O(x',y',z')}^{\frac{1}{3}torus} = \begin{pmatrix} A & 0 & 0 \\ 0 & C & 0 \\ 0 & 0 & D \end{pmatrix} a^4\pi\sigma \tag{3.3.31}$$

where $A = \frac{1}{6}(-33\sqrt{3} + 52\pi)$, $C = \frac{4}{9}(81 + 41\sqrt{3})$ and $D = \frac{1}{18}(648 + 99\sqrt{3} + 220\pi)$.

The transformation from x'-, y'-, z'-axes to x, y, z-axes is given by (3.2.55) - (3.2.56).

Carrying out the transformation yields

$$I_{O(x,y,z)}^{\frac{1}{3}torus} = \begin{pmatrix} A & 0 & B \\ 0 & C & 0 \\ B & 0 & D \end{pmatrix} a^4\pi\sigma \tag{3.3.32}$$

where $A = \frac{1}{36}(324 - 99\sqrt{3} + 344\pi)$, $B = \frac{1}{36}(297 + 324\sqrt{3} + 32\sqrt{3}\pi)$, $C = \frac{4}{9}(81 + 41\sqrt{3})$ and $D = \frac{1}{12}(324 + 33\sqrt{3} + 136\pi)$. Similarly, for the left-hand $\frac{1}{3}$-torus we find

$$I_{O(x,y,z)}^{\frac{1}{3}torus} = \begin{pmatrix} A & 0 & B \\ 0 & C & 0 \\ B & 0 & D \end{pmatrix} a^4\pi\sigma \tag{3.3.33}$$

where $A = \frac{1}{36}(324 - 99\sqrt{3} + 344\pi)$, $B = -\frac{1}{36}(297 + 324\sqrt{3} + 32\sqrt{3}\pi)$, $C = \frac{4}{9}(81 + 41\sqrt{3})$, and $D = \frac{1}{12}(324 + 33\sqrt{3} + 136\pi)$. For the top $\frac{1}{3}$-torus we calculate

$$I_{O(x,y,z)}^{\frac{1}{3}torus} = \begin{pmatrix} A & 0 & 0 \\ 0 & C & 0 \\ 0 & 0 & D \end{pmatrix} a^4\pi\sigma \tag{3.3.34}$$

106

where $A = \frac{1}{18}(648 + 99\sqrt{3} + 220\pi)$, $C = \frac{4}{9}(81 + 41\sqrt{3})$ and $D = \frac{1}{6}(-33\sqrt{3} + 52\pi)$.

The inertia tensors of the fractional toroidal components may be added to give

$$
I_O^{\frac{1}{3}torus} = \begin{pmatrix} \frac{2}{3}(81 + 47\pi) & 0 & 0 \\ 0 & \frac{4}{3}(81 + 41\sqrt{3}) & 0 \\ 0 & 0 & \frac{2}{3}(81 + 47\pi) \end{pmatrix} a^4\pi\sigma \qquad (3.3.35)
$$

We now add all of the inertia tensor components together to determine the inertia

tensor of the link, $I_O^{link} = I_O^{\frac{1}{3}torus} + I_O^{cyl} + I_O^{torus}$, and we find

$$
I_O^{link} = \begin{pmatrix} \frac{1}{3}(G + H\pi) & 0 & 0 \\ 0 & \frac{2}{3}(J + K\pi) & 0 \\ 0 & 0 & \frac{1}{3}(G + H\pi) \end{pmatrix} a^4\pi\sigma \qquad (3.3.36)
$$

where $G = (273 + 24\sqrt{3})$, $H = 520 + 96\sqrt{3}$, $J = 255 + 24\sqrt{3}$ and $D = 472 + 96\sqrt{3}$.

3.3.10   Exact Calculation of Moment of Inertia Tensor for a Hollow Link with 5 tori

The next link we will examine has 4 tori going through one stretched torus, and is shown in Figure 31. For this geometry, the origin of the primed system is moved by a distance $\sqrt{2}a + 2a$ in the positive x'-direction; this is true for all four tori passing through the center of the stretched torus. Applying (3.2.17), we find

$$
I_{O(x',y',z')}^{torus} = \begin{pmatrix} 26 & 0 & 0 \\ 0 & 4(23 + 8\sqrt{2}) & 0 \\ 0 & 0 & 2(37 + 16\sqrt{2}) \end{pmatrix} a^4\pi\sigma \qquad (3.3.37)
$$

The next step is to transform the system from x'-, y'-, z'-axes to x, y, z-axes. We choose the right-hand top torus first, the transformation is given by Equation (3.2.81).

107

Applying (3.2.55), we obtain

$$I^{torus}_{O(x,y,z)} = \begin{pmatrix} 2(26 + 8\sqrt{2}) & 0 & -8(3 + 2\sqrt{2}) \\ 0 & 4(23 + 8\sqrt{2}) & 0 \\ -8(3 + 2\sqrt{2}) & 0 & 2(25 + 8\sqrt{2}) \end{pmatrix} a^4 \pi \sigma \qquad (3.3.38)$$

The transformation for the bottom right-hand torus from x'-, y'-, z'-axes to x, y, z-axes is given by Equation (3.2.83). Applying (3.2.55), for the bottom right-hand torus we obtain

$$I^{torus}_{O(x,y,z)} = \begin{pmatrix} 2(26 + 8\sqrt{2}) & 0 & 8(3 + 2\sqrt{2}) \\ 0 & 4(23 + 8\sqrt{2}) & 0 \\ 8(3 + 2\sqrt{2}) & 0 & 2(25 + 8\sqrt{2}) \end{pmatrix} a^4 \pi \sigma \qquad (3.3.39)$$

The moment of inertia tensor for the top right-hand torus is the same as Equation (3.3.38) and the inertia tensor for the top left-hand torus is the same as Equation (3.3.39).

The inertia tensor of the four fractional tori may now be added to obtain the following

$$I^{torus}_{O} = \begin{pmatrix} 8(26 + 8\sqrt{2}) & 0 & 0 \\ 0 & 16(23 + 8\sqrt{2}) & 0 \\ 0 & 0 & 8(25 + 8\sqrt{2}) \end{pmatrix} a^4 \pi \sigma \qquad (3.3.40)$$

Next, we look at the inertia tensor for a cylinder, given in Equation (3.3.25). We begin with the right-hand cylinder, where we only need to move the x', y', z' coordinate system by $3a$ in the x'-direction to obtain the inertia tensor relative to the origin at

108

O.

$$I^{cyl}_{O(xyz)} = \begin{pmatrix} \frac{10}{3} & 0 & 0 \\ 0 & \frac{118}{3} & 0 \\ 0 & 0 & 40 \end{pmatrix} a^4\pi\sigma \qquad (3.3.41)$$

We obtain the same result for the left-hand cylinder.

For the top and bottom cylinders, we need to take the above result and rotate it by 90°. For both top and bottom cylinders, we find an inertia tensor of

$$I^{cyl}_{O(xyz)} = \begin{pmatrix} 40 & 0 & 0 \\ 0 & \frac{118}{3} & 0 \\ 0 & 0 & \frac{10}{3} \end{pmatrix} a^4\pi\sigma \qquad (3.3.42)$$

The inertia tensors of the four cylindrical components can be added and we find

$$I^{cyl}_{O} = \begin{pmatrix} \frac{260}{3} & 0 & 0 \\ 0 & \frac{472}{3} & 0 \\ 0 & 0 & \frac{260}{3} \end{pmatrix} a^4\pi\sigma \qquad (3.3.43)$$

The last parts we need are the toroidal components of the stretched torus. We follow the steps outlined in Equations (3.2.93) - (3.2.96). Adding all four components together, we find the inertia tensor of the four quarter pieces of a torus to be

$$I^{\frac{1}{4}torus}_{O} = \begin{pmatrix} 2(36+17\pi) & 0 & 0 \\ 0 & 12(12+5\pi) & 0 \\ 0 & 0 & 2(36+17\pi) \end{pmatrix} a^4\pi\sigma \qquad (3.3.44)$$

We can now add all of the inertia tensor components together to determine the inertia

109

tensor of the link, $I_O^{link} = I_O^{\frac{1}{4}tensor} + I_O^{cyl} + I_O^{torus}$:

$$I_O^{link} = \begin{pmatrix} A & 0 & 0 \\ 0 & C & 0 \\ 0 & 0 & D \end{pmatrix} \frac{2a^4\pi\sigma}{3} \tag{3.3.45}$$

where $A = (238 + (351 + 96\sqrt{2}\pi))$, $C = 2(226 + (321 + 96\sqrt{2}\pi))$ and $D = (238 + (351 + 96\sqrt{2}\pi))$.

3.4 Conclusion

In this chapter we made some progress towards our goal of determining the true symmetry of the knots and links used in our model. We calculated the moment of inertia tensor several hollow and solid link configurations based on geometry alone, and generalized the solution for a chain of 'n' elements. The inertia tensors are given in terms of the density of the link and radius of the flux tube 'a'. We currently do not know the physical scale of the radius of the flux tube, therefore we need to estimate its value using the Bag Model as a guide. In addition, once we determine numerical values for the eigenvalues of the inertia tensor, we need to understand how to determine the symmetry of the link and how to caculate its rotational energy. These topics are tackled in Chapter IV.

CHAPTER IV

ROTATIONAL ENERGY

4.1 Introduction

In Chapter II, we established a hypothesis where glueball candidates are modeled as tightly knotted or linked chromoelectric flux tubes. In the model an approximation was made about how to treat the candidates in order to calculate the rotational energies. The glueball candidates were approximated as spherical rigid rotors. However, if we calculate the moment of inertia tensor of knots/links identified with glueball candidates, we find that only one of the candidates (link 6_2^3, the Borromean Rings) is in fact a spherical rigid rotor. Therefore, it is worth examining all of the knots and links used in the model in order to determine how they should be classified.

In Chapter III, we calculated the moment of inertia tensor for several links and our results are expressed in terms of the radius of the flux tube, a. In order to calculate a numerical value for the principal moments of inertia, we will need to determine the radius of the flux tube. Since we cannot measure or compute from fundamentals the radius of the flux tube, we will utilize the Bag Model to calculate the radius. We will begin with an overview of the Bag Model.

4.2 <u>Bag Model</u>

QCD as presented in the introduction provides of the strong interaction. The strength of the strong interaction (as measured by the QCD potential) grows steadily as the distance between strongly interacting particles increases. At small distances, QCD has few problems; however at large distances there are many problems not easily solved. Numerical calculations [39] show that the QCD potential grows linearly with distance beyond 1 fm. As a result, in QCD there is a constant long-range force between strongly interacting particles, compared to QED where the force between charged particles decreases like the square of the distance. This leads to confinement, which states that even though high energy experiments have provided evidence that hadrons are composed of quarks and gluons we are not able to see free quarks and gluons. Confinement presents the dilemma that in the regime where QCD is calculable few experiments are so far available, whereas in the regime where much data exists the theory admits few results [40].

In order to make sense of these results, it is necessary to consider phenomenological approximations. There are several models of confinement, but for our particular purpose, the most useful of these models are the "Bag Models" which postulate that quarks and gluons are confined to a given volume V. At the heart of bag phenomenology is the assumption that the vacuum can have more than one phase. This phase of the vacuum can appear as localized regions within another; for example bubbles in a liquid would be an analogy. Models based on a two-phase structure of the non-Abelian vacuum form the basis for bag phenomenology. The two-phase structure

refers to the idea that the vacuum inside the bag is different than the vacuum outside of the bag. It should be noted that phenomenological models are at best effective theories with only an underlying connection to the theory of QCD.

In QED the dielectric constant of the vacuum state is set as 1, i.e.

$$\kappa_{vac}^{QED} = 1. \tag{4.2.1}$$

The relationship between the displacement vector $\mathbf{D}$, the electric field $\mathbf{E}$ and the polarization $\mathbf{P}$ is:

$$\mathbf{D} = \mathbf{E} + \mathbf{P}. \tag{4.2.2}$$

where $\mathbf{D}$ is the field created by the source charges and $\mathbf{E}$ is the total field including charges from induced charges. As a result of the electric field, atoms will have a polarization, $\mathbf{P}$, in the same direction as $\mathbf{E}$ which creates a screening effect. The dielectric constant is defined as

$$\mathbf{D} = \kappa^{QED}\mathbf{E}, \tag{4.2.3}$$

and for any physical medium the dielectric constant satisfies $\kappa_{med}^{QED} \geq 1$.

Now, we would like to consider a medium that is *antiscreening* in order to model the theory of QCD. We imagine a medium in which $\kappa^{QCD} << 1$. It can be shown that a test charge immersed in this particular medium will dig a stable "hole" in the medium and inside the hole surrounding the test charge the dielectric constant κ^{QCD} is 1 but the medium outside of the hole is $\kappa^{QCD} << 1$ [42, 43]. This idea is shown in Figure 32. This model is the basis of several models [42, 43, 44] which produce confinement. Whenever particles carrying color changes, i.e. gluons and/or quarks,
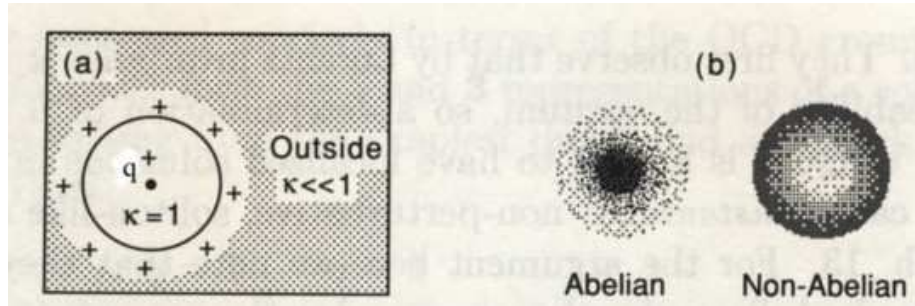
Figure 32: (a) Test charge q$^+$ in an antiscreening medium. The induced charge on the sphere is of the same sign as the test charge because medium antiscreens. (b) Drawing of the spatial distribution of an effective charge in Abelian and non-Abelian field theories [40].

are in the antiscreening QCD vacuum, from the model we would expect holes to develop in the vacuum around the particles. These regions are called *bags*. Inside the bags $\kappa_{in}^{QCD} = 1$, whereas outside the bag $\kappa_{\infty}^{QCD} << 1$ or more simply $\kappa_{\infty}^{QCD} = 0$. As a result, if the total color inside the bag is not zero, the mass of the bag becomes infinite at the boundary and if there is no net color inside the bag, the bag mass is finite as $\kappa_{\infty}^{QCD} \rightarrow 0$. Therefore, confinement is forced upon strongly interacting particles by the assumption that their mass is small inside the bag volume, but becomes very large outside of the bag.

Basic Bags

Our motivation for discussing bag models is to calculate the radius of the knotted or linked chromoeletric flux tube used in our model. A physical value for the radius is necessary in order to compute the rotational energies of a given knot or link. To

114

begin with, we can say that a glueball looks like a bubble immersed in a complex medium that is the true QCD vacuum. We will assume the simplest model and say that the inside and the outside of the bag are in two different phases, where the value of the effective color dielectric constant defines these phases. We also assume that the boundary between the phases is sharp. From these assumptions, the energy of the bag can be written as [41]

$$E_{bag} = E_{QCD}^{Total} - u_{vac}V \qquad (4.2.4)$$

where E_{QCD}^{Total} is the total energy of the system, u_{vac} is the energy density of the normal vacuum and V is the total volume of the system. If we let V_{bag} be the volume of the bubble and E_0 the energy of the fields inside the bubble, then we can write the total energy of the system, E_{QCD}^{Total}, as

$$E_{QCD}^{Total} = E_0 + u_{vac}(V - V_{bag}) \qquad (4.2.5)$$

We can combine Equations (4.2.4) and (4.2.5) to obtain the energy of the bag as

$$E_{bag} = E_0 - u_{vac}V_{bag} \qquad (4.2.6)$$

We can rewrite Equation (4.2.6) in terms of the bag constant, B, introduced by the M.I.T. Bag model [44]. In the M.I.T. Bag model, the bag constant is defined as

$$B = -u_{vac} \qquad (4.2.7)$$

Allowing us to rewrite Equation (4.2.6) as

$$E_{bag} = E_0 + BV_{bag} \qquad (4.2.8)$$

To prevent the bubble from growing indefinitely, we want $B \geq 0$. This requirement implies that the energy density of the normal vacuum is lower than the bubble vacuum, which by convention is taken to be zero. Therefore, the energy required to make a bubble in the vacuum is BV_{bag}.

We note that the above calculation could also include a term which represents the surface energy of the bag, however this term is typically small compared to the volume energy (BV_{bag}) and is frequently neglected.

4.3   Radius of Flux Tube Calculation

To calculate the radius of the tightly linked or knotted chromoelectric flux tubes used in our model, we want to find the bag energy as defined in Equation (4.2.8). Once we have an expression for the bag energy, we will minimize it to determine the radius, a. We will need to define the volume of our bag, and then the fields inside the bubble, E_0. In our model, the bag is a knotted or linked flux tube, which if unknotted or unlinked would be a torus or set of tori. The shape of our bag would then be a cylinder, which is given by the following

$$V_{bag} = \pi a^2 l \tag{4.3.1}$$

where l is the ropelength of the knot or link as defined in Chapter 2 and a is the radius of the tube. The energy, E_O, stored in the chromoelectric field $\mathbf{E}$ is defined as

$$E_0 = \frac{\kappa^{QCD}}{2} \int E^2 dV = \frac{\pi \kappa^{QCD} a^2 l E^2}{2} \tag{4.3.2}$$

where κ^{QCD} is the color dielectric constant and $E^2 = \mathbf{E} \cdot \mathbf{E}$.

We can then write the energy of the bag, E_{bag}, as follows

$$E_{bag} = \pi r^2 l B + \frac{\pi \kappa^{QCD} a^2 l E^2}{2} \tag{4.3.3}$$

As discussed in Chapter II, for each knot or link there is a topological invariant defined as ϵ_k which is called the knot or link energy. The knot or link energy is related to the ropelength and the radius of the tube; $\epsilon_k = \frac{l}{2a}$ is a constant for each tight knot or link. We can use this relationship to eliminate l, since we know the value of ϵ_k for each knot/link configuration. We obtain the following

$$E_{bag} = 2\pi a^3 \epsilon_k B + \pi a^3 \epsilon_k \kappa^{QCD} E^2 \tag{4.3.4}$$

The chromoelectric flux, Φ, of $\mathbf{E}$ through the tube is assumed to be constant according to our model and we also assume that the tube carries a single quantum of flux, i.e.

$$\Phi = \int \mathbf{E} \cdot dA = \pi a^2 E = 1 \tag{4.3.5}$$

We can now write E as follows

$$E = \frac{\Phi}{\pi a^2} = \frac{1}{\pi a^2} \tag{4.3.6}$$

We can then rewrite the field energy as

$$E_0 = \frac{\pi a^3 \epsilon_k \kappa^{QCD}}{\pi^2 a^4} = \frac{\epsilon_k \kappa^{QCD}}{\pi a} \tag{4.3.7}$$

Finally, we can write the bag energy as

$$E_{bag} = 2\epsilon_k (\pi a^3 B + \frac{\kappa^{QCD}}{2\pi a}) \tag{4.3.8}$$

The radius of the tube, a, is determined by minimizing the bag energy E_{bag}. From $-dE_{bag}/da = 0$, we find

$$-2\epsilon_k(3\pi a^2 B - \frac{\kappa^{QCD}}{2\pi a^2}) = 0 \qquad (4.3.9)$$

or

$$3Ba^4 = \frac{\kappa^{QCD}}{2\pi^2} \qquad (4.3.10)$$

From the previous discussion on bag models, the dielectric constant, κ^{QCD}, inside the bag is 1. We will take the bag constant as a phenomenological parameter which is fitted. If we set $B = 13 \frac{\text{MeV}}{\text{fm}^3}$ we find one real, positive value for the radius $a = 0.73$ fm. If we plug this radius back into the equation for the bag energy with the value of $\epsilon_k = 4\pi$ for the shortest link, we find $E_{bag} = 744$ MeV which corresponds to the lowest glueball state identified with the shortest link, $f_0(600) = 400 - 1200$ MeV.

4.4 Rotational Energy

We model glueball candidates as knotted and linked chromoelectric flux tubes. The glueball ground state prediction is based on a relationship between the knot/link length and the energy. In addition, we also predict excited states which are rotationally excited knotted/linked chromoelectric flux tubes. In order to determine the energy levels of the knotted/linked flux tubes, we will follow the already established method used to determine the rotational spectra of molecules. We consider the glueball candidates to be arbitrarily shaped rigid rotors, which are rigid bodies of arbitrary shape with a fixed center of mass whose energy consists only of rotational kinetic energy.

4.4.1 Introduction to Rotational Spectra

We can classify rotational energy spectra by their principal moments of inertia [45]. The principal moments of inertia calculated reflect the unique geometry of the knot or link. We model glueballs as a collection of point masses fixed relative to each other, but free to rotate as a whole. The moment of inertia tensor, I, was previously defined in (3.2.1).

The moment of inertia tensor is real and symmetric, i.e. it is Hermitian, and it can be diagonalized to give three possibly distinct eigenvalues. The eigenvalues are referred to as the principal moments of inertia, and the eigenvectors corresponding to the diagonalized coordinate system are the principal axes. The diagonalized moment of inertia tensor has the form

$$\mathbf{I} = \begin{pmatrix} I_a & 0 & 0 \\ 0 & I_b & 0 \\ 0 & 0 & I_c \end{pmatrix} \tag{4.4.1}$$

where I_a, I_b and I_c are the principal moments of inertia.

On can always find one axis, the c-axis, about which the moment of inertia has its maximum value, and another axis, labeled the a-axis, about which I has its minimum value. Conventionally, the principal axes are ordered in the following manner: $I_a \leq I_b \leq I_c$.

Rigid rotors are classified as follows: If all three principal moments of inertia are equal, we have a *spherical top*. If two principal moments are equal, we have a *symmetric top*. A *prolate* symmetric top has $I_b = I_c$ and the a axis is the symmetry

119

axis; an *oblate* symmetric top has $I_a = I_b$ and the c axis is the symmetry axis. A prolate top is cigar-shaped, whereas an oblate top is disc-shaped. If all three principal moments are unequal, we have an *asymmetric top*.

If we use these principal axes, then the components of the rotational angular momentum **J** along these axes are

$$J_a = I_a \omega_a, \tag{4.4.2}$$

$$J_b = I_b \omega_b, \tag{4.4.3}$$

$$J_c = I_c \omega_c. \tag{4.4.4}$$

The kinetic energy for a rigid rotor [47] can then be written as

$$T_{rot} = \frac{J_a^2}{2I_a} + \frac{J_b^2}{2I_b} + \frac{J_c^2}{2I_c} \tag{4.4.5}$$

4.4.2 Rotational Energy of a Spherically Symmetric Top

First, we will examine the case of a spherically symmetric top, where all three principal components of the moment of inertia tensor are equal with $I_a = I_b = I_c = I$.

The quantum mechanical energy of rotation for a spherically symmetric top is given by the Hamiltonian, which we find by replacing the angular momentum components in Equation 4.4.5 with their respective operators and is given by

$$H_{rot} = \frac{\hat{J}_a^2}{2I_a} + \frac{\hat{J}_b^2}{2I_b} + \frac{\hat{J}_c^2}{2I_c} \tag{4.4.6}$$

The total angular momentum operator has the following eigenvalue

$$\hat{J}^2 \psi = J(J+1)\psi, \, J = 0, 1, 2, 3, ... \tag{4.4.7}$$

Using the the fact that $I_a = I_b = I_c = I$, we can write the rotational energy levels as

$$E_{rot}^{sphere} = \frac{J(J+1)}{2I}, \quad J = 0, 1, 2, 3, ... \tag{4.4.8}$$

Most of the knots and links in our model do not possess spherical symmetry, as a consequence they will not fall into this category.

4.4.3 Rotational Energy of a Symmetric Top

The next case we will consider is a symmetric top. There are two classes of symmetric tops: oblate symmetric with $I_a = I_b < I_c$ and prolate symmetric with $I_a < I_b = I_c$.

For a prolate top, $I_b = I_c$, so we can rewrite the Equation 4.4.6 as

$$H^{rot} = \frac{1}{2}\left(\frac{\hat{J}_a^2}{I_a} + \frac{\hat{J}^2}{I_b} - \frac{\hat{J}_a^2}{I_b} - \frac{\hat{J}_c^2}{I_b} + \frac{\hat{J}_c^2}{I_c}\right) \tag{4.4.9}$$

or

$$H^{rot} = \frac{1}{2}\left(\frac{\hat{J}_a^2}{I_a} + \frac{\hat{J}^2}{I_b} - \frac{\hat{J}_a^2}{I_b}\right). \tag{4.4.10}$$

We know that $\hat{J}^2\psi = J(J+1)\psi$. Each of the components corresponding to angular momentum along one of the principal axes is quantized in units of K, energy proportional to K^2, e.g. $\hat{J}_a^2\psi = K^2\psi$. For the symmetric top, K is a new (good) quantum number that measures the component of angular momentum along the main axis [46]. Equal positive and negative values of K result in the same energy values. Thus, for a prolate top we find the following

$$E_{rot}^p = \frac{J(J+1)}{2I_b} + \frac{K^2}{2}\left(\frac{1}{I_a} - \frac{1}{I_b}\right) \tag{4.4.11}$$

or

$$E_{rot}^{p} = BJ(J+1) + K^2(A-B). \tag{4.4.12}$$

where the three rotational constants are defined as follows

$$A \; = \; \frac{1}{2I_a}, \quad B \; = \; \frac{1}{2I_b}, \quad C \; = \; \frac{1}{2I_c} \tag{4.4.13}$$

For an oblate top, we find through similar steps the following

$$E_{rot}^{o} = BJ(J+1) + K^2(C-B). \tag{4.4.14}$$

The quantum number K can take values $K = 0, \pm1, \pm2, ..., \pm J$ where all levels for $K > 0$ are doubly degenerate.

The energies depend on K via the relative values of the rotational constants, A, B and C. The magnitude of K tells us how much of the angular momentum comes from motion about the symmetry axis, and consequently how the energy depends on the moment of inertia about that axis [54]. When $K \approx J$, the top is rotating fast around its symmetry axis and when $K = 0$ there is no rotation about the symmetry axis.

4.4.4 Rotational Energy of an Asymmetric Top

Most of the knots/links we will consider are not symmetric tops, meaning they fall into the category of asymmetric tops. In the case of an asymmetric top, all three moments of inertia are different ($I_a \neq I_b \neq I_c$). Since all three principal moments of inertia are unequal, we cannot easily determine the rotational energy from the Hamiltonian as in the previous sections. The main difference between the case of an

asymmetric top and a symmetric top is that the asymmetry removes the degeneracy of the different K levels.[48]. There are several general expressions [49, 50] in the literature to compute the energy levels of an asymmetric top, we have chosen the expression derived by Wang [51].

Given the three rotational constants, an asymmetric rotor can be characterized by its Ray's asymmetry parameter

$$\kappa = \frac{2B - A - C}{A - C}, \tag{4.4.15}$$

which becomes -1 for a prolate symmetric top (B = C) and 1 for an oblate symmetric top (B = A), and the most asymmetric case has $\kappa = 0$. Note that the Ray's asymmetry parameter, κ, is not related to the dielectric constant, κ, referred to at the beginning of the chapter. The energy levels of an asymmetric top are different from prolate and oblate symmetric tops in that the K levels, which are always degenerate for symmetric tops, are split in the asymmetric top [52]. For each level of J, the asymmetric top has $(2J + 1)$ distinct rotational sublevels; the symmetric rotor has $(J + 1)$ distinct sublevels for each J value. As the asymmetry increases, i.e. κ approaches 0, the "K splitting" increases until there is no longer any close correspondence between the two levels and the degenerate K levels of the symmetric top.

For the energy expression, we will need two more parameters, b_p and b_o, defined as follows.

$$b_p = \frac{C - B}{2A - B - C} = \frac{\kappa + 1}{\kappa - 3} \tag{4.4.16}$$

b_p is zero for a prolate symmetric top, and increases in size as the top becomes more

asymmetric. The analogous asymmetry parameter for an asymmetric oblate top is

$$b_o = \frac{A - B}{2C - B - A} = \frac{\kappa - 1}{\kappa + 3} \tag{4.4.17}$$

For an asymmetric top, the total angular momentum J and its projection M_J on an axis fixed in space are constants of the motion and "good" quantum numbers which can be used to specify the state of the rotor [53]. Note that both M_J and K are projections of J, however M_J is the projection of J about the fixed laboratory z-axis whereas K is the component of the angular momentum about the symmetry axis. In both the classical motion and the quantum-mechanical solution the component of the angular momentum is not constant along any direction in the rotating asymmetric body. This means that the quantum number K is no longer a "good" quantum number and cannot be used to specify the rotational state. In reality, there are no convenient quantum numbers which can be used to specify the state and also have physical meaning. We have chosen one particular approximation for the asymmetric top, in which K has been replaced by a pseudo-quantum number that has no physical meaning. We will use the pseudo-quantum number, w, to designate the energy levels.

If the knot or link is an asymmetric prolate top, the energy may be written in the approximate form

$$E_{rot}^p = \frac{B + C}{2} J(J + 1) + \left(A - \frac{B + C}{2} \right) w \tag{4.4.18}$$

This is very similar to the rotational energy of a symmetric prolate top. Exact expressions for some of the various possible values of w are given in Table 4.4.1, and the parameter b represents either b_p or b_o depending on the symmetry. Further values

for w associated with higher J values can be found in [53]. For the oblate case, we

Table 4.4.1: Values of the parameter w in terms of the parameter b for an asymmetric prolate or oblate top.

J	w
0	0
1	1 - b
1	0
1	1 + b
2	$2(1 - \sqrt{1 + 3b^2})$
2	1 - $3b$
2	4
2	1 + $3b$
2	$2(1 + \sqrt{1 + 3b^2})$
3	$2(1 - \sqrt{1 + 15b^2})$
3	$5 - 3b - 2\sqrt{2}\sqrt{2 + 3b + 3b^2}$
3	$5 + 3b - 2\sqrt{2}\sqrt{2 - 3b + 3b^2}$
3	4
3	$5 + 3b + 2\sqrt{2}\sqrt{2 - 3b + 3b^2}$
3	$5 - 3b + 2\sqrt{2}\sqrt{2 + 3b + 3b^2}$
3	$2(1 + \sqrt{1 + 15b^2})$

find a similar formulas. The energy is

$$E_{rot}^o = \frac{A + B}{2}J(J + 1) + \left(C - \frac{A + B}{2}\right)w \qquad (4.4.19)$$

4.5   Conclusion

This chapter served primarily as an introduction to the theoretical background essential to the following chapter. The chapter began with an introduction to the Bag Model, which we subsequently used to estimate the physical size of the radius of the tightly knotted or linked flux tubes modeled as glueball candidates in Chapter II. The remainder of the chapter focused on the physics of the rotational energy of

rigid rotors as well as presented how to classify rigid rotors based on their symmetry properties. The calculations and definitions presented in this chapter allow us to calculate the rotational energies for the knots and links used in the model outlined in Chapter II.

CHAPTER V

CALCULATION OF ROTATIONAL ENERGY

5.1   Introduction

In Chapters III and IV we performed calculations and discussed theory that will now allow us to calculate rotational energies for the knots and links used in the glueball model detailed in Chapter II. As stated earlier, the model assumes all knotted and linked flux tubes to be spherical tops for the purpose of approximating the excitation energy of a particular glueball candidate. In this chapter we will show that only one of the knots or links used in the model is in a fact a spherical top, and we will calculate classify the symmetry of the remainder. Based on their classifications, we will calculate their rotational energies.

In chapter III we performed exact calculations of the moment of inertia for specific link geometries, however for most knots and links exact calculations are not possible. We will calculate the moment of inertia of these knots and links from a set of vertex points, i.e. the set of numerically determined coordinates of each knot or link.

We begin the chapter with the calculation of the simplest link: the Hopf link. We can calculate the rotational energy of the Hopf link based on the moment of inertia tensor calculation from Chapter III. We can also calculate the rotational energy based on a set of vertex coordinate points. We will compare both calculations, and use this comparison as a way to approximate an error in the vertex coordinate points for

symmetric tops.

After examining the Hopf link, we will go through several sample rotational energy calculations that represent a wide variety of knots/links. At the end of the chapter, the rotational energies of all knots and links will be tabulated.

5.2   Rotational Energy Calculations

5.2.1   Rotational Energy of Hopf link

In order to calculate the rotational energy of a particle modeled as two flux tubes in a tight Hopf link configuration, we need the mass of the particle, the radius of the flux tubes and the shape of the Hopf link. The Hopf link is associated with the pseudoscaler meson $f_0(600)$. In an earlier calculation, we used the MIT bag model approach to calculate the radius, a, of each knotted or linked flux tube used in our model and we found it to be $a = 0.71$ fm. In (3.2.15), we found the principal moments of inertia of the Hopf link to be $I_a = \pi^2 a^5 \rho$ and $I_b = I_c = \frac{75}{2}\pi^2 a^5 \rho$. Plugging in numerical values for the variables, we find

$$
\begin{aligned}
I_a &= 21\pi^2 a^5 \rho = 21\pi^2 (0.71 \text{ fm})^5 \left(\frac{800 \text{ MeV}}{8\pi^2 (0.71 \text{ fm})^3} \right) = 1058.61 \text{ MeV fm}^2 \\
I_b &= \frac{75}{2}\pi^2 a^5 \rho = \frac{75}{2}\pi^2 (0.71 \text{ fm})^5 \left(\frac{800 \text{ MeV}}{8\pi^2 (0.71 \text{ fm})^3} \right) = 1890.38 \text{ MeV fm}^2 \\
I_c &= \frac{75}{2}\pi^2 a^5 \rho = \frac{75}{2}\pi^2 (0.71 \text{ fm})^5 \left(\frac{800 \text{ MeV}}{8\pi^2 (0.71 \text{ fm})^3} \right) = 1890.38 \text{ MeV fm}^2 \quad (5.2.1)
\end{aligned}
$$

We calculate the rotational constants, A, B and C previously defined in Equation 4.4.13, in order to determine the shape of the knot and ultimately the rotational

128

energy. For the Hopf link, we find the following values for the rotational constants

$$A = \frac{1}{2I_a} = 4.72 \times 10^{-4} \text{ MeV}^{-1} \text{ fm}^{-2}$$

$$B = C = \frac{1}{2I_b} = 2.64 \times 10^{-4} \text{ MeV}^{-1} \text{ fm}^{-2} \qquad (5.2.2)$$

As defined in Chapter IV, the rotational constants are used to calculate the Ray's Asymmetry parameter and ultimately the rotational energy relationship used. For the Hopf link, $\kappa = -1$, meaning it is a prolate symmetric top. We are able to calculate the rotational energy, using the rotational energy relationship defined for a prolate symmetric top in Equation 4.4.12.

Lastly, before we calculate the rotational energy for the Hopf Link we need to change the units of the rotational constants A and B so that the resultant energy is in units of MeV; using 200 MeV fm $\cong$ 1 gives

$$A = 18.89 \text{ MeV}$$

$$B = 10.58 \text{ MeV} \qquad (5.2.3)$$

Finally, the energy depends on the quantum numbers J and K; Table 5.2.1 summarizes the rotational energy results for the Hopf Link. From the rotational energies, we can calculate the predicted rotational states for the $f_0(600)$ whose ground state energy is listed by the Particle Data Group as 800 ± 400 MeV. The predictions are summarized in Table 5.2.2, along with the published error associated with the $f_0(600)$. However, given the short lifetime of the $f_0(600)$, ($\approx 8 \times 10^{-25}$ sec), these excited states are unlikely to be seen experimentally.

Table 5.2.1: Hopf Link Excitation Energy

J	K	E_{rot}(MeV)
1	0	21
1	1	29
2	0	63
2	1	72
2	2	97
3	0	127
3	1	135
3	2	160
3	3	202

Table 5.2.2: Predicted Excitation states of the $f_0(600)$

J	K	E_J(MeV)
0	0	800 ± 400
1	0	821 ± 400
1	1	829 ± 400
2	0	863 ± 400
2	1	872 ± 400
2	2	897 ± 400
3	0	927 ± 400
3	1	935 ± 400
3	2	960 ± 400
3	3	1002 ± 400

5.2.2   Rotational Energy based on Vertex Points

Since we cannot calculate the moment of inertia tensor from geometry alone in most cases, we use a set of vertex points unique to each knot and link. Based on the

inertia tensor defined in Equation (3.2.2), its components I_{ij} can be expanded into

$$I = \begin{pmatrix} \sum_\alpha m_\alpha(r_\alpha^2 - x_\alpha^2) & -\sum_\alpha m_\alpha x_\alpha y_\alpha & -\sum_\alpha m_\alpha x_\alpha z_\alpha \\ -\sum_\alpha m_\alpha y_\alpha x_\alpha & \sum_\alpha m_\alpha(r_\alpha^2 - y_\alpha^2) & -\sum_\alpha m_\alpha y_\alpha z_\alpha \\ -\sum_\alpha m_\alpha z_\alpha x_\alpha & -\sum_\alpha m_\alpha z_\alpha y_\alpha & \sum_\alpha m_\alpha(r_\alpha^2 - z_\alpha^2) \end{pmatrix} \qquad (5.2.4)$$

where $(x_\alpha, y_\alpha, z_\alpha)$ are coordinates in the center-of-mass frame, m_α is the mass associated with each point used in the calculation and $r_\alpha^2 = x_\alpha^2 + y_\alpha^2 + z_\alpha^2$.

5.2.3   Rotational Energy of Hopf link based on Vertex Points

The set of vertex points of the Hopf Link consists of 179 points [55]. The coordinates of the vertex points do not carry any physical units. However, in Chapter III we presented exact calculations for the inertia tensor of a Hopf link and we will use this result to create a scale for the vertex points. We assume the mass of each point is equal, so that m_α is calculated for each knot depending on the mass of the particle and the number of vertex points. The Hopf Link is associated with the $f_0(600)$, whose ground state mass is listed in Table 5.2.2; the mass of each point is then $m_\alpha = (800/179)$ MeV or $m_\alpha = 4.47$ MeV.

We use Mathematica to diagonalize the moment of inertia tensor and determine the principal moments of inertia, I_a, I_b and I_c. For the unscaled Hopf Link, we find the following values for the principal moments of inertia: $I_a = 1601.8$ MeV, $I_b = 3170.36$ MeV and $I_c = 3232.89$ MeV. In order to normalize the vertex points, we impose the condition that the trace of both inertia tensors be the same. In order for the trace of the inertia tensor, calculated from the coordinates of the vertex points, to equal the

trace from the exact calculation we need to multiply the coordinates of the vertex points by a factor of 0.77752. We will use this result to define our scale factor by defining the distance between adjacent vertex points as 0.77752 fm. Now that the vertex points have an associated length scale, we can now determine the principal moments of inertia with the proper units: $I_a = 968.35$ MeV fm^2, $I_b = 1916.61$ MeV fm^2, and $I_c = 1954.41$ MeV fm^2.

From these eigenvalues, we can calculate the rotational energies of the Hopf link and compare them with the exact calculation. The results calculated from the vertex points do not yield an exact symmetric top; the Ray's asymmetry parameter is: $\kappa_{vertex} = -0.961263$ compared to $\kappa_{exact} = -1$. However, since we know that it is in fact an exact symmetric top, we will calculate the rotational energies based on the relationship for a prolate symmetric top. Table 5.2.3 summarizes the rotational energy results for the Hopf Link calculated from the vertex points, E_{rot}^{vertex} and also includes the results from Table 5.2.1 as a way of comparison with the exact results, E_{rot}. The percentage error is calculated from the following relationship

$$\text{Error} = \left(\frac{\left| \text{E}_{rot}^{vertex} - \text{E}_{rot} \right|}{\text{E}_{rot}} \right) * 100\% \tag{5.2.5}$$

We also include the percentage error for each rotational energy level for the Hopf link. Since the Hopf link is the only case where we can calculate both the exact rotational energy and the rotational energy from the vertex points, we use this case to estimate the error in future vertex points calculations since we have no other way to determine the error.

Table 5.2.3: Hopf Link Excitation Energy

J	K	$E_{rot}^{vertex}(MeV)$	$E_{rot}(MeV)$	Error
1	0	21	21	1.37%
1	1	31	29	5.48%
2	0	63	63	1.37%
2	1	73	72	1.44%
2	2	103	97	6.98%
3	0	125	127	1.37%
3	1	135	135	0.12%
3	2	166	160	3.68%
3	3	217	202	7.64%

5.2.4 Rotational energy calculations for symmetric and asymmetric tops

For the Hopf Link, the Ray's asymmetry parameter was calculated to be -1; or in the case of the calculation based on the set of vertex coordinate points, very close to -1, and we know that in reality it is exactly -1 making it easy to argue for its status as a prolate symmetric top. However, most of the knots and links examined are not so easily classified as either a prolate or oblate symmetric top, $\kappa = -1$ and $\kappa = 1$ respectively. In fact, the majority of the knots and links examined have an asymmetry parameter of $-1 < \kappa < 1$. How do we determine what can be approximated as an oblate or prolate symmetric top, and what should be classified as an asymmetric top? Is there a large difference in rotational energies if we simply ignore the small asymmetry and assume the knot or link is a symmetric top? In order to explore these questions, we will go through a couple of rotational energy calculations in detail.

We first use the knot 5_2 as an example, which is shown in Figure 33. The knot 5_2 is identified with the meson $f_0(1500) = 1505 \pm 6$ MeV, as well as the excited states

$f_1(1510) = 1518 \pm 5$ MeV and $f_2(1525) = 1525 \pm 5$ MeV. The energies and errors are those listed by the Particle Data Group. The Ray's asymmetry parameter for the 5_2 is $\kappa = -0.678$; which means it is asymmetric but closer to a prolate top than an oblate top. Let's first look at what rotational energy values we find if we simply
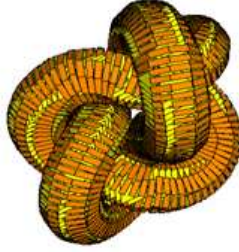
Figure 33: A tight configuration of knot 5_2, which in the model is identified with the meson $f_0(1500) = 1505 \pm 6$ MeV, as well as the excited states $f_1(1510) = 1518 \pm 5$ MeV and $f_2(1525) = 1525 \pm 5$ MeV.

assume it is a prolate symmetric top. Then, we will calculate the energies using the relationship for an asymmetric prolate top in order to see how much splitting occurs. We will focus on the excited states with $J = 1, 2$ cases, since we can compare those states with experimental data. The results, including the projected states calculated from the ground state $f_0(1500)$ and E_{rot}, are summarized in Table 5.2.4. Now, we will assume that 5_2 is an asymmetric prolate top. The energy for an asymmetric prolate top was defined in Equation 4.4.18, where the quantum number K has been replaced by w as discussed in Section 4.4.5. The possible values of the parameter w are defined in Table 4.4.1 and depend on the parameter b_p, defined in Equation 4.4.16. For our particular example of knot 5_2, $b_p = -0.0874538$.

As a result of the asymmetry, we have the splitting of energy levels and conse-

Table 5.2.4: 5_2 Excitation Energy and projected Excited States based on prolate symmetric top

J	K	E_{rot} (MeV)	E_J(MeV)
1	0	6	1511
1	1	9	1514
2	0	19	1524
2	1	22	1527
2	2	29	1534

quently we have more excited levels than in the case of an exactly prolate symmetric top. For $J = 1$, we have three excited states rather than two and for $J = 2$ we have five states rather than three. Treating knot 5_2 as an asymmetric prolate top we find the following rotational energies, summarized in Table 5.2.5. Examining tables 5.2.4

Table 5.2.5: 5_2 Excitation Energy based on an asymmetric prolate top

J	w	E_{rot} (MeV)	E_J (MeV)
1	0	7	1512
1	0.91	9	1514
1	1.09	9	1514
2	-0.02	20	1525
2	0.74	22	1527
2	1.26	23	1528
2	4.00	30	1535
2	4.02	30	1535

and 5.2.8, we find that for the knot 5_2 there is a small, but noticeable, difference between assuming that the knot is a prolate symmetric top and assuming it is an asymmetric top. Even though these splits may be small, we will include them in our

model.

Next we will look at a link that is considered to be very asymmetric; where $\kappa = 0$ is generally considered to be the most asymmetric case. We will look at link 5_1^2, which has a value of $\kappa = -0.0611502$ and in our model is not currently identified with any known state. We predict that it is coupled to an f ground state with an approximate mass of 1505 MeV. We will first assume that is a prolate symmetric top, which is summarized in Table 5.2.6. And in Table 5.2.7, we summarize the results based on

Table 5.2.6: 5_1^2 Excitation Energy and projected Excited States based on prolate symmetric top

J	K	E_{rot} (MeV)	E_J(MeV)
1	0	9	1514
1	1	9	1514
2	0	26	1531
2	1	27	1532
2	2	29	1534

the assumption that 5_1^2 an asymmetric top. Again, we examine tables 5.2.6 and 5.2.7 for the link 5_1^2 and we find a small, but noticeable, splitting of energy levels when we assume the link is not a prolate symmetric top. And we notice that the splitting is more noticeable than in the case of the knot 5_2, which is to be expected since it is less asymmetric. We will approximate a knot or link as an oblate (or prolate) symmetric top if its κ value is within the range 0.96 to 1 (or -1 to -0.96), which is based on the comparison of the κ value of the exact calculation of the Hopf link, $\kappa = -1$, with that

Table 5.2.7: 5_1^2 Excitation Energy based on a prolate asymmetric top

J	w	E_{rot} (MeV)	E_J (MeV)
1	0	8	1513
1	0.69	9	1514
1	1.31	9	1514
2	-0.26	24	1529
2	0.080	24	1529
2	1.92	26	1531
2	4.00	28	1533
2	4.26	28	15331

calculated from the vertex points, $\kappa = -0.96$. And, consequently, we will call a knot or link an asymmetric oblate (or prolate) top if its Ray's asymmetry value is within the range $-0.96 \leq \kappa \leq 0.96$.

5.2.5   Additional Rotational Energy Calculations

<u>Rotational Energy of the Hopf link with one double flux</u>

Following the same steps as outlined in the previous section, we can calculate the rotational energy of the Hopf link where one tube carries double flux. The difference in our calculation will be the mass of the link; in our model, the Hopf link with one double flux is paired with the $f_0(1200 - 1600)$ particle. We previously averaged the mass of the $f_0(1200 - 1600)$ to be 1325 ± 12 MeV. The volume of the tube with double flux is $V_1 = 8\pi^2(1 + \sqrt{2})a^3$ and the volume of the tube with single flux is $V_2 = 2\pi^2(1 + \sqrt{2})a^3$, giving the link a total volume of $V = 10\pi^2(1 + \sqrt{2})a^3$. For the

principal moments of inertia, we then find

$$I_a = \frac{1}{4}(109 + 85\sqrt{2}) \left(\frac{(1325 \text{ MeV}\pi^2)(0.71 \text{ fm})^5}{10\pi^2(1 + \sqrt{2})(0.71 \text{ fm})^3} \right) = 567.42 \text{ MeV fm}^2$$

$$I_b = \frac{1}{2}(85 + 69\sqrt{2}) \left(\frac{(1325 \text{ MeV}\pi^2)(0.71 \text{ fm})^5}{10\pi^2(1 + \sqrt{2})(0.71 \text{ fm})^3} \right) = 903.98 \text{ MeV fm}^2$$

$$I_c = \frac{1}{4}(201 + 161\sqrt{2}) \left(\frac{(1325 \text{ MeV}\pi^2)(0.71 \text{ fm})^5}{10\pi^2(1 + \sqrt{2})(0.71 \text{ fm})^3} \right) = 1061.24 \text{ MeV fm}^2 \quad (5.2.6)$$

For the Hopf link with one double flux, we find the following values for the rotational

constants

$$A = \frac{1}{2I_a} = 8.83 \times 10^{-4} \text{ MeV}^{-1} \text{ fm}^{-2} = 35.25 \text{ MeV}$$

$$B = \frac{1}{2I_b} = 5.54 \times 10^{-4} \text{ MeV}^{-1} \text{ fm}^{-2} = 22.12 \text{ MeV}$$

$$C = \frac{1}{2I_b} = 4.72 \times 10^{-4} \text{ MeV}^{-1} \text{ fm}^{-2} = 18.85 \text{ MeV} \quad (5.2.7)$$

The Ray's asymmetry parameter is calculated to be $\kappa = -0.600209$. The Hopf link

with one double flux is an asymmetric prolate top. In this case, we use Equation

4.4.18 to calculate the rotational energies. Equation 4.4.18 depends on the parameter

w, whose values are listed in Table 4.4.1, which in turn depend on the parameter b_p

given by Equation 4.4.16. For our particular geometry, $b_p = -0.111047$.

As a result of the asymmetry, we have the splitting of energy levels. Treating

the Hopf link with one double flux as an asymmetric prolate top we find the follow-

ing rotational energies, summarized in Table 5.2.8. However, like the $f_0(600)$, the

$f_0(1200 - 1600)$ has a short lifetime of $\approx 5 \times 10^{-25}$ sec; and the excited states are

unlikely to be measured experimentally.

Table 5.2.8: Hopf link with double flux Excitation Energy

J	w	E_{rot} (MeV)	E_J (MeV)
1	0	41	1366
1	0.89	54	1379
1	1.11	57	1382
2	-0.04	122	1447
2	0.67	133	1458
2	1.33	143	1468
2	4.00	182	1507
2	4.04	183	1508

Rotational Energy of Link $2_1^2 \# 2_1^2$

To determine the rotational energy for link $2_1^2 * 0_1$ we will follow the same steps as outlined for the Hopf link. The Ray's asymmetry parameter is calculated to be $\kappa = -0.98$, making it very close to a prolate symmetric top. We will take it to be prolate symmetric top for our calculation of the rotational energy. In our model, the link $2_1^2 * 0_1$ is associated with the excited state $f_2(1270)$ whose mass is listed as M = 1275.1 ± 1.2 MeV. Since all excited states are based on the ground state, $E_J = E_0 + E_{rot}$, we need to calculate the ground state energy, E_0. If we express E_{rot} in terms of E_0 and set $J = 2$ and $K = 0$, we can solve for E_0. We find $E_0 = 1215.06$ MeV. The rotational energies and the predicted states are listed in Table 5.2.9.

Table 5.2.9: Rotational Energy of Link $2_1^2 * 0_1$

J	K	E_{rot} (MeV)	E_J (MeV)
0	0	0	1215
1	0	20	1235
1	1	47	1262
2	0	60	1275
2	1	87	1302
2	2	166	1381

5.3   Tables

5.3.1   Rotational Energy of Spherical Top in Table 5.4.2

In Table 5.4.2 we present the one link that we know is a spherical top: the Borromean rings, i.e. link 6_3^2. The principal moments of inertia were calculated from a set of vertex coordinate points. Since this calculation does not produce an exact result, we found that the moment of inertia eigenvalues were not all equal. However, since we know they should be equal, we averaged all three values in order to calculate the rotational energy using Equation 4.4.8. From our calculation, we found $I_a = 5818.56$ MeV fm^2, $I_b = 6115.27$ MeV fm^2 and $I_c = 6125.04$ MeV fm^2. When averaged, we find $I_{avg} = 6019.62$ MeV fm^2

5.3.2   Rotational Energy of Prolate and Oblate Tops in Table 5.4.3.

Table 5.4.3 lists the rotational energies calculated for the few knots and links that from their Ray's asymmetry parameter can be classified as prolate or oblate symmetric tops. The table lists the specific knot or link, the state identified with the

knot or link in the model specified in Table 2.7.1 in Chapter II, the quantum numbers J and K, the rotational energy, E_{rot} in MeV, and the actual or projected state, E_J in MeV. The energy of the state used to calculate the rotational energy, either directly pulled from the Particle Data Group or based on predictions from our model detailed in Chapter II, is listed in bold face to distinguish it from theoretical predictions.

The Hopf link is the first entry in the table, and the details are given at the beginning of the chapter. Since the rotational energies were calculated from the exact geometry of the Hopf link, the only associated error is related to the calculation of the radius, a, which cannot be estimated. The predicted rotational energies, E_J, for the Hopf link then include only the error associated the state $f_0(600)$, i.e. 400 MeV, determined by the Particle Data Group.

The next entry is the trefoil, 3_1, which is paired with the $f_0(980)$. The rotational energies are calculated from a set of vertex coordinate points, we expect some related error. However, we do not know the error associated with the vertex coordinate points. We conclude that the only way to estimate the error of the vertex points is by a direct comparison, as we worked out for the Hopf link earlier in this chapter. The Hopf link is the only case where we can calculate the rotational energy exactly and from a set of vertex points, and the results of this comparison are listed in Table 5.2.3. Consequently, we use the errors calculated in Table 5.2.3 to estimate the errors for calculations based on a set of vertex points in Table 5.4.3. We consider these errors to be an overestimate, since the calculation of the Hopf link rotational energies is based on 179 vertex coordinate points compared to 400 vertex coordinate points

for knots 3_1 and 4_1 and 562 vertex coordinate points for link 6_2^2. We would expect the errors to go down when more vertex coordinate points are used for a calculation, and to go up with the length of the knot; however, we assume the errors from the vertex coordinate points dominate. The predictions for the rotational energies, E_J, of the trefoil then include the estimated error associated with vertex coordinate points listed in the E_{rot} (MeV) column in addition to the error associated with the particle state $f_0(980)$, i.e. 10 MeV.

The error associated with the rotational energy of knot 4_1 was calculated similarly. The particle state associated with link 6_2^2 is a predicted state based on the model outlined in Chapter II and is listed in brackets to distinguish it from experimentally observed states. As such, the error associated with this state is based on our calculations in Chapter II. The errors associated with the predicted rotational energies for link 6_2^2 then include the error estimated from the vertex coordinate points in addition to our estimated error for the predicted state. The rotational energy associated with the link $2_1^2 \# 0_1$ was calculated exactly, so the only error included is that associated with particle $f_2(1270)$. The details of the ground state calculation based on $f_2(1270)$ are given earlier in this chapter.

5.3.3 Rotational Energy of asymmetric tops in Tables 5.4.4 - 5.4.14.

While table 5.4.3 represents knots and links classified as oblate or prolate symmetric tops, the Tables 5.4.4 - 5.4.14 list the rotational energies of knots and links classified as prolate or oblate asymmetric tops. Instead of the quantum numbers J

and K, we use J and w since K is no longer a good quantum number for an asymmetric top as discussed in Chapter IV. The parameter w depends on κ and was defined in Table 4.4.1.

In the previous table, we were able to estimate the error on the rotational energies. However, since these rotational energies depend on J and w we have no calculation upon which to base our errors. As such, we will not presume to add errors to these excitation energies. We would assume them to be on the same order or less as those calculated based on the Hopf link. We hope to be able to estimate the errors in the future, when sets of vertex coordinate points for more complicated links become available.

Since the number of knots and links increases dramatically with length, we have chosen to calculate only the rotational energies for those states predicted by our model (i.e. the particle states listed in brackets) up to 2 GeV. Therefore, we only include the rotational energies for those observed states listed by the Particle Data Group. In the future, if states above 2 GeV are observed it would be useful and beneficial to then calculate beyond this artificially imposed energy limit.

5.3.4   Summary of Ray's asymmetry parameter, κ in Tables 5.4.16 - 5.4.17.

Tables 5.4.16 - 5.4.17 contain the Ray's asymmetry parameter calculated for the knots and links used in our model.

5.4   Discussion and Conclusions

After calculating the rotational energies of the knots and links identified with glueball candidates, we can discuss how our results impact the model as outlined in Chapter II. In Chapter II, we made an assumption that the knots and links used in the model possessed a spherical symmetry. As we have shown in this chapter, the assumption about spherical symmetry doesn't hold in general for knots and links. The only case where the spherical symmetry persisted was that of the Borromean Rings, link 6_3^2. The remaining knots and links are classified as either prolate/oblate symmetric or asymmetric tops.

In Chapter II, we used the relationship between the energy of a spherical top and all available particle mass data to determine the excited energy spectrum. The energy spectrum was based on Equation (2.6.2), where the energy depends only on the value of J and a fitted parameter δ. The fitted parameter δ is the spherical analog of the rotational constants A, B and C; with spherical symmetry only one rotational constant value is needed. Consequently, the rotational energy prediction calculated for each value of J is identical, i.e. if $\delta = 5$ MeV for all $J = 1$ energy levels the rotational energy is 5 MeV. In this chapter, we have determined the symmetry of each individual knot/link used in the model. The rotational energy was based on value of J and the symmetry of each individual knot. The rotational energies for each knot/link are different, resulting in a much more complicated and richer spectrum.

The most dramatic result of this generalization are predictions for additional excited levels. With the loss of symmetry we find the splitting of previously degenerate

144

energy levels. For example, if we compare the predictions for the knot 5_2 in Chapter II with those calculated in Table 5.4.5 we find two additional $J = 1$ levels and four additional $J = 2$ levels. Another consequence of this richer spectrum is that it is easier to match excited energy levels with their identified knot or link. Using the example of knot 5_2 again, the model identifies a ground state and two excited levelss (a $J = 1$ and a $J = 2$) with this knot. In Chapter II, the rotational energy was based on the spherically symmetric top which predicts one $J = 1$ level and one $J = 2$ level. However, after determining that knot 5_2 is asymmetric, we now predict three $J = 1$ levels and five $J = 2$ levels. This richer spectrum allows for a better fit with the data, in addition to predicting many more excited states. This comparison is summarized in Table 5.4.1.

In conclusion, the results from this chapter provide the model with predictions about the structure of the excited glueball spectrum. We predict a very rich glueball spectrum of ground states, as well as excited levels. The rotational energy spectrum contains many levels close together in energy which may be difficult to distinguish, however many predictions are within experimental reach. Hopefully these predictions can be tested.

Table 5.4.1: Comparison of predicted rotational energy spectrum of knot 5_2 as a spherical top vs. an asymmetric top.

Knot	State	Mass (MeV)	J	E_{rot}^{sphere} (MeV)	E_J^{sphere} (MeV)	J	w	E_{rot}^{asym} (MeV)	E_J^{asym} (MeV)
						2	4.02	30	1535
						2	4	30	1535
						2	1.26	23	1528
						2	0.74	22	1527
	$f_2(1525)$	**1525 $\pm$ 5**	2	15	1520	2	-0.02	20	1525
	$f_1(1510)$	**1518 $\pm$ 5**	1	5	1510	1	1.09	9	1514
						1	0.91	9	1514
						1	0	7	1512
5_2	$f_0(1500)$	**1505 $\pm$ 6**	0	0	1505	0	0	0	1505

Table 5.4.2: Rotational Energies of spherical link: 6_2^3.

Knot/Link	State	J	E_{rot} (MeV)	E_J (MeV)
6_2^3	[1749]	0	0	**1749 $\pm$ 22**
		1	7	1756 $\pm$ 22
		2	20	1769 $\pm$ 22

Table 5.4.3: Rotational Energies of prolate and oblate knots/links: 2_1^2, 3_1, $2_1^2 \# 2_1^2$, 4_1 and 6_2^2.

Knot/Link	κ	State	J	K	E_{rot} (MeV)	E_J (MeV)
2_1^2	-1.0	$f_0(600)$	0	0	0	**800 $\pm$ 400**
			1	0	21	821 $\pm$ 400
			1	1	29	829 $\pm$ 400
			2	0	63	863 $\pm$ 400
			2	1	72	872 $\pm$ 400
			2	2	97	897 $\pm$ 400
3_1	0.999341	$f_0(980)$	0	0	0	**980 $\pm$ 10**
			1	1	16 $\pm$ 1	996 $\pm$ 11
			1	0	20 $\pm$ 0	1000 $\pm$ 10
			2	2	44 $\pm$ 3	1024 $\pm$ 13
			2	1	56 $\pm$ 1	1036 $\pm$ 11
			2	0	60 $\pm$ 1	1040 $\pm$ 11
$2_1^2 \# 2_1^2$	-0.98		0	0	0	1215.1 $\pm$ 1.2
			1	0	20.0	1235.1 $\pm$ 1.2
			1	1	46.6	1261.6 $\pm$ 1.2
		$f_2(1270)$	2	0	60.0	**1275.1 $\pm$ 1.2**
			2	1	86.6	1301.7 $\pm$ 1.2
			2	2	166.3	1381.4 $\pm$ 1.2
4_1	-0.997603		0	0	0	1271.2 $\pm$ 1.2
		$f_1(1285)$	1	0	10.6 $\pm$ 0.6	**1281.8 $\pm$ 0.6**
			1	1	11.5 $\pm$ 0.6	1282.8 $\pm$ 1.2
			2	0	31.8 $\pm$ 0.4	1303.0 $\pm$ 1.0
			2	1	32.7 $\pm$ 0.5	1303.9 $\pm$ 1.1
			2	2	35.6 $\pm$ 2.5	1306.8 $\pm$ 3.08
6_2^2	-0.998734	[1709]	0	0	0	**1709 $\pm$ 22**
			1	0	5 $\pm$ 0	1714 $\pm$ 22
			1	1	8 $\pm$ 0	1717 $\pm$ 22
			2	0	14 $\pm$ 0	1723 $\pm$ 22
			2	1	17 $\pm$ 0	1726 $\pm$ 22
			2	2	26 $\pm$ 2	1735 $\pm$ 23

Table 5.4.4: Rotational Energies of asymmetric prolate knots/links: 4_1^2, 2_1^2 (one component of link 2_1^2 carries double flux), 5_1 and 5_2.

Knot/Link	κ	State	J	w	E_{rot} (MeV)	E_J (MeV)
4_1^2	-0.115689	[1209]	0	0	0	**1209 ± 19**
			1	0	10	1219 ± 19
			1	0.72	12	1221 ± 19
			1	1.28	14	1223 ± 19
			2	-0.23	29	1238 ± 19
			2	0.15	30	1239 ± 19
			2	1.85	36	1245 ± 19
			2	4	43	1252 ± 19
			2	4.23	44	1253 ± 19
2_1^2	-0.600209	$f_0(1200 - 1600)$	0	0	0	**1325 ± 15**
			1	0	41	1366 ± 1
			1	0.89	54	1379 ± 15
			1	1.11	57	1382 ± 15
			2	-0.04	122	1447 ± 15
			2	0.67	133	1458 ± 15
			2	1.33	143	1468 ± 15
			2	4	182	1507 ± 15
			2	4.04	183	1508 ± 15
5_1	-0.362301		0	0	0	1419.5 ± 0.9
		$f_1(1420)$	1	0	6.9	**1426.4 ± 0.9**
			1	0.81	8.9	1428.3 ± 0.9
			1	1.19	10.2	1429.7 ± 0.9
		$f_2(1430)$	2	-0.11	20.5	1440.0 ± 0.9
			2	0.43	22.0	1441.5 ± 0.9
			2	1.57	25.1	1444.6 ± 0.9
			2	4	31.9	1451.4 ± 0.9
			2	4.11	32.2	1451.7 ± 0.9
5_2	-0.678317	$f_0(1500)$	0	0	0	**1505 ± 6**
			1	0	7	1512 ± 6
			1	0.91	9	1514 ± 6
		$f_1(1510)$	1	1.09	9	1514 ± 6
		$f_2(1525)$	2	-0.02	20	1525 ± 6
			2	0.74	22	1527 ± 6
			2	1.26	23	1528 ± 6
			2	4	30	1535 ± 6
			2	4.02	30	1535 ± 6

Table 5.4.5: Rotational Energies of asymmetric prolate and oblate knots/links: 5_1^2, 6_3^3, 6_1^2, and 7_7^2.

Knot/Link	κ	State(s)	J	w	E_{rot} (MeV)	E_J (MeV)
5_1^2	-0.0611502	[1502]	0	0	0	**1502 $\pm$ 21**
			1	0	8	1510 $\pm$ 21
			1	0.69	9	1511 $\pm$ 21
			1	1.31	9	1511 $\pm$ 21
			2	-0.26	24	1526 $\pm$ 21
			2	0.08	24	1526 $\pm$ 21
			2	1.92	26	1528 $\pm$ 21
			2	4	28	1530 $\pm$ 21
			2	4.26	28	1530 $\pm$ 21
6_3^3	-0.735524		0	0	0	1543 $\pm$ 12
			1	0	6	1549 $\pm$ 12
			1	0.93	8	1551 $\pm$ 12
			1	1.07	9	1552 $\pm$ 12
		$f_2(1565)$	2	-0.01	19	**1562 $\pm$ 12**
			2	0.79	21	1564 $\pm$ 12
			2	1.2	22	1565 $\pm$ 12
			2	4	27	1570 $\pm$ 12
			2	4.01	27	1570 $\pm$ 12
6_1^2	0.0248771		0	0	0	1615 $\pm$ 6
			1	1.32	6	1620 $\pm$ 6
			1	0.68	7	1621 $\pm$ 6
			1	0	8	1623 $\pm$ 6
			2	4.29	17	1631 $\pm$ 6
			2	4	17	1632 $\pm$ 6
			2	1.97	21	1635 $\pm$6
			2	0.033	24	1638 $\pm$ 6
		$f_2(1640)$	2	-0.29	25	**1639 $\pm$ 6**
7_7^2	0.129734	[1674]	0	0	0	**1674 $\pm$ 22**
			1	1.28	6	1680 $\pm$ 22
			1	0.72	6	1680 $\pm$ 22
			1	0	7	1681 $\pm$ 22
			2	4.22	17	1691 $\pm$ 22
			2	4	17	1691 $\pm$ 22
			2	1.83	20	1694 $\pm$ 22
			2	0.17	22	1696 $\pm$ 22
			2	-0.22	22	1696 $\pm$ 22

Table 5.4.6: Rotational Energies of asymmetric prolate and oblate knots/links: 6_1, 6_2, 7_8^2, and 6_1^3.

Knot/Link	κ	State(s)	J	w	E_{rot} (MeV)	E_J (MeV)
6_1	-0.566748	[1710]	0	0	0	**1710 ± 22**
			1	0	3	1713 ± 22
			1	0.88	4	1714 ± 22
			1	1.12	4	1714 ± 22
			2	-0.04	9	1719 ± 22
			2	0.64	10	1720 ± 22
			2	1.36	11	1721 ± 22
			2	4	14	1724 ± 22
			2	4.04	14	1724 ±
6_2	-0.582995	$f_0(1710)$	0	0	0	**1724 ± 7**
			1	0	6	1730 ± 7
			1	0.88	7	1731 ± 7
			1	1.12	7	1731 ± 7
			2	-0.04	17	1741 ± 7
			2	0.65	18	1742 ± 7
			2	1.35	19	1743 ± 7
			2	4	22	1746 ± 7
			2	4.04	22	1746 ± 7
7_8^2	0.81974	[1742]	0	0	0	**1742 ± 22**
			1	1.05	6	1748 ± 22
			1	0.95	6	1748 ± 22
			1	0	7	1749 ± 22
			2	4.01	17	1759 ± 22
			2	4	17	1759 ± 22
			2	1.14	19	1761 ± 22
			2	0.86	19	1761 ± 22
			2	-0.01	20	1762 ± 22
6_1^3	-0.891911	[1743]	0	0	0	**1743 ± 22**
			1	0	6	1749 ± 22
			1	0.97	7	1750 ± 22
			1	1.03	7	1750 ± 22
			2	-0.002	17	1760 ± 22
			2	0.92	18	1761 ± 22
			2	1.08	18	1761 ± 22
			2	4	22	1765 ± 22
			2	4.00	22	1765 ± 22

Table 5.4.7: Rotational Energies of asymmetric prolate and oblate knots/links:6_3, 6_3^2, 8_7^3 and 8_{19}.

Knot/Link	κ	State(s)	J	w	E_{rot} (MeV)	E_J (MeV)
6_3	-0.492805		0	0	0	1738 ± 10
			1	0	6	1744 ± 10
			1	0.85	7	1745 ± 10
			1	1.15	7	1745 ± 10
		$f_2(1750)$	2	-0.06	17	$\mathbf{1755 \pm 10}$
			2	0.56	18	1756 ± 10
			2	1.44	19	1757 ± 10
			2	4	22	1760 ± 10
			2	4.06	22	1760 ± 10
6_3^2	-0.824825	[1751]	0	0	0	$\mathbf{1751 \pm 22}$
			1	0	5	1756 ± 22
			1	0.95	7	1758 ± 22
			1	1.05	7	1758 ± 22
			2	-0.01	16	1767 ± 22
			2	0.86	18	1769 ± 22
			2	1.14	18	1769 ± 22
			2	4	23	1774 ± 22
			2	4.01	23	1774 ± 22
8_7^3	0.291762		0	0	0	1796 ± 12
			1	1.22	5	1801 ± 12
			1	0.78	6	1801 ± 12
			1	0	6	1802 ± 12
			2	4.13	15	1811 ± 12
			2	4	15	1811 ± 12
			2	1.65	18	1813 ± 12
			2	0.35	19	1815 ± 12
		$f_2(1810)$	2	-0.13	19	$\mathbf{1815 \pm 12}$
8_{19}	0.0235572	[1839]	0	0	0	$\mathbf{1839 \pm 23}$
			1	1.32	5	1844 ± 23
			1	0.68	6	1845 ± 23
			1	0	6	1845 ± 23
			2	4.29	15	1854 ± 23
			2	4	15	1854 ± 23
			2	1.97	17	1856 ± 23
			2	0.03	19	1858 ± 23
			2	-0.29	19	1858 ± 23

Table 5.4.8: Rotational Energies of asymmetric prolate and oblate knots/links: 7_1, 8_{20}, 7_2 and 7_3.

Knot/Link	κ	State(s)	J	w	E_{rot} (MeV)	E_J (MeV)
7_1	-0.126537	[1850]	0	0	0	**1850 ± 23**
			1	0	4	1854 ± 23
			1	0.72	5	1855 ± 23
			1	1.28	6	1856 ± 23
			2	-0.22	13	1863 ± 23
			2	0.16	13	1863 ± 23
			2	1.84	16	1866 ± 23
			2	4	19	1869 ± 23
			2	4.22	19	1869 ± 23
8_{20}	0.594679		0	0	0	1897 ± 12
			1	0	5	1902 ± 12
			1	0.89	5	1902 ± 12
			1	1.11	6	1903 ± 12
			2	4.04	14	1911 ± 12
			2	4	14	1911 ± 12
			2	1.34	16	1914 ± 12
			2	0.66	17	1914 ± 12
		$f_2(1910)$	2	-0.04	18	**1915 ± 12**
7_2	-0.762128	[1925]	0	0	0	**1925 ± 24**
			1	0	4	1929 ± 24
			1	0.94	6	1931 ± 24
			1	1.06	6	1931 ± 24
			2	-0.01	11	1936 ± 24
			2	0.81	13	1938 ± 24
			2	1.19	14	1939 ± 24
			2	4	20	1945 ± 24
			2	4.01	20	1945 ± 24
7_3	-0.869755	[1926]	0	0	0	**1926 ± 24**
			1	0	4	1930 ± 24
			1	0.97	6	1932 ± 24
			1	1.03	6	1932 ± 24
			2	-0.003	11	1937 ± 24
			2	0.90	13	1939 ± 24
			2	1.10	14	1940 ± 24
			2	4	20	1946 ± 24
			2	4.00	20	1946 ± 24

Table 5.4.9: Rotational Energies of asymmetric prolate knots/links: 7_1^2, 7_4, 8_{15}^2 and 7_2^2.

Knot/Link	κ	State(s)	J	w	E_{rot} (MeV)	E_J (MeV)
7_1^2	-0.790578		0	0	0	1932 ± 12
			1	0	4	1936 ± 12
			1	0.94	6	1937 ± 12
			1	1.06	6	1938 ± 12
		$f_2(1950)$	2	-0.01	12	**1944 ± 12**
			2	0.83	14	1946 ± 12
			2	1.17	14	1946 ± 12
			2	4	20	1951 ± 12
			2	4.01	20	1951 ± 12
7_4	-0.814452	[1936]	0	0	0	**1936 ± 24**
			1	0	4	1940 ± 24
			1	0.95	6	1942 ± 24
			1	1.05	6	1942 ± 24
			2	-0.01	13	1949 ± 24
			2	0.85	14	1950 ± 24
			2	1.15	14	1950 ± 24
			2	4	19	1955 ± 24
			2	4.01	19	1955 ± 24
8_{15}^2	-0.943571	[1937]	0	0	0	**1937 ± 24**
			1	0	4	1941 ± 24
			1	0.99	6	1943 ± 24
			1	1.01	6	1943 ± 24
			2	-0.0006	13	1950 ± 24
			2	0.96	14	1951 ± 24
			2	1.04	14	1951 ± 24
			2	4	19	1956 ± 24
			2	4.00	19	1956 ± 24
7_2^2	-0.735572	[1959]	0	0	0	**1959 ± 24**
			1	0	4	1963 ± 24
			1	0.93	6	1965 ± 24
			1	1.07	6	1965 ± 24
			2	-0.01	13	1972 ± 24
			2	0.79	14	1973 ± 24
			2	1.21	15	1974 ± 24
			2	4	19	1978 ± 24
			2	4.01	19	1978 ± 24

Table 5.4.10: Rotational Energies of asymmetric prolate and oblate knots/links: 8_8^3, 7_4^2, 7_5 and 7_3^2.

Knot/Link	κ	State(s)	J	w	E_{rot} (MeV)	E_J (MeV)
8_8^3	0.169353	[1959]	0	0	0	**1959 ± 24**
			1	1.26	4	1963 ± 24
			1	0.74	5	1964 ± 24
			1	0	6	1965 ± 24
			2	4.20	13	1972 ± 24
			2	4	13	1972 ± 24
			2	1.79	15	1974 ± 24
			2	0.21	17	1976 ± 24
			2	-0.20	17	1976 ± 24
7_4^2	-0.763933	[1960]	0	0	0	**1960 ± 24**
			1	0	4	1964 ± 24
			1	0.94	5	1965 ± 24
			1	1.06	6	1966 ± 24
			2	-0.01	13	1973 ± 24
			2	0.81	14	1974 ± 24
			2	1.19	14	1974 ± 24
			2	4	18	1978 ± 24
			2	4.01	18	1978 ± 24
7_5	-0.909101		0	0	0	1971 ± 11
		$f_1(1970)$	1	0	4	1975 ± 11
			1	0.98	6	1977 ± 11
			1	1.02	6	1977 ± 11
			2	-0.002	12	1983 ± 11
			2	0.93	13	1985 ± 11
			2	1.07	14	1985 ± 11
			2	4.00	20	1991 ± 11
			2	4.00	20	1991 ± 11
		$f_4(2050)$	4	4.02	47	**2018 ± 11**
7_3^2	-0.592062	[1969]	0	0	0	**1969 ± 24**
			1	0	4	1973 ± 24
			1	0.89	5	1974 ± 24
			1	1.11	5	1975 ± 24
			2	-0.04	13	1982 ± 24
			2	0.66	14	1983 ± 24
			2	1.34	14	1983 ± 24
			2	4	17	1986 ± 24
			2	4.04	17	1986 ± 24

Table 5.4.11: Rotational Energies of asymmetric prolate and oblate knots/links: 8_{21}, 7_7, 7_6 and 7_1^3.

Knot/Link	κ	State(s)	J	w	E_{rot} (MeV)	E_J (MeV)
8_{21}	0.346069	[1974]	0	0	0	**1974 ± 24**
			1	1.20	4	1978 ± 24
			1	0.80	5	1979 ± 24
			1	0	6	1980 ± 24
			2	4.11	13	1987 ± 24
			2	4	13	1987 ± 24
			2	1.59	15	1989 ± 24
			2	0.41	17	1991 ± 24
			2	-0.11	17	1991 ± 24
7_7	-0.900145	[1976]	0	0	0	**1976 ± 24**
			1	0	5	1981 ± 24
			1	0.97	6	1982 ± 24
			1	1.03	6	1982 ± 24
			2	-0.002	14	1990 ± 24
			2	0.92	15	1991 ± 24
			2	1.08	15	1991 ± 24
			2	4	18	1994 ± 24
			2	4.00	18	1994 ± 24
7_6	0.183698	[1979]	0	0	0	**1979 ± 24**
			1	1.26	5	1984 ± 24
			1	0.74	5	1984 ± 24
			1	0	6	1985 ± 24
			2	4.19	14	1993 ± 24
			2	4	14	1993 ± 24
			2	1.77	16	1995 ± 24
			2	0.23	17	1996 ± 24
			2	-0.19	17	1996 ± 24
7_1^3	-0.83397	[1982]	0	0	0	**1982 ± 24**
			1	0	4	1986 ± 24
			1	0.96	6	1988 ± 24
			1	1.04	6	1988 ± 24
			2	-0.006	12	1994 ± 24
			2	0.87	14	1996 ± 24
			2	1.13	14	1996 ± 24
			2	4	19	2001 ± 24
			2	4.01	19	2001 ± 24

Table 5.4.12: Rotational Energies of asymmetric prolate and oblate knots/links: 9^2_{49}, 7^2_5, 9^2_{43} and 7^2_6.

Knot/Link	κ	State(s)	J	w	E_{rot} (MeV)	E_J (MeV)
9^2_{49}	-0.354835	$f_0(2020)$	0	0	0	**1992 $\pm$ 16**
			1	0	4	1996 $\pm$ 16
			1	0.81	5	1997 $\pm$ 16
			1	1.19	6	1998 $\pm$ 16
		$f_2(2000)$	2	-0.11	12	2004 $\pm$ 16
			2	0.42	12	2004 $\pm$ 16
			2	1.58	14	2006 $\pm$ 16
			2	4	17	2009 $\pm$ 16
			2	4.11	17	2009 $\pm$ 16
7^2_5	0.187861		0	0	0	2001 $\pm$ 80
			1	1.25	3	2004 $\pm$ 80
			1	0.75	3	2004 $\pm$ 80
			1	0	3	2004 $\pm$ 80
			2	4.11	8	2009 $\pm$ 80
			2	4	8	2009 $\pm$ 80
			2	1.76	9	2010 $\pm$ 80
			2	0.24	10	2011 $\pm$ 80
		$f_2(2010)$	2	-0.11	10	**2011 $\pm$ 80**
9^2_{43}	0.0132954	[1997]	0	0	0	**1997 $\pm$ 24**
			1	1.33	4	2001 $\pm$ 24
			1	0.67	5	2002 $\pm$ 24
			1	0	6	2003 $\pm$ 24
			2	4.30	12	2009 $\pm$ 24
			2	4	13	2010 $\pm$ 24
			2	1.98	15	2112 $\pm$ 24
			2	0.018	17	2014 $\pm$ 24
			2	-0.30	17	2014 $\pm$ 24
7^2_6	-0.566859	[1998]	0	0	0	**1998 $\pm$ 24**
			1	0	5	2003 $\pm$ 24
			1	0.	5	2003 $\pm$ 24
			1	1.12	6	2004 $\pm$ 24
			2	-0.04	14	2012 $\pm$ 24
			2	0.64	14	2012 $\pm$ 24
			2	1.36	15	2013 $\pm$ 24
			2	4	17	2015 $\pm$ 24
			2	4.04	17	2015 $\pm$ 24

Table 5.4.13: Rotational Energies of asymmetric prolate and oblate knots/links: 8_3^4, 8_{16}^2, 9_{46} and 9_{54}^2.

Knot/Link	κ	State(s)	J	w	E_{rot} (MeV)	E_J (MeV)
8_3^4	-0.822918	[2000]	0	0	0	**2000 $\pm$ 24**
			1	0	3	2003 $\pm$ 24
			1	0.95	6	2006 $\pm$ 24
			1	1.05	6	2006 $\pm$ 24
			2	-0.006	10	2010 $\pm$ 24
			2	0.86	12	2012 $\pm$ 24
			2	1.14	13	2013 $\pm$ 24
			2	4	20	2020 $\pm$ 24
			2	4.01	20	2020 $\pm$ 24
8_{16}^2	-0.268727		0	0	0	2023 $\pm$ 8
			1	0	4	2027 $\pm$ 8
			1	0.78	5	2029 $\pm$ 8
			1	1.22	5	2028 $\pm$ 8
			2	-0.14	13	2036 $\pm$ 8
			2	0.33	13	2036 $\pm$ 8
			2	1.67	14	2037 $\pm$ 8
			2	4	16	2039 $\pm$ 8
			2	4.14	16	2039 $\pm$ 8
		$f_3(2050)$	3	-0.42	25	**2048 $\pm$ 8**
9_{46}	-0.619507	$f_0(2060)$	0	0	0	**2055 $\pm$ 25**
			1	0	4	2059 $\pm$ 25
			1	0.89	5	2060 $\pm$ 25
			1	1.11	5	2060 $\pm$ 25
			2	-0.03	11	2066 $\pm$ 25
			2	0.68	12	2067 $\pm$ 25
			2	1.32	13	2068 $\pm$ 25
			2	4	16	2071 $\pm$ 25
			2	4.03	16	2071 $\pm$ 25
9_{54}^2	0.120131		0	0	0	2141 $\pm$ 11
			1	1.28	4	2145 $\pm$ 11
			1	0.72	4	2145 $\pm$ 11
			1	0	5	2146 $\pm$ 11
			2	4.23	11	2152 $\pm$ 11
			2	4	11	2152 $\pm$ 11
			2	1.85	13	2154 $\pm$ 11
			2	0.15	15	2156 $\pm$ 11
		$f_2(2150)$	2	-0.23	15	**2156 $\pm$ 11**

Table 5.4.14: Rotational Energies of asymmetric prolate and oblate knots/links: 8_1, 9_{19}^3, 8_1^4 and 9_1.

Knot/Link	κ	State(s)	J	w	E_{rot} (MeV)	E_J (MeV)
8_1	0.55492		0	0	0	2127 ± 12
			1	1.13	4	2131 ± 12
			1	0.87	4	2131 ± 12
			1	0	5	2132 ± 12
			2	4.05	11	2138 ± 12
			2	4	11	2138 ± 12
			2	1.38	13	2140 ± 12
			2	0.62	14	2141 ± 12
		$f_2(2140)$	2	-0.05	14	$\mathbf{2141 \pm 12}$
9_{19}^3	-0.521485	$f_0(2200)$	0	0	0	$\mathbf{2189 \pm 13}$
			1	0	4	2193 ± 13
			1	0.86	4	2193 ± 13
			1	1.14	5	2194 ± 13
			2	-0.05	11	2200 ± 13
			2	0.59	12	2201 ± 13
			2	1.41	12	2201 ± 13
			2	4	14	2203 ± 13
			2	4.05	14	2203 ± 13
8_1^4	-0.591888		0	0	0	2287 ± 60
			1	0	3	2291 ± 60
			1	0.89	4	2292 ± 60
			1	1.11	4	2292 ± 60
			2	-0.04	10	2297 ± 60
			2	0.66	11	2298 ± 60
			2	1.34	12	2299 ± 60
			2	4	14	2301 ± 60
			2	4.04	14	2301 ± 60
		$f_4(2300)$	4	-0.52	33	$\mathbf{2320 \pm 60}$
9_1	-0.480279		0	0	0	2289 ± 28
			1	0	3	2292 ± 28
			1	0.85	4	2292 ± 28
			1	1.15	4	2293 ± 28
		$f_2(2300)$	2	-0.07	8	$\mathbf{2297 \pm 28}$
			2	0.55	9	2298 ± 28
			2	1.45	10	2299 ± 28
			2	4	13	2301 ± 28
			2	4.07	13	2302 ± 28
		$f_3(2300)$	3	4	21	2310 ± 28

Table 5.4.15: Rotational Energies of asymmetric prolate knots/links: 9_{20}^3, 8_4^3 and 9_4.

Knot/Link	κ	State(s)	J	w	E_{rot} (MeV)	E_J (MeV)
9_{20}^3	-0.361546		0	0	0	2306 ± 60
		$f_1(2310)$	1	0	4	**2310 ± 60**
			1	0.81	4	2310 ± 60
			1	1.19	5	2311 ± 60
			2	-0.11	11	2317 ± 60
			2	0.43	11	2317 ± 60
			2	1.57	12	2318 ± 60
			2	4	14	2320 ± 60
			2	4.11	14	2320 ± 60
8_4^3	-0.104949	$f_0(2330)$	0	0	0	**2332 ± 12**
			1	0	3	2335 ± 12
			1	0.71	4	2336 ± 12
			1	1.29	4	2336 ± 12
		$f_2(2340)$	2	-0.24	9	2341 ± 12
			2	0.14	10	2342 ± 12
			2	1.86	11	2343 ± 12
			2	4	13	2345 ± 12
			2	4.24	13	2345 ± 12
9_4	-0.860882		0	0	0	2406 ± 50
			1	0	3	2409 ± 50
			1	0.96	4	2410 ± 50
			1	1.04	4	2410 ± 50
			2	-0.004	8	2415 ± 50
			2	0.89	9	2415 ± 50
			2	1.11	10	2416 ± 50
			2	4	12	2419 ± 50
			2	4.00	12	2419 ± 50
		$f_6(2510)$	6	-0.26	59	**2465 ± 50**

Table 5.4.16: Ray's Asymmetry parameter, κ, for knots and links

knot/link	κ	knot/link	κ	knot/link	κ
2_1^2	-1	8_5	-0.74254	8_4^3	-0.10495
3_1	0.99934	8_6	-0.69770	8_5^3	-0.17866
4_1	-0.99760	8_7	-0.79458	8_6^3	-0.50713
4_1^2	-0.11570	8_8	-0.87001	8_7^3	0.29176
5_1	-0.36230	8_9	-0.47946	8_8^3	0.16935
5_2	-0.67832	8_{10}	-0.18616	8_9^3	-0.61604
5_1^2	-0.06115	8_{11}	-0.18447	8_{10}^3	-0.83702
6_1	-0.56675	8_{12}	-0.91929	8_1^4	-0.59189
6_2	-0.58290	8_{13}	-0.88039	8_2^4	0.15205
6_3	-0.49281	8_{14}	-0.63535	8_3^4	-0.82292
6_1^2	0.02488	8_{15}	0.19420	9_1	-0.48028
6_2^2	-0.99873	8_{16}	-0.07157	9_2	-0.28559
6_3^2	-0.82483	8_{17}	-0.78187	9_3	-0.57386
6_1^3	-0.89191	8_{18}	0.87697	9_4	-0.86089
6_2^3	-0.93933	8_{19}	0.02356	9_5	-0.09275
6_3^3	-0.73552	8_{20}	0.59468	9_6	-0.49863
7_1	-0.12654	8_{21}	0.34607	9_7	-0.91853
7_2	-0.76213	8_1^2	0.86957	9_8	-0.32943
7_3	-0.86976	8_2^2	-0.93844	9_9	-0.82345
7_4	-0.81445	8_3^2	-0.30483	9_{10}	0.16125
7_5	-0.90910	8_4^2	-0.56401	9_{11}	-0.67311
7_6	0.18370	8_5^2	-0.80332	9_{12}	-0.95588
7_7	-0.90014	8_6^2	-0.50713	9_{13}	-0.41682
7_1^2	-0.79058	8_7^2	-0.70889	9_{14}	-0.77489
7_2^2	-0.73557	8_8^2	-0.21279	9_{15}	-0.70289
7_3^2	-0.59206	8_9^2	-0.08055	9_{16}	-0.93549
7_4^2	-0.76393	8_{10}^2	-0.90815	9_{17}	-0.01058
7_5^2	0.18786	8_{11}^2	-0.89167	9_{18}	0.25760
7_6^2	-0.56685	8_{12}^2	-0.97396	9_{19}	-0.55263
7_7^2	0.12973	8_{13}^2	-0.74926	9_{20}	-0.57267
7_8^2	0.81974	8_{14}^2	0.91365	9_{21}	-0.87253
7_1^3	-0.83397	8_{15}^2	-0.94357	9_{22}	-0.68598
8_1	0.55492	8_{16}^2	-0.26873	9_{23}	-0.70768
8_2	-0.22096	8_1^3	-0.56167	9_{24}	-0.90788
8_3	-0.95159	8_2^3	-0.82812	9_{25}	-0.55097
8_4	-0.44435	8_3^3	-0.61555	9_{26}	-0.92977

Table 5.4.17: Ray's Asymmetry parameter, κ, for knots and links (continued)

knot/link	κ	knot/link	κ	knot/link	κ
9_{27}	0.67353	9^2_{14}	-0.13991	9^2_{50}	-0.04067
9_{28}	-0.86412	9^2_{15}	-0.41981	9^2_{51}	0.04437
9_{29}	-0.42098	9^2_{16}	-0.28730	9^2_{52}	-0.33148
9_{30}	0.74076	9^2_{17}	-0.09530	9^2_{53}	-0.66014
9_{31}	-0.32014	9^2_{18}	-0.53738	9^2_{54}	0.12013
9_{32}	-0.88272	9^2_{19}	-0.38657	9^2_{55}	0.52853
9_{33}	0.54535	9^2_{20}	-0.85746	9^2_{56}	-0.59524
9_{34}	-0.03530	9^2_{21}	-0.76536	9^2_{57}	-0.85628
9_{35}	0.80730	9^2_{22}	-0.85416	9^2_{58}	0.59533
9_{36}	-0.47180	9^2_{23}	-0.54695	9^2_{59}	-0.40847
9_{37}	0.18740	9^2_{24}	0.14303	9^2_{60}	-0.77067
9_{38}	-0.34157	9^2_{25}	-0.02367	9^2_{61}	-0.40945
9_{39}	-0.14130	9^2_{26}	-0.47284	9^3_1	-0.32886
9_{40}	-0.98910	9^2_{27}	-0.86520	9^3_2	-0.88428
9_{41}	-0.79778	9^2_{28}	-0.97037	9^3_3	-0.87086
9_{42}	-0.78263	9^2_{29}	-0.61928	9^3_4	0.06788
9_{43}	-0.43643	9^2_{30}	0.61483	9^3_5	-0.63883
9_{44}	0.07417	9^2_{31}	-0.68762	9^3_6	-0.19745
9_{45}	-0.84192	9^2_{32}	-0.82369	9^3_7	-0.78247
9_{46}	-0.61951	9^2_{33}	-0.62500	9^3_8	-0.94881
9_{47}	-0.75642	9^2_{34}	-0.53180	9^3_9	-0.37496
9_{48}	0.19643	9^2_{35}	-0.60789	9^3_{10}	-0.53638
9_{49}	-0.68391	9^2_{36}	-0.17180	9^3_{11}	0.71309
9^2_1	-0.42476	9^2_{37}	-0.13063	9^3_{12}	0.13210
9^2_2	-0.79040	9^2_{38}	-0.60899	9^3_{13}	-0.66384
9^2_3	-0.06142	9^2_{39}	-0.68668	9^3_{14}	-0.62307
9^2_4	-0.87387	9^2_{40}	-0.55968	9^3_{15}	0.89491
9^2_5	-0.67751	9^2_{41}	0.15076	9^3_{16}	-0.03241
9^2_6	-0.55077	9^2_{42}	0.16344	9^3_{17}	-0.76086
9^2_7	-0.76855	9^2_{43}	0.01330	9^3_{18}	0.13750
9^2_8	-0.90686	9^2_{44}	-0.56475	9^3_{19}	-0.52149
9^2_9	-0.63351	9^2_{45}	-0.75428	9^3_{20}	-0.36155
9^2_{10}	-0.04110	9^2_{46}	-0.89634	9^3_{21}	0.21866
9^2_{11}	-0.07023	9^2_{47}	-0.40419	9^4_1	-0.85286
9^2_{12}	-0.10581	9^2_{48}	-0.17761		
9^2_{13}	-0.27755	9^2_{49}	-0.35484		

CHAPTER VI

CONCLUSIONS

6.1   Summary

In Chapter II, we established a hypothesis where glueball candidates are modeled
as tightly knotted or linked chromoelectric flux tubes. A specific knot or link is iden-
tified with a glueball ground state, and the excited states are modeled as rotational
excitations. We first updated the model with the newest data available from the
Particle Data Group, which included a few new f states as well as some particle mass
changes. With the additional states and mass changes, the model still produces a
very good fit. The reduced χ^2 for the fit from Chapter II which includes all available
particles is $\chi^2 = 1.0$, compared to $\chi^2 = 0.84$ in the original model.

In order to estimate the rotational energy in the model, we assumed the knots and
links had an approximate spherical symmetry. We used the relationship between the
energy of a spherical top and all available particle mass data to determine the excited
energy spectrum. The energy spectrum was based on Equation (2.6.2), where the
energy depends only on the value of J and a fitted parameter δ. The fitted parameter
δ is the spherical analog of the rotational constants A, B and C; with spherical
symmetry only one rotational constant value is needed. Consequently, the rotational
energy prediction calculated for each value of J is identical, i.e. if $\delta = 5$ MeV for
all $J = 1$ energy levels the rotational energy is 5 MeV. Based on the assumption of

spherical symmetry for all of the knots/links in the model, we generated a predicted spectrum of glueball states.

However, when we calculated the moment of inertia tensor of knots/links identified with glueball candidates to determine their symmetry, we found that only one of the candidates (link 6_2^3, the Borromean Rings) is in fact a spherical rigid rotor. From this result, we decided to expand the model to include the specific symmetry (symmetric oblate, symmetric prolate, or asymmetric) of each knot or link used and calculate a new rotational energy spectrum.

In chapter III we performed exact calculations of the moment of inertia for a few specific link geometries, specifically: the Hopf link, the Hopf link where one loop carries double flux, link $2_1^2 \# 2_1^2$, a link with 4-elements, a link with 5-elements, a link with 6-elements, a link with 4-tori (3 tori going through the center of the 4th torus) and a link with 5-tori (4 tori going through the center of the 5th torus). The chapter detailed those calculations for several hollow and solid link configurations, and then generalized the solution for a chain with n elements. The inertia tensor results are expressed in terms of the radius of the flux tube, a. Therefore, in order to calculate a numerical value for the principal moments of inertia, we needed to determine the radius of the flux tube. In Chapter IV, we used the Bag Model as a guide to calculate the radius. We also introduced the rigid rotor classification scheme as well as the rotational energy relationships based on symmetry properties.

In Chapter V, we drew on the results from Chapters III and IV which allowed us to calculate rotational energies for the knots and links used in the glueball model detailed

in Chapter II. For each knot or link, we calculated the moment of inertia tensor either from its geometry or from a set of vertex coordinate points. From the eigenvalues of the inertia tensor, we were able to determine specifically the symmetry of each knot or link. We used κ, known as Ray's asymmetry parameter, to classify the knots and links as a prolate symmetric top, an oblate symmetric top or an asymmetric top. Once classified, we calculated and tabulated all rotational energies. This generalization introduced a number of energy level splittings which created an excitation energy spectrum much denser and more complex than that presented in Chapter II.

6.2 Model Predictions

The model makes a number of predictions that could be confirmed by experiment. We predict more ground states than are currently observed, each of which would be associated with a knot or link. Some of the particular predictions from the model are summarized in Table 6.2.1.

Table 6.2.1: Some ground state f_0 particle predictions from the Model.

Knot	Mass (MeV)	Width (MeV)
4_1^2	1208	≥ 100
$2_1^2 \# 2_1^2$	1215	185
4_1	1271	24
5_1	1420	55
5_1^2	1502	≥ 100
6_3^3	1543	134
6_1^2	1615	99

In addition to new ground states, the results of Chapter V predict additional excited levels. When the assumption of spherical symmetry is relaxed, we find the splitting of previously degenerate energy levels. For example, if we compare the predictions for the knot 5_2 in Chapter II with those calculated in Table 5.4.5 we find two additional $J = 1$ levels and four additional $J = 2$ levels. Another consequence of this richer spectrum is that it is easier to match excited energy levels with their identified knot or link. Using the example of knot 5_2 again, the model identifies a ground state and two excited levels (a $J = 1$ and a $J = 2$) with this knot. In Chapter II, the rotational energy was based on the spherically symmetric top which predicts one $J = 1$ level and one $J = 2$ level. However, after determining that knot 5_2 is asymmetric, we now predict three $J = 1$ levels and five $J = 2$ levels. This richer spectrum allows for a better fit with the data, in addition to predicting many more excited states. This comparison is summarized in Table 5.4.1.

We predict a very rich glueball spectrum of ground states, as well as excited levels. The rotational energy spectrum contains many levels close together in energy which may be difficult to distinguish, however many predictions are within experimental reach. Hopefully these predictions can be tested.

6.3   Further Research

We have consulted with Dr. Jason Cantarella of the University of Georgia about computing a set of vertex coordinate points for the link $2_1^2\#2_1^2$. Since we have an exact moment of inertia tensor calculation for this link, we could do a comparison with the

set of vertex coordinate points to estimate their error. With this error estimate, we could better evaluate the error associated with rotational energy calculations based on a set of vertex coordinate points.

Additionally, one could explore the possibility of chiral partners for the states listed in the table. We looked at the η states, which are similar to f states ($J^{PC} = 0^{++}$) but have negative parity conjugation, i.e. $J^{PC} = 0^{-+}$. The chirality of the knot or link associated with a given f state was examined to determine if there should be an η state associated with the f state. As presented in the introduction, if a knot changes to a left handed or right handed knot under a mirror reflection, it is considered chiral. If the knot remains unchanged under mirror reflection it is considered to be achiral. The symmetry transformation associated with chirality is parity. An achiral knot only allows a positive parity transformation, whereas a chiral knot yields both a positive and a negative parity transformation. Therefore, in principle for every chiral knot associated with an f state there should be another state with negative parity: the η states. Therefore, the model could be expanded to include chiral partners.

REFERENCES

[1] Fritzch, M., M. Gell-Mann, and H. Leutwyler, 1971. Phys. Lett. **47B**, 365.

[2] Gross, D.J. and Wilczek, F., 1973, Phys. Rev. D **8**, 3633

[3] Weinberg, S., 1973, Phys. Rev. Lett. **31**, 494

[4] Godfrey, S. and Napolitano, J., 1999, Rev. Mod. Phys. **71**, 1411

[5] Gell-Mann, M. Phys. Lett. 1964, **8**, 214.

[6] Zweig, G., 1964, CERN preprint 8419/TH.412; 8182/TH.401 (unpublished)

[7] Klempt, Eberhard. "Glueballs, Hybrids, Pentaquarks: Introduction to Hadron Spectroscopy and Review of Selected Topics." 18th Annual Hampton University Graduate Studies, Jefferson Lab, Newport News, Virginia, June 2-20, 2003. arXiv:hep-ph/0404270 v1 29 Apr 2004; Klempt, Eberhard. "Glueballs, Hybrids, Pentaquarks: Introduction to Hadron Spectroscopy and Review of Selected Topics." 18th Annual Hampton University Graduate Studies, Jefferson Lab, Newport News, Virginia, June 2-20, 2003.

[8] Aitchison, I. J. R. and Hey, A. J. G. "Gauge Theories in Particle Physics - Volume I: From Relativistic Quantum Mechanics to QED," 2003, Taylor & Francis Group LLC.

[9] Griffiths, David. "Introduction to Elementary Particles," 1987, John Wiley & Sons, Inc. Used primarily chapters 1, 2, 5, 9, and 11.

[10] Kenyon, I. R. "Gauge Theories," 1986, Eur. J. Phys. **7** 115 - 123

[11] Politzer, H. D. 1974 Phys. Rep. **14C** 129

[12] Kane, Gordon. "Modern Elementary Particle Physics," 1993, Perseus Publishing.

[13] Watson, Andrew. "The Quantum Quark," 2004, Cambridge University Press.

[14] Frauenfelder, Hans and Henley, Ernest M. "Subatomic Physics," 1991, Prentice Hall.

[15] Yukawa, H., 1935, Proc. Phys. Math. Soc. Jap. **17**, 48

[16] Wikipedia: www.wikipedia.com. Primarily the Particle Physics, Standard Model, and QCD articles.

[17] Davydov, A. S. "Quantum Mechanics," 1966, NEO Press.

[18] C. Amsler *et al.*, 2008, Physics Letters G **667**, 1.

[19] C. J. Morningstar and M. Peardon, 1999, Phys. Rev. D **60**.

[20] Pennington, M.R. "Glueballs: the Naked Truth," Invited talk at Workshop on Photon Interactions and the Photon Structure, Lund, Sweden, Sep 1998.

[21] Close, F. E. "Gluonic Hadrons," 1988, Rep. Prog. Phys. **51**, 833.

[22] Amsler, C. and Close, F.E., 1995, Phys. Lett. B **353**, 385; 1996, Phys. Rev. D **53**, 295.

[23] Lee, W. and Weingarten, D., 2000, Phys. Rev. D **61** 014015.

[24] Li, D., Yu, H. and Shen, Q., "Glueball-quarkonia content of the f0(1370), f0(1500) and f0(1710)," hep-ph/0001107.

[25] Close, F.E. and Kirk, A., 2000, Phys. Lett. B **483**, 345.

[26] L.S. Celenza *et al.*, 2000, Phys. Rev. C **61**, 035201.

[27] M. Strohmeier-Presicek *et al.*, 1999, Phys. Rev. D **60**, 054010.

[28] Buniy, R.V. and Kephart, T.W., 2003, Phys. Lett. **B576**, 127 and 2005, Int. J. Mod. Phys. A **20**, 1252.

[29] Cromwell, Peter. "Knots and Links," 2004, Cambridge Press.

[30] http://www.freelearning.com/knots/

[31] http://www.pims.math.ca/knotplot/knot-theory/knot-theory.html

[32] Thomson, W. H. 1869, Transactions of the Royal Society of Edinburgh **25** 217-220

[33] Ashton, T., Cantarella, J. Piatek, M., and Rawdon, E. "Self-Contact Sets for 50 Tightly Knotted and Linked Tubes." math.DG/0508248

[34] Moffatt, H.K. "The Energy Spectrum of Knots and Links," 1990, Nature **347** 367 - 369

[35] Wikipedia "Moment of Inertia," http://en.wikipedia.org/wiki/Moment_of_inertia

[36] Weisstein, Eric W. "Moment of Inertia," From MathWorld–A Wolfram Web Resource. http://mathworld.wolfram.com/Torus.html

[37] Weisstein, Eric W. "Torus," From MathWorld–A Wolfram Web Resource. http://mathworld.wolfram.com/Torus.html

[38] Symon, Keith R. "Mechanics," 1953, Addison-Wesley Publishing Company, Inc.

[39] Muller, Berndt. "Lecture Notes in Physics: The Physics of the Quark-Gluon Plasma," 1985, Springer-Verlag

[40] Guidry, Mike. "Gauge Field Theories: An Introduction with Applications," 1991, John Wiley & Sons, Inc.

[41] Rho, M. "Pions and the Chiral Bag," 1982, Prog. Part. Nucl. Phys. **8** 103

[42] Lee, T.D. "Particle Physics and Introduction to Field Theory," 1981, Harwood

[43] Baym, G. "Confinment and deconfinement of quarks in nuclear matter," 1982, Prog. Part. Nucl. Phys. **8** 73 - 101

[44] Curtis G. Callan, Jr., Roger F. Dashen and David J. Gross. "A theory of hadronic structure," 1979, Physical Review **D8** 1826 - 1855

[45] Lecture Notes: "Rotation of Polyatomic Molecules," 2009 (http://www.gps.caltech.edu/ gab/ch21b/lectures/lecture05.pdf)

[46] Ingram, David J.E. "Radio and Microwave Spectroscopy," 1976, Butterworth & Co. Ltd. pg. 44

[47] Levine, Ira N. "Molecular Spectroscopy," 1975, John Wiley & Sons, Inc. ch. 5 (Rotation of Polyatomic Molecules) pgs. 197 - 216

[48] Ingram, David J.E. "Spectroscopy at Radio and Microwave Frequencies," 1967, Butterworth & Co. Ltd. pgs. 119 - 120

[49] Nielson, H.H. "Infrared Bands of Slightly Asymmetric Molecules," 1931, Phys. Rev. **38** 1432

[50] Hainer, R.M., Cross, P.E. and King, G.W. "The Asymmetric Rotor I. Calculation and Symmetry Classification of Energy Levels," 1943, J. Chem. Phys. **11** 27

[51] Wang, S.C. "On the Asymmetrical Top in Quantum Mechanics," 1929, Phys. Rev. **34** 243

[52] Gordy, Walter. "Microwave Molecular Spectra," 1984, Knovel. ch. 7 (Asymmetric-Top Molecules) pgs. 227 - 235.

[53] Townes, Charles H. and Schawlow, Arthur L. "Microwave Spectroscopy," 1955, McGraw-Hill Book Company, Inc. ch. 4 (Asymmetric-Top Molecules) pgs. 84-89.

[54] Atkins, P.W. "Molecular Quantum Mechanics," 1983, Oxford University Press. ch. 11 (Molecular rotational and vibrational transitions) pgs. 288 - 291.

[55] Rawdon, Eric. Email correspondence with Dr. Eric Rawdon of the University of St. Thomas.